# ABSTRACT

Title of Thesis: PARAMETRIC INVESTIGATIONS INTO FLUID-STRUCTURE INTERACTIONS IN HOVERING FLAPPING FLIGHT

Jesse Maxwell, 2013

Thesis Directed By: Professor Balakumar Balachandran
Department of Mechanical Engineering

A parametric investigation into flapping flight is presented. For a Reynolds number of 75, harmonically forced flapping dynamics is studied. A wing section is modeled as two rigid links connected by a hinge with a torsion spring-damper combination. This section is wrapped in a smooth aerodynamic surface for immersion in the fluid domain. An immersed boundary method is employed on a two-dimensional structured Cartesian grid to solve the incompressible form of the Navier-Stokes equations for low Reynolds numbers by using a finite difference method. Fully coupled fluid-structure interactions are considered. Performance metrics, which include cycle-averaged lift, drag, power, and their ratios, are used to characterize the effects of different parameters and kinematics. Principal components of flow-field structures are quantified, and the system's response is correlated to performance. The thesis findings can serve as a basis to understand and identify flapping frequencies that provide high performance.

# PARAMETRIC INVESTIGATIONS INTO FLUID-STRUCTURE INTERACTIONS IN HOVERING FLAPPING FLIGHT

by

Jesse Maxwell

Thesis submitted to the Faculty of the Graduate School of the
University of Maryland, College Park in partial fulfillment
of the requirements for the degree of
Master of Science
2013

Advisory Committee:
Professor Balakumar Balachandran, Chair and Advisor, Mechanical Engineering
Associate Professor James Baeder, Department of Aerospace Engineering
Assistant Professor Amir Riaz, Department of Mechanical Engineering

For Zoë

Acknowledgements

I would like to thank my advisor and committee chair, Professor Balachandran, for his guidance, encouragement and significant support while pursuing my graduate studies, introducing me to and guiding this research, and assistance in writing this thesis. I would also like to thank my committee members, Professor Baeder and Professor Riaz, for their instruction relevant to my research and assistance in completing this thesis.

I would like to thank Tim Fitzgerald for his assistance with my research and contributions to my understanding in the field of computational modeling and the physics of flapping flight, for his deep knowledge of everything I approached him with, and his general enthusiasm for this work. I would also like to thank Dr. Chris Chabalko and all of my colleagues in Professor Balachandran's Computational Dynamics Laboratory from whom I have received guidance, assistance and support.

I would like to thank my parents for their emphasis on education and creativity, push to constantly challenge myself, encouragement in my academic and professional pursuits, and their facilitation of developing a strong work ethic from an early age. And most of all, I would like to thank my beautiful and intelligent wife for all of her support and encouragement.

## I. Nomenclature, Acronyms, and Abbreviations

| | |
|---|---|
| A | Normalized leading link length as percentage of chord length $L_C$ |
| $A_x$ | Amplitude of horizontal translation for harmonic kinematics |
| $A_\theta$ | Amplitude of rotation for harmonic kinematics |
| $C_D$ | Coefficient of drag |
| $C_L$ | Coefficient of lift |
| $C_M$ | Coefficient of moment |
| $C_P$ | Coefficient of power |
| $C_T$ | Coefficient of total thrust |
| $C_{Tx}$ | Coefficient of horizontal thrust |
| DNS | Direct Numerical Simulation |
| $\vec{F}_L / L$ | Lift force per unit span of the wing |
| FSI | Fluid-Structure Interaction |
| $I_A$, $I_B$ | Mass moments of inertia of leading link (A) and free link (B), respectively |
| $k$ | Torsion spring constant |
| $L_C$ | Chord length of un-deformed structure |
| LES | Large Eddy Simulation |
| $l_A$ | Length of leading link (A) as proportion of $L$ |
| $m_A$, $m_B$ | Mass of leading link (A) and mass of free link (B), respectively |
| PCA | Principal Component Analysis |
| $P_{rot}$ | Power associated with rotational inertia and fluid moments |
| $P_{tr}$ | Power associated with translational inertia and fluid forces |

| | |
|---|---|
| $p$ | Pressure field of fluid |
| $\vec{p}_{fluid}$ | Linear momentum of the fluid |
| $Q_\alpha$ | Generalized force from fluid acting on structure |
| $R_x$ | Translational forces required to drive the kinematics |
| $R_\theta$ | Moment required to drive the kinematics |
| $Re$ | Reynolds number ≡ $(\max(\lvert\mathbf{v}(t)\rvert)\,\rho_{fluid}\,L_C / \mu)$ |
| $\rho_{fluid}$ | Density of the fluid |
| SVD | Singular Value Decomposition |
| $T$ | Period of flapping, in seconds s |
| $t$ | Time, in seconds s |
| $\mathbf{v}$ | Velocity vector field with components ($u$, $v$) |
| $u$ | Horizontal component of fluid velocity |
| UVLM | Unsteady Vortex Lattice Method |
| $v$ | Vertical component of fluid velocity |
| $\mathbf{x}$ | Position vector ($x$, $y$) |
| $x$ | Horizontal position coordinate |
| $y$ | Vertical position coordinate |
| W | Inverse of forcing frequency to natural frequency ratio: W = $\omega_n / \omega_f$ |
| W#A## | Case identifier for inverse frequency ratio # and leading link percentage of normalized length ##. *Example: W2A10 corresponds to* $\omega_f / \omega_n = 1/2$ *and leading link length of* $0.10L_C$ |
| $\alpha$ | Angle between leading and free links of the structure, in radians rad |
| $\gamma$ | Phase shift in angle of attack kinematics, in radians rad |

| | |
|---|---|
| $\mu$ | Dynamic viscosity of the fluid |
| $\nu$ | Kinematic viscosity of the fluid |
| $\theta$ | Angular orientation of leading link (A) of structure, in radians rad |

## Table of Contents

## List of Figures

## 1. Introduction

Over the past decade in particular, flapping flight has become an increasingly popular field of investigation with multi-disciplinary approaches taken by diverse groups of researchers, including groups in aerospace and mechanical engineering, robotics, fluid physics, scientific computation, mathematics, and experimental and computational biology. While the aerodynamics and performance of high Reynolds (Re) number flows over fixed airfoils is relatively well understood and has been extensively treated for over a century, significantly more complicated phenomena associated with unsteady mobile wings in flapping flight and transient periodic flow, have only recently been given consideration. These studies of the physics of flapping flight, commonly at lower Re numbers, include experimental investigations (e.g., Ellington et al., 1996; Dickinson *et al*., 1999) and computational modeling and simulation (e.g., Liu and Kawachi, 1998; Sun and Tang, 2002; Ramamurti and Sandberg, 2002; Ramamurti and Sandberg, 2006; Vanella *et al*., 2009; Wang, 2000a; Wang, 2000b; Wang *et al*., 2004). The classical omission of the detailed study of flapping flight is largely due to the complexity of the physics in the context of continuum fluids and flexible solids, complex geometries, interactions between fluid and mechanical structures, and time dependence. Studies of three-dimensional fluid dynamics and structural interactions associated with unsteady flapping flight face significantly complex and difficult challenges, which cannot be addressed by analytical methods. Furthermore, the size and time scales to be resolved have been beyond the capabilities of scientific computing systems until recently. Developments during the past few decades have led to the availability of accurate high-speed cameras and sensors, and developments in computational power, numerical

methods, and computer architectures for detailed reproduction, measurement, and simulation have allowed for experimental investigations and numerical simulation with sufficient resolution and accuracy. These developments have helped gain a better understanding of the physics of flapping flight.

Conventional fixed-wing aircraft separate propulsion, lift, and the use of directional control in distinct controllable systems are well understood under many diverse conditions to date (e.g., Anderson, 2007; Clancy, 1975; Katz, 1991; White, 1974). Flapping wings as a mechanism for flight can combine the capabilities of propulsion, lift, and maneuvering in one composite system at the expense of design and control complexity (Sane and Dickinson, 2001). While evolution has enabled and inspired the development of myriad designs, kinematics, and expert control of flapping systems across many scales of biology, current methods can do little to decipher commonly observed flapping flight phenomena. Early conceptual models to understand the multiple simultaneous functions of flapping wings were proposed by Weis-Fogh, who described a general process of delayed stall, wake capture, rotational lift, and the added mass effect (Weis-Fogh, 1965). An increasing interest in computational treatment of flapping flight of birds and insects has developed as computing power has advanced, with two-dimensional simulations of directly solved viscous flow performed by the end of the 20$^{th}$ century (e.g. Liu, Ellington, Kawachi, Van Den Berg and Wilmott, 1998; Wang, 2000a). Researchers have proposed that mechanical properties of wings, geometry, and kinematics play a significant role in system performance and provide insights into flapping flight of insects, motivating investigations such as those by Wang, Birch and Dickinson (2004). These authors have addressed varied kinematics and geometry and

confirmed previously proposed flapping flight related phenomena in the context of particular case studies by comparing two-dimensional simulation results with results from three-dimensional experiments. Three-dimensional numerical investigations have been limited to specific case studies due to the immense computational cost, and these investigations have ranged from fully-coupled fluid-structure interactions (FSI) and direct numerical simulation (DNS) to the utilization of simplified methods for weak FSI, large eddy simulation (LES), and turbulence modeling. Three-dimensional simulations have been used to model hovering in the hawkmoth (Liu, Ellington, Kawachi, Van Den Berg and Wilmott, 1998), *drosophila* (Sun and Tang, 2002) and general low-Reynolds number insect hovering flight (Ramamurti and Sandenberg, 2002). Other groups have opted to make simplifying assumptions for conditions rather than fluid modeling such as large aspect ratio wings with small span-wise angular displacements so as to allow for accurate modeling in two dimensions (e.g., Vanella, Fitzgerald, Preidikman, Balaras, and Balachandran, 2009; Wang, Birch and Dickinson, 2004), DNS with weakly coupled FSI. Other simplifications to the modeling of fluid flow include inviscid potential-based methods, such as the unsteady vortex lattice method (UVLM) and similar (e.g. Sane and Dickinson, 2002; Fitzgerald, Valdez, Vanella, Balaras, and Balachandran, 2011). Inviscid methods have been shown to exhibit similar qualitative trends and provide reasonably accurate cycle-averaged steady-state performance metrics for high Reynolds number flapping. Steady forward flight has been treated by Gopalakrishnan and Tafti (2010) in a manner similar to steady hovering flight, but with the significant assumption of fully prescribed, constant boundary inflow. The prescribed boundary inflow may only be physical for one particular inertial body with a corresponding drag coefficient and under

the assumption that the inertial base of the wings negligibly deviates from a smooth, consistent trajectory during each flapping period. The transition between hovering and forward flight has been briefly addressed experimentally by Vandenberghe, Zhang, and Childress for unstable kinematic symmetry (Vandenberghe, Zhang and Childress, 2004; Vandenberghe, Childress and Zhang 2006).

A two-dimensional formulation has been adopted for the present work as it allows for the use of common modern computational hardware with acceptable processing duration while maintaining the capability of solving strong coupling of fluid-structure interactions and complete resolution of turbulence and small flow structures through direct numerical simulation of a viscous fluid. The present work endeavors to investigate and to characterize the effects of flexibility, structural dissipation at resonance, geometric symmetry and variations in harmonic kinematics of flapping wings. The effects of related parameter variations for steady hovering flight under specified conditions are quantified in terms of dimensionless performance metrics for lift and thrust, drag and power, and their ratios. A mechanism for the transition between hovering and forward flight is proposed as steady, symmetric hovering with decay to asymmetric kinematics to produce an unbalanced lateral force by introducing an offset in the angle of attack.

### Interest in Flapping Flight

Flapping flight is known to be the single most successful mode of animal locomotion that is exhibited by over one thousand species of bats, more than nine thousand species of living, flighted birds, and as many as tens of millions of species of

flying insects. Flapping flight's use for primary locomotion has evolved independently at least during four known periods in the animal kingdom: in mammals, birds, insects, and reptiles. In mammals, flapping wings have developed as branched skeletal frames with a stretched membrane to produce the mostly smooth aerodynamic lift surface with the primary mode of flight as continuous flapping (Simmons, Seymour, Habersetzer, and Gunnel, 2008). In reptiles, pterosaurs are the most notable of the pterosauria order and they had wings composed of a basic skeletal frame at the leading and trailing edges corresponding to "arms" and "legs" with a smooth, stretched membrane between them, lacking additional major frame structures (Gatesy and Dial, 1996). Low-frequency flapping and gliding are believed to be the primary uses of these wings because of the overall Reynolds scale and wing size relative to the body. Birds are known to vary from the 2.6-inch wingspan of the Bee Hummingbird to twelve feet of the Wandering Albatross, and the wings are flapped at frequencies ranging from 80 Hz to less than 1Hz (Wood, 1983). Insects appear on a much smaller scale in general than previous categories and are known to have wing spans that range from the millimeter-wing span of the Fairy Wasp (*Gonatocerus ater*) to the Witch Moth's 12-inch wing span with flapping frequencies ranging from 3 Hz to over 1,000 Hz (Walker, 1999). A snapshot of a small hovering bee is presented in Figure 1.1 with an aesthetic translucent vorticity contour overlay from two dimensional simulations in the present work at Reynolds 75.

The similarities and differences in structure, scale, and mechanisms of lift and maneuvering between these diverse branches of the evolutionary tree illustrate the versatile use of flapping flight From soft, flexible, aerodynamic wings of many birds and bats to more rigid, branch-structured and jagged wings of many insects; from the precise

**Figure 1.1: Hovering Bee with Vorticity Field Overlay**
"Hovering Bee" *from Karen Cusick, used with permission*
(source: http://daffodilphotoblog.wordpress.com/2011/03/05/mostly-bees/);
*Vorticity overlay from present work*.

control of high-frequency hummingbirds and bees to the low-energy expenditure of large soaring birds; from nearly-unitary aspect ratios of wings of small flies to the high aspect ratio of the albatross and dragon flies; the applications, mechanisms, structure and utility of flapping flight are evidently diverse and nearly incomprehensible. However, through a fundamental analysis grounded in first principles of Newtonian physics and continuum mechanics with basic physical models, one can hope to construct elements of understanding of this complex and diverse phenomenon.

Flapping is a highly scalable lift and propulsive concept for locomotion in any fluid media. It combines the highly versatile capabilities of vertical take-off and landing, high-speed maneuverability, and the smoothness and efficiency of gliding. Flapping integrates the actions of lateral propulsion, vertical lift, and directional control into functions performed by a single system: wings. In the context of robotics, flapping flight also includes potential performance-related gains in peak lift and thrust production as well as efficiency gains relative to power consumption when compared to conventional fixed-wing and vertical rotor aircraft. These properties are of significant importance to aircraft and flying robots on all scales; particularly, those intended for isolated operation, extended duration, adverse weather conditions and disturbance rejection, or those desired to have widely variable payload mass capability. Concepts for configurations of small flapping Micro Air Vehicles (MAVs) include humming-bird-sized systems, such as that shown in Figure 1.2, capable of carrying surveillance equipment or other payloads while allowing for precise motion control.

Inspired by the widespread use of this locomotion in nature, for this thesis work, it is chosen to be investigated in the context of a parametric study of hovering and transition to forward flight for the effects of flexibility, structural dissipation and varied kinematics. Consideration is given to the importance of fully-coupled fluid-structure interactions with the dynamic wing model. Combinations of these wing structure and flapping parameters and variations thereof are simulated numerically and compared using resulting performance metrics of each parameter combination case. Performance metrics considered include instantaneous and cycle-averaged dimensionless coefficients of thrust, drag, power, and their ratios. Discrete sampling of parameter combinations allows for

**Figure 1.2: *Archilichus alexandri* (Hummingbird) Hovering**
(source: http://en.wikipedia.org/wiki/File:Archilochus-alexandri-002-edit.jpg, *public domain*).

mapping of performance metrics in parameter space to identify regions of predicted optimality through interpolation of discrete data sets developed through simulation. System frequency responses are analyzed as important clues for fundamental physical phenomena, which can be correlated to system performance.

The rest of this thesis is organized as follows. In Chapter 2, the problem statement is provided, and in the following chapter, the methods used in this study are presented and discussed. In Chapter 4, the results obtained are presented and discussed, and in Chapter 5, a summary of the work carried out is presented along with concluding remarks and suggestions for future work. Additional results are included in Appendix A, and algorithms and codes used in this work are given in Appendix B. Bibliography related to this work is presented at the end.

## 2. Problem Statement

In this thesis work, the author intends to characterize the flapping flight of a small insect during steady hovering for variations in wing flexibility, structural dissipation, chord-wise asymmetry, phase shifts in harmonic kinematics, and the breaking of kinematic symmetry to produce an unbalanced lateral thrust. A common fruit fly hovers at a Reynolds number of approximately 25 whereas a small bee hovers at a Reynolds number of approximately 200 and higher (Sane, 2003). Moderately in between this range is the Reynolds number 75, which has been selected and held fixed for the investigations. Fluid-structure interactions at this Re number have also been studied in the group's previous studies (e.g., Fitzgerald *et al*., 2011). The two-dimensional formulation has been adopted for the present work, as it allows for the use of common modern computational hardware with acceptable processing duration while maintaining the capability of solving strongly coupled fluid-structure interactions. The two-dimensional formulation also allows for complete resolution of turbulence and small flow structures through full direct numerical simulation (DNS) of a viscous fluid. The physics models employed in the present study include an incompressible Newtonian fluid with a flexible dynamic wing modeled as two rigid sections connected by a torsion spring and damper combination; this structural model is wrapped in a smooth aerodynamic body for immersion in the fluid domain, as detailed in the following sections of this chapter.

Many phenomena in nature and in engineering design occur at or near their first linear system resonance, which has not been previously investigated in the context of potential benefits in flapping flight performance. Numerical studies addressing structural flexibility have omitted structural dissipation considerations, only allowing effects of

fluid forces to dampen the structural system. Previous work has also considered only symmetric wing sections and has considered parameter effects in very limited cases due to the high computational effort required. Motivating questions of interest in understanding flapping flight to be addressed by this thesis may be summarized as follows: i) would flapping at the first linear system resonance be beneficial? ii) How does structural dissipation affect the system response? iii) How does wing section geometry affect aerodynamic performance? iv) How do the flapping forcing parameters affect the system response and overall performance? Parametric studies will be performed using the models detailed in the following sections and methods detailed in Chapter 3 to address these motivating questions, with results and analysis presented in Chapter 4.

## 2.1. Fluid Model

The fluid medium that the flexible wing model moves through and interacts with in the present study is modeled as an incompressible Newtonian fluid continuum governed by the Navier-Stokes equations:

$$\frac{\partial \mathbf{v}}{\partial t} + \mathbf{v} \bullet \nabla \mathbf{v} = -\nabla p + \frac{1}{Re} \nabla^2 \mathbf{v} + \mathbf{f} \tag{2.1}$$

Here **v** is the velocity field, t is the time variable, p is the pressure field, and **f** represents all external body forces. The Reynolds number is defined as

$$Re = \frac{\rho_f L_c v_c}{\mu} \tag{2.2}$$

where $\rho_f$ is the fluid density, $L_c$ is the characteristic length of the undeformed wing chord, $v_c$ is the characteristic speed defined by the peak translational speed of the driving point for given kinematics, and $\mu$ is the dynamic viscosity of the fluid. The primary application

intended for this study is the flapping of a flexible wing in atmosphere under sufficiently subsonic conditions as to approximate the flow as being entirely incompressible. Furthermore, pressure shocks travel throughout the fluid domain with effectively infinite speed, such that pressure variations in one fluid element affect all other fluid elements and the entire pressure field instantaneously. Key conditions that must be satisfied are that the velocity field is divergence free for all time; that is,

$$\nabla \bullet \mathbf{v} = 0 \tag{2.3}$$

The equations (2.1) and (2.3) are discretized and solved by using the second-order Adams-Bashforth linear multistep method on a structured, staggered Cartesian mesh. Incompressibility is enforced by using a fractional step method with time integration.

## 2.2. Wing Section Model and Kinematics

The two-dimensional flexible flapping wing is modeled by using two separate components, one in the structural or inertial domain and one in the fluid domain. In the inertial domain, the wing is described by two rigid links connected at a hinge point with a simple torsion spring and damper combination. The torsion spring equilibrium position corresponds to the co-aligned position of both links; that is, it corresponds to $\alpha(t) = 0$ in Figure 2.1. The masses of the links are modeled as point masses at each link's designated center of mass; for example, for link *A*, at a distance $\eta_A$ from the hinge point and having moment of inertia $I_A$. In the fluid domain, the wing is modeled as an aerodynamic surface with specified thickness as a percent of the chord, 3% $L_C$ for the present work,

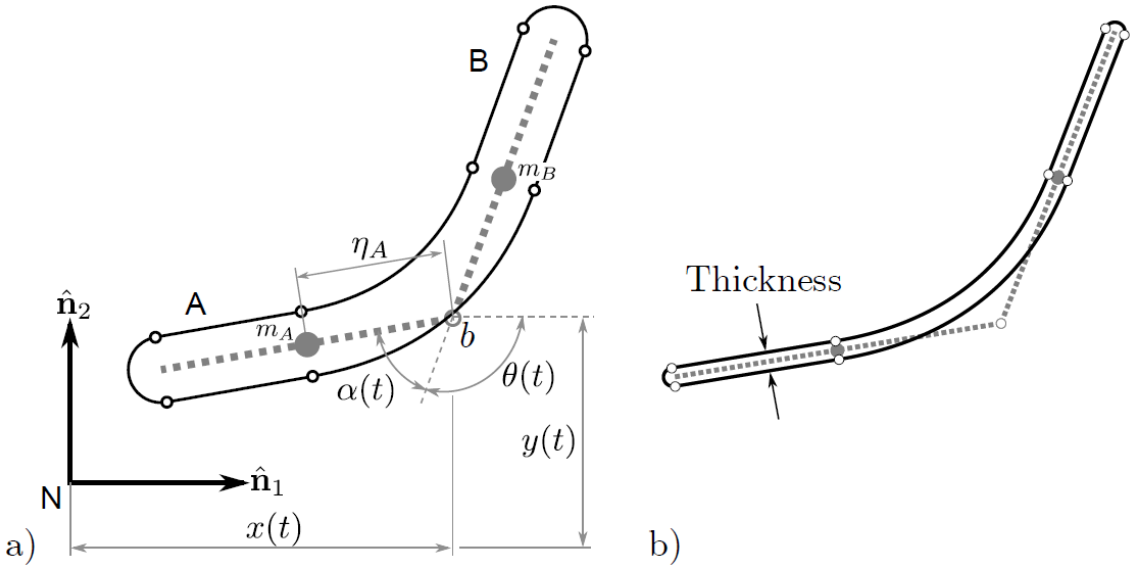


**Figure 2.1: Flexible Wing Cross-Sectional Model for a) 10% $L_C$ Thickness and b) 3% $L_C$ Thickness**
(source: Fitzgerald *et al*., 2011, *used with permission*).

with hemispherical ends and interpolated splines along the flexible section that are tangent to the rigid sections; their curvatures are used to enforce a constant cross-sectional area during flexible deformation.

The two-link structural model is depicted in Figure 2.1. The rigid links A and B (dashed black line) are connected at hinge b by a torsion spring with stiffness k. The variables $x(t)$, $y(t)$, $\theta(t)$, and $\alpha(t)$ are the generalized coordinates used to describe the wing's motion. In the hovering simulations, $x(t)$, $y(t)$, and $\theta(t)$ are prescribed by equations (2.4). $\alpha(t)$ is the only degree of freedom needed to define the system.

$$\begin{aligned} x(t) &= \left(1-e^{-t/\tau}\right)\frac{A_x}{2}\cos\left(\omega_f t\right) \\ y(t) &= 0 \\ \theta(t) &= \theta_0 + \left(1-e^{-t/\tau}\right)A_\theta \sin\left(\omega_f t+\gamma\right) \end{aligned} \tag{2.4}$$

The forcing frequency is defined as $\omega_f = 2/A_x$. The initial offset for the prescribed link is $\theta_0 = -\pi/2$ and the angle of attack amplitude $A_\theta$ for the prescribed link has been set to $\pi/4$ radians. The phase shift in the harmonic theta kinematics, given by $\gamma$, is set to zero in all but one series of case studies. The amplitude in the *x*-direction $A_x$ is set to 2.8 so that the peak translational speed is normalized to 1. The time constant $\tau$ is introduced to provide a non-impulsive start from a vertical rest initial condition and is chosen such that the kinematics reach 99.8% of the prescribed amplitude after $5T$, where $T = 2\pi/\omega_f$ is the period for harmonic flapping; $\tau = 0.8\cdot(2\pi/\omega_f)$.

The smooth decay from rest to steady harmonic motion has been shown to reduce transient effects and startup noise in the flow fields and structural response. The flapping frequency $\omega_f$ is fixed while varying the frequency ratio $\omega_f/\omega_n$ is equivalent to varying the spring stiffness *k* for fixed inertial parameters and allows for variation in the present study between a frequency ratio of 1/6, corresponding to a very stiff spring, to the linear system resonance ratio of 1. With kinematics prescribed for the top link, B, the bottom link, A, is free to deform due to fluid forces with a single degree of freedom, $\alpha(t)$. It can be shown that the equation of motion that governs the structural response is given by:

$$I_A\ddot{\alpha}(t) + c\dot{\alpha}(t) + k\alpha(t) = -I_A\ddot{\theta}(t) + m_A\eta_A\ddot{x}(t)\sin\left(\theta(t)+\alpha(t)\right) + Q_\alpha \qquad (2.5)$$

wherein the dimensionless ratio of the forcing frequency to the natural frequency for the system defined by dimensional system parameters is given by:

$$\frac{\omega_f}{\omega_n} = \frac{2/A_x}{\sqrt{k/I_A}} \qquad (2.6)$$

Here, the structural system's natural frequency is defined as $\omega_n = \sqrt{k / I_A}$. The damping factor is allowed to vary from zero to 5.0 in the present work and it is defined as

$$\zeta = \frac{c}{2\sqrt{kI_A}} \tag{2.7}$$

As shown in Figure 2.1, the structural system is wrapped in an aerodynamic flexible surface in order to smoothly deform in the fluid domain. Fluid forces are interpolated in the fluid domain at the control points defined as the aerodynamic body's surface and the net forces and moments are applied to the structural model presented here. An example of the driving kinematics as well as inertial and fluid-induced

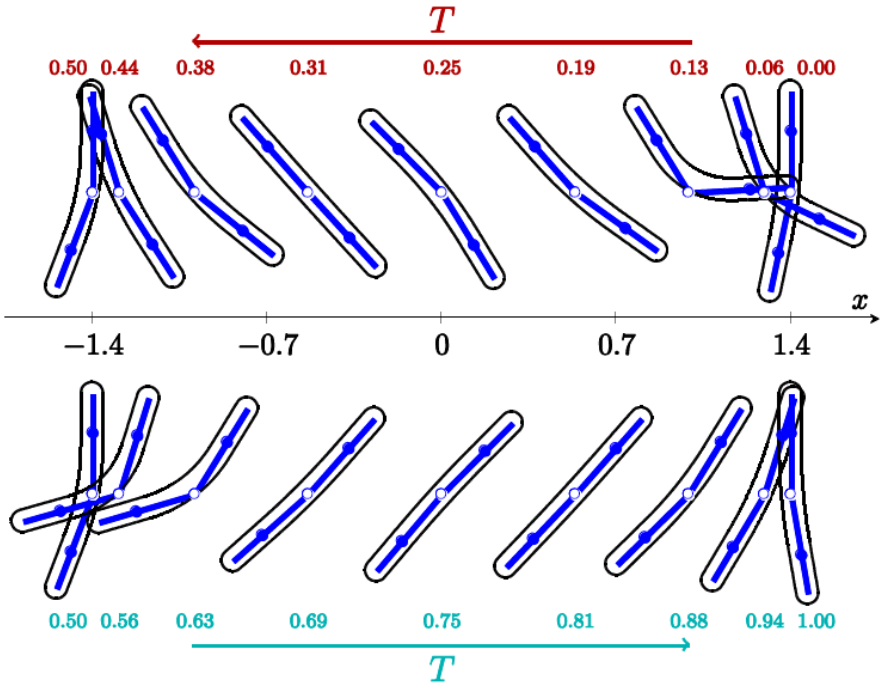


**Figure 2.2: Motion profile with fluid-structure interaction for symmetric harmonic kinematics. The path is given for intervals of 16 equally spaced intervals of the period for a frequency ratio $\omega_f / \omega = 1/3$, Re = 1000, and aerodynamic profile thickness of 10% $L_C$** (source: Fitzgerald et al., 2011, *used with permission*).

deformation is displayed in Figure 2.2 as snapshots over one flapping period. One can see the rigid link structural model embedded in the aerodynamic body during steady state flapping from previous work at Reynolds number 1000 and a thicker wing profile relative to the chord length.

### 2.2.1. Structural Dissipation

The viscous fluid surrounding the immersed wing geometry acts to dissipate energy and it can be considered as a source of damping. The fluid inertial and viscous effects result in a low amplitude of oscillation of the free section than an identical flapping wing without the effects of a surrounding fluid. However, the mechanism of wake capture breaks down this analogy at the two stroke reversals per period where energy imparted into the fluid is partially recaptured for additional lift production. Structural dissipation is introduced in the form of a simple torsion damper at the hinge point. The torsion damper provides a moment that is proportional to the angular velocity $\dot{\alpha}$ at all times and strictly acts to dissipate energy of the system. The frequency ratio defined in the present work is in terms of the *undamped* natural frequency for all cases. It is remarked that the damped natural frequency for an underdamped system is given by $\omega_d = \omega_n \sqrt{1-\zeta^2}$, which will be less than the undamped natural frequency. Also, note that the strong coupling of the fluid-structure interactions results in a non-zero (and non-constant) effective damping for all cases considered due to the viscous fluid; therefore, even nominally undamped cases will not respond in a manner identical to that of an ideal undamped flexible system considered with elementary single degree-of-freedom dynamics.

### 2.2.2. Asymmetrical Links

In a significant portion of the present work, the author addresses the effects of geometrical asymmetry in the simple wing model presented and characterizes the related effects on performance. It is of interest to vary the location of the hinge between wing links, thereby changing their lengths relative to the chord. This is accomplished by generalizing the dynamic description of the system in Section 2.2 and rearranging the control points for the rigid and spline-fitted flexible sections, which describe the aerodynamic body in the fluid domain. An example of the "initial" symmetrical aerodynamic body and the "shifted" body control points are presented for a shift to a leading link length of $0.25L_C$ in Figures 2.3 and 2.4.

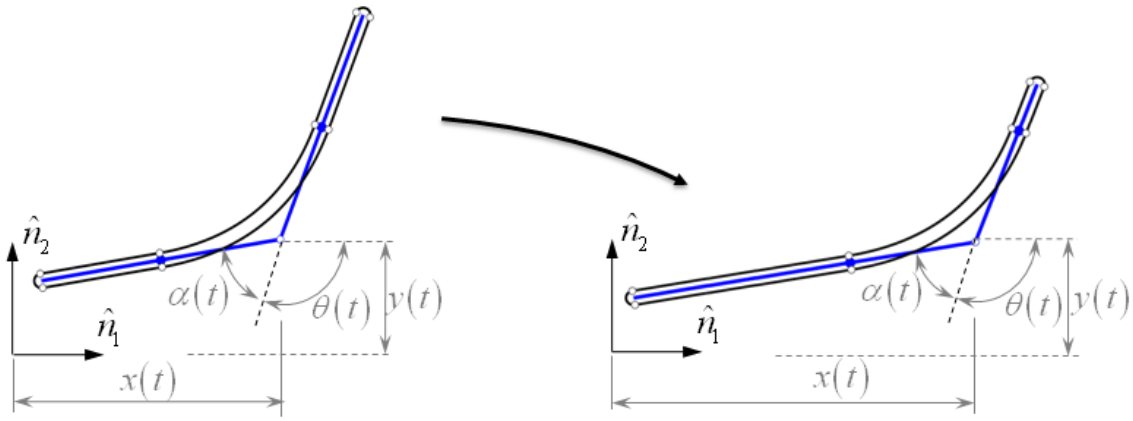


**Figure 2.3: Default symmetric and shifted asymmetric ($0.25L_C$) wing aerodynamic profile.**

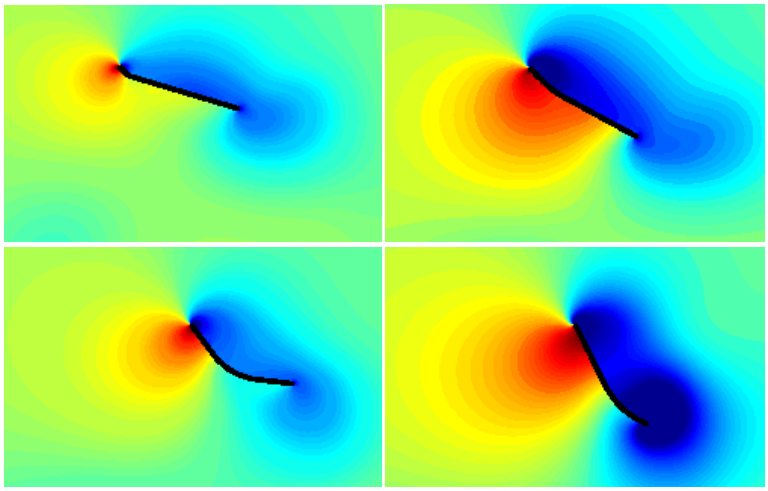

**Figure 2.5: Asymmetric wing profiles with maximum dynamic deflections and pressure contours (-1, 1) to illustrate flexible, free, and prescribed section lengths. A = 0.10$L_c$ (top left), 0.25$L_c$ (top right), 0.50$L_c$ (bottom left), and 0.75$L_c$ (bottom right).**

A series of pressure contour snapshots to illustrate deformation and relative section lengths for the cases considered in the present work are presented in Figure 2.5 for a frequency ratio of $\omega_f / \omega_n = 1/4$. The relative leading section lengths to be considered are 0.10$L_C$, 0.25$L_C$, 0.50$L_C$, and 0.75$L_C$.

Note that the flexible section length varies for the minimum link length. The default symmetrical wing has a flexible section of length 0.45$L_C$, which is slightly reduced to 0.40$L_C$ for the medium-short and medium-long cases. The minimum driven section length case, 0.10$L_C$, due to geometrical constraints has a flexible section length of only 0.10$L_C$. This sharper curvature is visible in the deformation snapshots illustrated in Figure 2.5. The minimum driven section length case may be interpreted as prescribing the slope and position of the leading edge with time and allowing a long free section to deform flexibly. The maximum driven section length may be interpreted as prescribing

the slope and position of a large wing with a small flexible trailing edge. The cases considered allow a coarsely resolved comparison across the full range of a prescribed leading edge with a large flexible section and the existing data for a fully rigid flapping plate.

### 2.2.3. Phase Shift in Theta

Simple harmonic kinematics is a natural starting point for well-understood, periodic, time-varying systems such as periodic, steady flapping. However, previous researchers (e.g., Dickinson, Lehmann, and Sane, 1999; Bos, Lentink, Van Oudheusden, and Bijl, 2008) have proposed alternate kinematics that have been found to produce performance enhancements in some cases relative to lift production or lift-to-power efficiency. Here, simple harmonic kinematics is maintained for the ease of analysis and actuator implementation for Micro Air Vehicle (MAV) design guidance. Despite the relative simplicity of harmonic kinematics, many parameters exist for parametric analysis to discover more efficient or more desirable configurations. Parameters to vary for the considered harmonic kinematics include the vertical and horizontal stroke amplitudes, the angle of attack amplitude, and phase shifts in these spatial variables. The amplitudes are chosen to be fixed in the present work and a phase shift in the angle of attack kinematics is of interest. A pictorial representation of the kinematics for various phase shifts in the angle of attack of a rigid wing is presented in Figure 2.6.

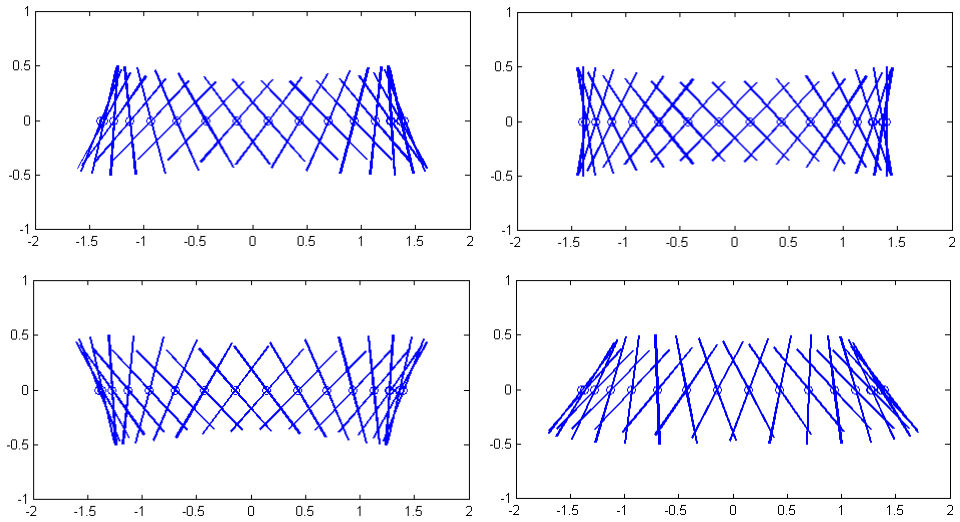

**Figure 2.6: Harmonic kinematics for a rigid wing with a phase shift in theta shown with 20 snapshots over one period at equally spaced time intervals. Phase Shift: -0.5rad (top left), 0 (top right), +0.5rad (bottom left), and +1.0rad (bottom right).**

A thought experiment employing harmonic flapping of a rigid two-dimensional wing as presented in Figure 2.6 intuitively suggests a potentially significant difference in lift production and power expenditure for significant phase shifts. One can imagine that the stroke reversal of a rigid wing with a phase lag in the angle of attack might increase the power expenditure, due to the resistance of the trailing fluid during stroke reversal. Conversely, advancing the phase in the angle of attack may ease the power required for reversal and cause the trailing fluid to increase the lift generated upon angle of attack reversal. This mechanism, known as "wake capture," acts to partially reclaim energy previously expended into the fluid by the wing. Therefore, it is predicted that a reduction in lift and an increase in power will occur for phase lag in angle of attack harmonic kinematics whereas an increase in lift and a reduction in power expenditure will occur for a small phase lead.

# 3. Methods

In this chapter, the models used to carry out the simulations are described, the assumptions made are stated, and the tools used to examine the results are also discussed.

## 3.1. Scope of Methods

In this section, the assumptions and limitations of the physical models used for the fluid and dynamic wing section and the solution method employed are summarized, along with the assumptions made in the problem formulations.

The fluid is assumed to be Newtonian, incompressible, and behave as a homogeneous, isotropic continuum with constant viscosity and density. Gravity loading is not accounted for, and therefore, no weight or buoyancy effects are considered. This is a reasonable assumption due to the small wing area (thickness 3% of chord) and the wing material density ratio to fluid (82.073:1). The density ratio is set in order to fix the mass of the links relative to 10% $L_C$ thickness cases used in previous studies, in which the density ratio was set to 25:1. This ratio was chosen in order to allow the ratio of fluid forces to inertial forces to be on the order of ½. There are no heat transfer effects and no temperature effects considered in the system. The unsteady, incompressible Navier-Stokes equations are also based on a divergence-free velocity field at all times and an infinite speed of pressure propagation is assumed. The Reynolds number of insect flight ranges from 10 to $10^5$ (Sane, 2003). For the fixed Reynolds number studies considered in this thesis, this number is chosen to be 75. For context, the Reynolds number of a common fruit fly is about 25 and about 250 for a honey bee. All turbulence is directly resolved, and no simplification or turbulence modeling is employed. The Kolmogorov

dissipative micro-scale requirement to sufficiently resolve turbulence at all scales dictates a resolution per characteristic length, $L_C$, of (Ferziger and Peric, 1997)

$$N^3 \le Re^{9/4} = 16553.4 \rightarrow N \ge 25.5 \tag{3.1}$$

divisions per chord length, which requires $\Delta x \le 0.039$. The mesh spacing used in the refined region is over an order of magnitude smaller at $\Delta x = 0.003725$ and stretched out to the domain boundaries. The refined region maximum Courant-Freidrichs-Lewey (CFL) number is on the order of

$$\frac{u\Delta t}{\Delta x} \cong \frac{\left(1\frac{m}{s}\right)\left(7\times10^{-5}s\right)}{\left(0.003725m\right)} = 0.02 \tag{3.2}$$

which is well below the stability limit of 1 for an explicit method (Ferziger and Peric, 1997). The "approximately equal to" symbol is used because the translational velocity is normalized to 1m/s while peak velocity magnitudes in the flow field may slightly exceed this characteristic value. Post-analysis of the flow fields reveals peak velocity magnitude of less than 1.6 m/s across all cases whereas the kinematics normalizes the peak translational speed of the driving point for a symmetric wing at 1m/s. This results in a peak CFL number of 0.032 for the worst case simulated. The mesh dissipation number is given by

$$\frac{\nu\Delta t}{\left(\Delta x\right)^2} \cong \frac{\frac{v_c L_c}{\mathrm{Re}}\Delta t}{\left(\Delta x\right)^2} = \frac{\left(\frac{1}{75}\frac{m^2}{s}\right)\left(7\times10^{-5}s\right)}{\left(0.003725m\right)^2} = 0.07 \tag{3.3}$$

Again, "approximately equal to" is used because the characteristic velocity is used for the nominal value. Post-analysis of the flow fields reveal a peak dissipation number of 0.12 for the worst case simulated.

The wing section model receives and transmits forces on its aerodynamic boundary immersed in the fluid at points interpolated along the boundary between mesh points in the fluid domain. The fluid forces are interpolated at these control points and applied to the dynamic model of the wing as a comprehensive force and moment on the lower link with the upper link kinematics fully prescribed. The torsion spring and damper response is computed explicitly with $126\times10^3$ time steps per period and the resulting displacement produces inertial forces due to the free section and prescribed displacement of the leading section to be imposed onto the fluid by the interpolated control points onto the fluid mesh. The final step per iteration is the Poisson inversion for pressure field correction to enforce the divergence-free velocity field condition for incompressible flow, performed once per time step. A single simulation of 15 periods for this model requires approximately 6 weeks to solve on a 2.5GHz processor for raw flow field variable snapshots, force and moment data production.

### 3.2. DNS, Immersed Boundary, and Strongly-Coupled FSI

A fluid domain of 551 horizontal by 1229 vertical grid points is resolved to $0.003725L_C$ in the refined region and stretched to a bounding box of dimensions $30L_C \times 30L_C$ to minimize the effect of boundaries and maximize the allowable simulation duration. Periodic vertical boundary conditions are imposed and a no-slip horizontal wall is imposed at the lateral boundaries. Simulation results are checked following the final period to ensure that flow effects do not reach the boundary. This was found empirically to typically occur between approximately the periods of 17 and 18 depending on the strength of the vertical fluid jet for simulations at the Reynolds number of 75. The reader

is referred to Vanella and Balaras (2009) for a detailed formulation of the immersed boundary method and validation. Prior work has also validated stability and mesh independence under similar simulations of flapping flight (e.g., Fitzgerald *et al*., 2011; Vanella *et al*., 2009; Vanella and Balaras, 2009). The fluid domain discretization used for all case studies in the present work at Reynolds number 75 is a stretched Cartesian mesh of dimension $30L_C \times 30L_C$ as presented in Figure 3.1.

The parameters for density and profile thickness have been chosen such that the ratio of forces on the structure due to the fluid compared to body inertia are approximately a factor of two; that is, $F_{fluid} \sim \frac{1}{2} F_{structural\ inertia}$ in order to emphasize the effects of strongly coupled fluid-structure interactions. Additionally, the boundary conditions on the domain are periodic in the vertical direction and no-slip and no-penetration walls in the lateral direction.

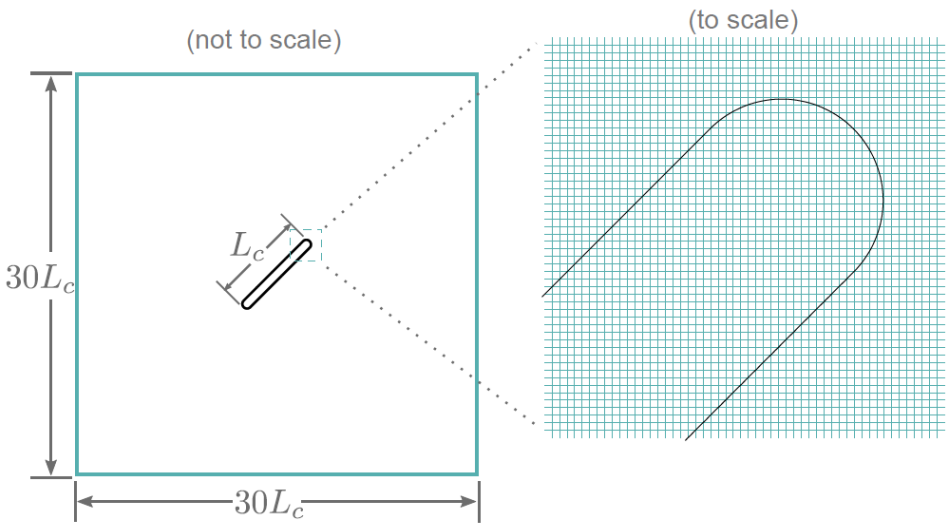


**Figure 3.1: Fluid Domain with Characteristic Wing (Left), and Fluid Grid with Aerodynamic Body (Right).**
(source: Chabalko, Fitzgerald, Valdez, and Balachandran, 2012, *used with permission*)

### 3.2.1. Performance Metrics

The forces interpolated at each time step on the control points of the immersed boundary are decomposed into their vertical and horizontal components. The sum of all vertical components is made dimensionless by using the fluid density, characteristic chord length, and characteristic velocity into the *lift coefficient*, $C_L$, and recorded at each time step; that is,

$$C_L(t) = \frac{Q_y(t)}{\frac{1}{2}\rho_f V_c^2 L_c} \tag{3.3}$$

The sum of all horizontal components is made dimensionless by the fluid density, characteristic chord length, and characteristic velocity into the *drag coefficient*, $C_D$, and recorded at each time step. The sign of the drag coefficient is defined as opposite of the instantaneous translational velocity at each time step, so that

$$C_D(t) = -sgn\left(\dot{x}(t)\right)\left[\frac{Q_x(t)}{\frac{1}{2}\rho_f V_c^2 L_c}\right] \tag{3.4}$$

The moment induced by inertial and fluid forces during flapping should average zero during a flapping cycle for symmetric kinematics. The net moment is made dimensionless by the fluid density, characteristic chord length, and characteristic velocity and denoted as the *moment coefficient*, $C_M$, and is recorded at each time step. It is given symbolically by:

$$C_M(t) = \frac{Q_\alpha(t) + Q_\theta(t)}{\frac{1}{2}\rho_f V_c^2 L_c^2} \tag{3.5}$$

A conservative estimate for the input power for the given system and kinematics has been proposed by Vanella *et al*. (2009). The driving force in the *x*-direction, $R_x(t)$,

and the driving moment in the theta direction, $R_x(t)$, are computed from the mass matrix from the equations of motion with associated fluid forces and moments as

$$\begin{aligned} R_x(t) = {} & (m_A + m_B)\ddot{x} - \left(-m_A\eta_a \sin(\theta+\alpha) + m_B\eta_b \sin(\theta)\right)\ddot{\theta} \\ & -m_A\eta_a \sin(\theta+\alpha)\ddot{\alpha} - (m_A\eta_a \cos(\theta+\alpha)\left(\dot{\theta}+\dot{\alpha}\right)^2 \\ & -m_B\eta_b\dot{\theta}^2 \cos(\theta)) - Q_x \end{aligned} \tag{3.6}$$

$$R_\theta(t) = \left(-m_A\eta_a \sin(\theta+\alpha) + m_B\eta_b \sin(\theta)\right)\ddot{x} + \left(I_A + I_B\right)\ddot{\theta} + I_A\ddot{\alpha} - Q_\theta \tag{3.7}$$

Then the input power for translation, $P_{tr}(t)$, and rotation, $P_{rot}(t)$, can be defined as

$$P_{tr}(t) = \begin{cases} R_x\dot{x}, & \text{if } R_x\dot{x} > 0 \\ 0, & \text{otherwise} \end{cases} \tag{3.8}$$

$$P_{rot}(t) = \begin{cases} R_\theta\dot{\theta}, & \text{if } R_\theta\dot{\theta} > 0 \\ 0, & \text{otherwise} \end{cases} \tag{3.9}$$

It is assumed that the power cannot be negative for this model system. There is no power recovery or storage in the drive or actuation system, and only, power expenditure. The total power is made dimensionless by the characteristic fluid density, velocity and chord length into the *power coefficient* defined by:

$$C_{PW}(t) = \frac{P_{tr}(t) + P_{rot}(t)}{\frac{1}{2}\rho_f V_c^3 L_c} \tag{3.10}$$

While maximum lift production is desired for the design and understanding of systems capable of flight, one must consider the instantaneous and cycle-averaged power required to sustain flight. For the application of Micro Air Vehicle (MAV) design, optimizing lift relative to power consumption allows for an efficient use of on-board power supplies. Conditions and parameters determined for peak lift production are

unlikely to correspond to power consumption minima, and therefore, one looks for the peak efficiency points in the context of the dimensionless lift-to-power ratio defined by

$$\frac{C_L(t)}{C_{PW}(t)} = \frac{\frac{Q_y(t)}{\frac{1}{2}\rho_f V_c^2 L_c}}{\frac{P_{tr}(t)+P_{rot}(t)}{\frac{1}{2}\rho_f V_c^3 L_c}} = \frac{Q_y(t)V_c}{P_{tr}(t)+P_{rot}(t)} \tag{3.11}$$

Maximizing the lift coefficient in MAV design and control allows for the most rapid takeoff and ascent as well as the ability to carry heavy payloads. Alternatively, maximizing the lift-to-power ratio allows for the longest flight duration for a fixed energy supply under otherwise the same conditions. By understanding lift production and power consumption for particular wing configurations and flapping conditions, one can gain insights into flight methods and anatomy in biological systems. Swift mobility and low power consumption may be significant evolutionary drivers, which have led to nature selected efficient and high-performing configurations that modern researchers employing numerical investigations would hope to identify and replicate.

### 3.2.2. Flow Field and Principal Component Analysis

Flow field snapshots at particular points within a steady flapping period are interesting to illustrate major vortex structures and regions of high and low pressure. One looks for moderate free-link displacements, high pressure regions under the wing, low pressure regions above the wing, and flow movement downward in the central fluid jet as indicators of positive lift production. A representative snapshot of the near-body velocity field is presented in Figure 3.2 with illustrative magnitude contours and velocity vectors.

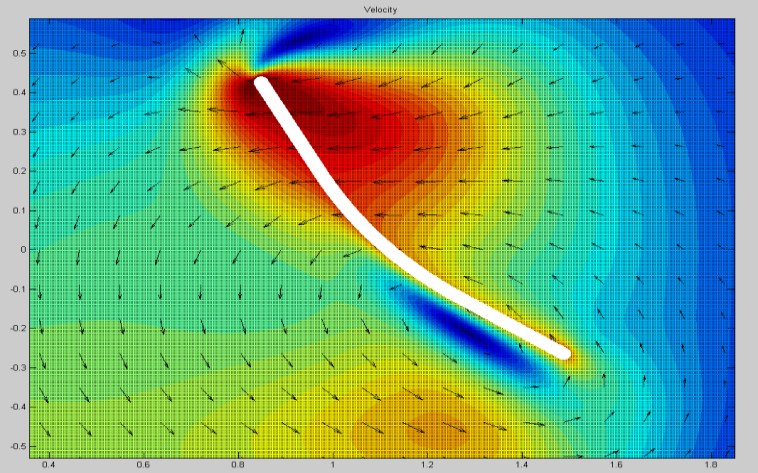


**Figure 3.2: Representative flow field snapshot with wing profile (white), velocity contours, and vector field.**

While useful, these snapshots are individually insufficient to characterize the steady state performance and illustrate key features of the flow field that may not be apparent with one particular snapshot. Principal Component Analysis (PCA) allows the breakdown of the flow field into its most significant features, either per snapshot or considering a cycle average of snapshot data. PCA can be performed by using several means depending upon the level of detail needed, the data to be analyzed and the intended application. For the present work, Singular Value Decomposition (SVD) is used to deter mine the principal components associated with the flow fields. The finite matrix $M$ of discrete data is decomposed into a unitary pre-multiplication matrix $U_t$ , a post-multiplication matrix $V_t$, and a diagonal matrix of $t$ singular values $\Sigma_t$ in order of their significance:

$$M \cong U_t \Sigma_t V_t \tag{3.12}$$

The “approximately equal to” symbol is used to indicate that partial reconstructions with $t$ modes can be a sufficient approximation to an $m \times n$ matrix $M$. An example of SVD of a discrete data set is the decomposition of an image, where each pixel in the image

domain corresponds to a matrix element with a particular scalar value. In Figure 3.3, there is a demonstration of the deconstruction and reconstruction of a grayscale image from the first, first two, first ten, and then first 100 modes.

The original image of a dragonfly can be seen to have complex features and details with some clear primary structures. The first mode shows a strong, thin vertical section at the center of the image with two parallel, prominent features extending horizontally. With knowledge of the original image, one identifies the body and the wings as these primary features identified in Mode 1. Considering the sum of the first two modes in the next sub-figure, details emerge on the tail section that is narrower than the body section, the head is distinguishable from the main body, and the wings begin to take shape and are seen to converge at the body section. The far right sub-figure illustrates that adding the next 98 most significant modes to the first two modes does very little to reveal fundamental structures and principal components, but rather only fills in fine details with rapidly diminishing significance. In fact, the reconstructed image only reproduces the original image when the number of modes added equals the largest dimension of the image matrix. In this thesis, the same method will be applied to deconstruct the less-obvious, dynamic near-body flow field for both instantaneous and cycle-averaged variables.

The singular value decomposition orders the modes according to their significance. Furthermore, the level of significance in terms of "percentage of information" may be computed. Both the SVD modes and the associated significance rankings are reported for period-averaged flow fields.

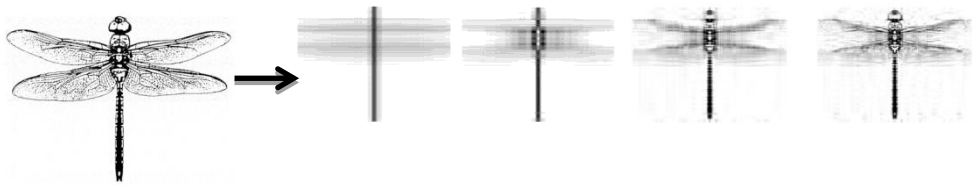

**Figure 3.3: Principal component analysis of Dragonfly image (far left), and decompositions into Modes 1, 1-2, 1-10, and 1-100 (second left to right).**
(Source: http://en.wikipedia.org/wiki/Green_Darner, *Anax junius, public domain*)

# 4. Results and Analysis

By using the methods described in the previous chapter, sets of numerical experiments for certain parameter combinations of interest were conducted to investigate the influence of the different parameters on the system dynamics and performance. A total of 36 numerical simulations were run in sets ranging from 4 to 12 simulations per set depending upon available resources and desired parameter resolution. Results with distilled summaries of performance metrics, flow fields, analysis and correlations are presented in the following sections of this chapter.

## 4.1. System with Damping and Resonance Forcing

Simulations were run for a flexible wing flapping forced at system resonance with torsion damping factors of 0.5, 0.7, 1.0, and 1.1. The angular displacement was significant at the lightest damping factor considered, 0.5, as seen in Figure 4.1 with negative lift produced for all cases; hence, no lower damping factor cases were considered. An upward trend in performance metrics at the high end of the initial series prompted an additional set of investigations with damping factors of 1.5, 2.0, 3.0, and 5.0; positive lift was achieved for all cases in this second series of numerical experiments.

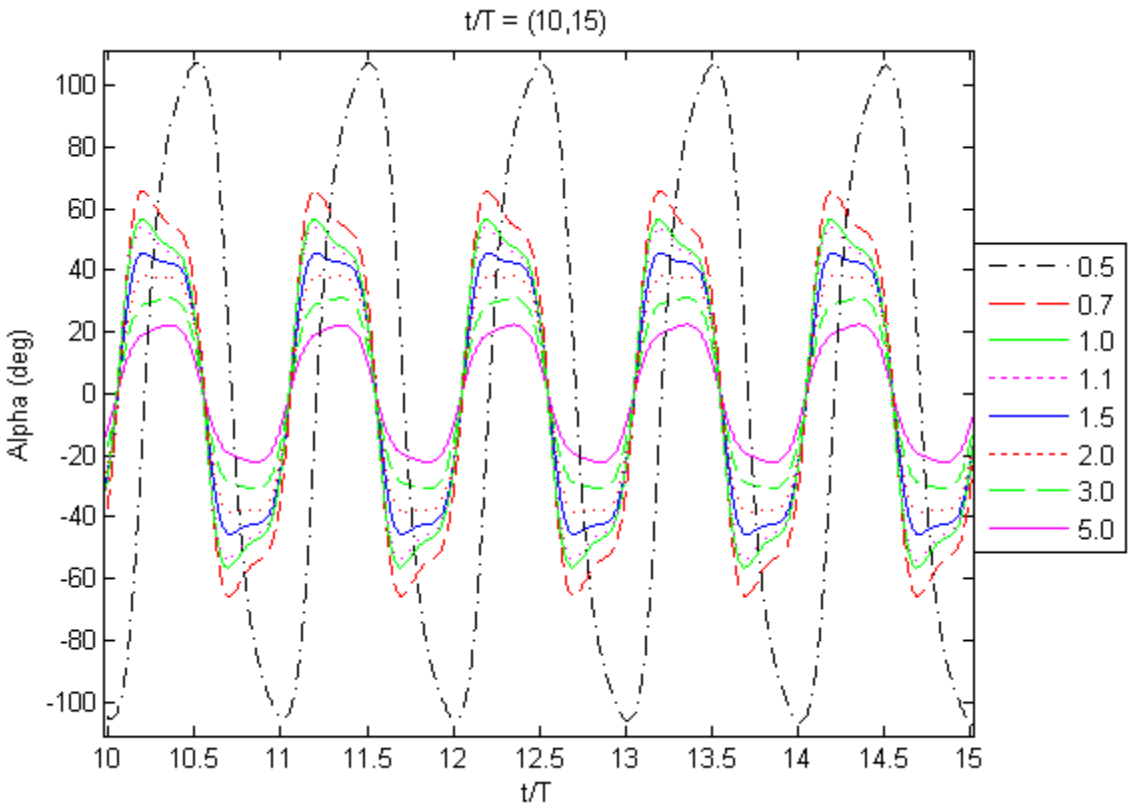


**Figure 4.1: Steady state angular displacement of free link. From largest to smallest amplitude, damping factor values: 0.5, 0.7, 1.0, 1.1, 1.5, 2.0, 3.0, and 5.0.**

### 4.1.1. Performance Metrics

The lift coefficient plot presented in Figure 4.2 is illustrative of the negative lift observed for the first series of damping factors considered with a near-zero lift produced for a damping factor 1.1 and a positive slope for the first four cases. This trend prompted another set of numerical experiments with the significantly larger damping factors of 1.5, 2.0, 3.0, and 5.0. It is noted that the inherent structural damping factors for conventional homogeneous materials are on the order of 0.01 to 0.1; hence, practical implementation of these simulated conditions would require a system or component specifically intended to provide these high damping factors. As expected from the initial series, the upward lift

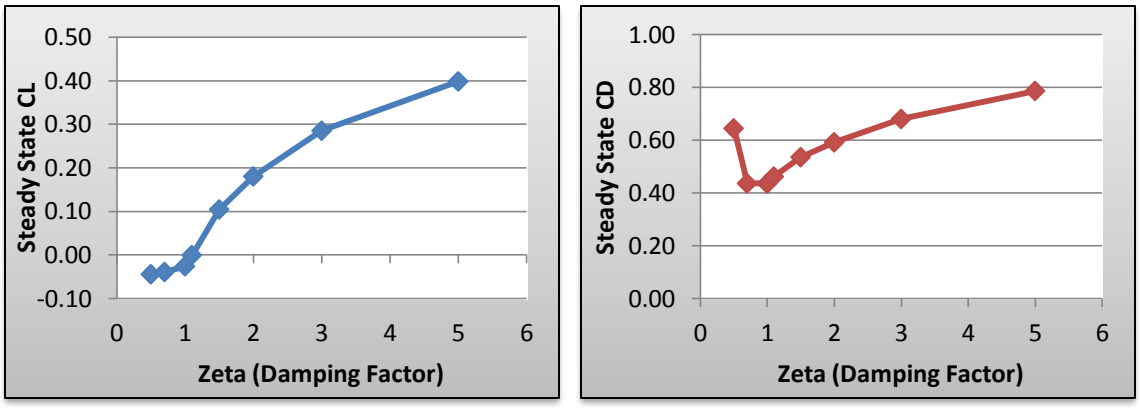


**Figure 4.2: Cycle-averaged steady state lift coefficient (left) and cycle-averaged steady state drag coefficient (right).**

trend continued and increasing positive lift was obtained for lift coefficients between 1.5 and 5.0. The rate at which the positive lift grows with respect to the damping factor is observed to decrease beyond a damping factor of 1.1. This diminishing performance increase suggests that the lift coefficient may level off to a finite value as the damping factor is increased towards infinity.

The cycle-averaged lift and drag coefficients are presented as a function of damping factor in Figure 4.3 on the same scale for better resolution and a more direct comparison. The positive trend in the lift coefficient for sub-unity damping factors is apparent and there is an inflection point around 1.1 and an upward trend as the damping factor is increased. The drag coefficient shows a similar trend for damping factors above 1.1, suggesting that the lift-to-drag ratio would level off as well. The complexity of the curves in the simulated cases relative to well-behaved and well-understood elementary functions suggests that there is much more information to consider in the flow field in order to draw fundamental relationships than simply the net cycle-averaged forces on the body's surface. The lightest damping case considered produced large angular

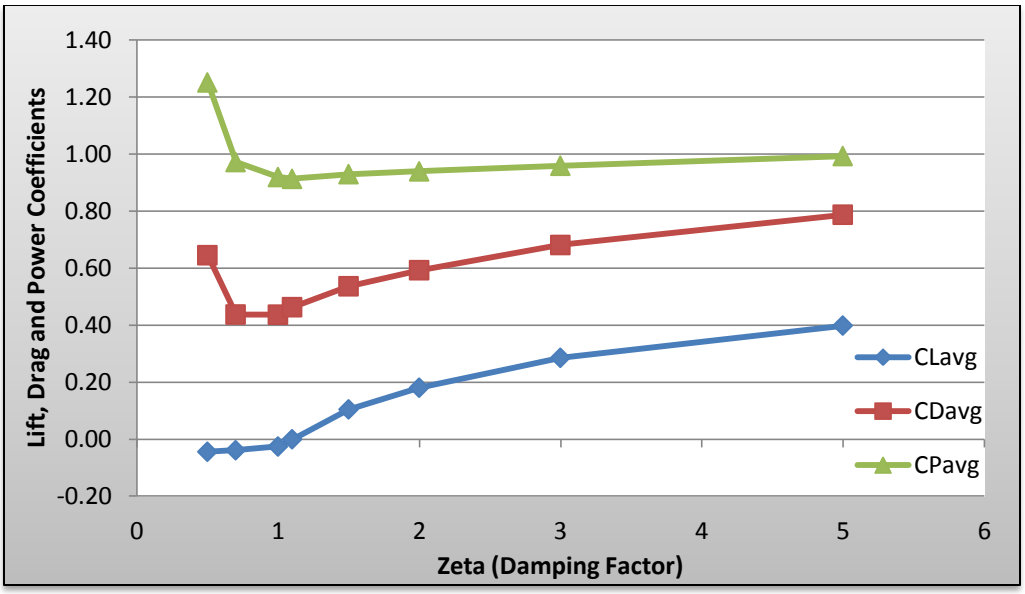


**Figure 4.3: Cycle-averaged steady state lift coefficient (blue), drag coefficient (red), and power coefficient (green).**

displacements in the free link of the wing, on the order of 110°, which may be causing the high drag during flapping. As the damping factor is increased, the angular displacement decreases to more intuitively aerodynamic ranges and the structural compliance in the system allows a minimum in drag between damping factors of 0.7 and 1.1. Snapshots of the wing profile during maximum angular displacement during steady flapping are presented in Figure 4.4 to visually convey why damping factors below 0.5 were not considered.

The lift increases at a decreasing rate as the damping factor is increased. As the damping factor increases further, the drag increases. One would expect the flexible wing to approach the performance of a harmonically oscillating rigid plate under the same conditions at the limit of the damping factor approaching infinity. This is demonstrated in Figure 4.5 with the lift-to-drag ratio, where the value at the far right is the case for a rigid

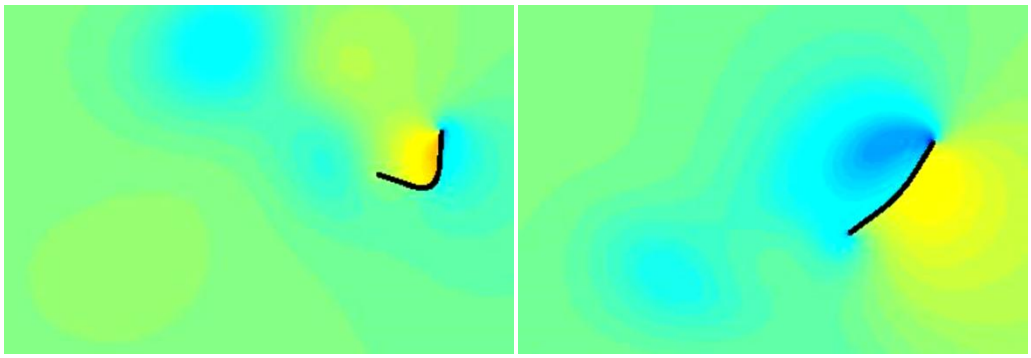

**Figure 4.4: Steady sate maximum angular displacement of free link pressure contour (-1 , 1) snapshot; damping factor 0.5 (left) and 5.0 (right).**

wing computed in earlier work (Fitzgerald *et al*., 2011). The drag coefficient in all cases presented is significantly higher than the lift coefficient, with a curious minimum between the damping factors of 0.7 and 1.0. Unfortunately, this minimum in drag corresponds to a lift coefficient of approximately zero; hence, from the lift-to-drag ratio curve in Figure 4.5, it can be stated that there is no practical benefit or significance to this minimum under these simulated conditions in terms of performance.

Assuming a valid extrapolation beyond a damping factor of 5.0, one may interpret the distilled performance metrics of the simulation set as an assertion that a flexible wing flapping at linear system resonance can at best only approach the lift and lift-to-drag ratio performance of a rigid wing under the specified conditions. Implications of this result are that insects flying under similar conditions likely do not flap near resonance as the amount of structural damping available in conventional mechanical or biomaterials would not allow positive lift production. Additionally, it is recommended MAVs not be designed to operate with flexible wings near resonance unless near-rigid behavior of the wings can be achieved with sufficiently high structural damping.

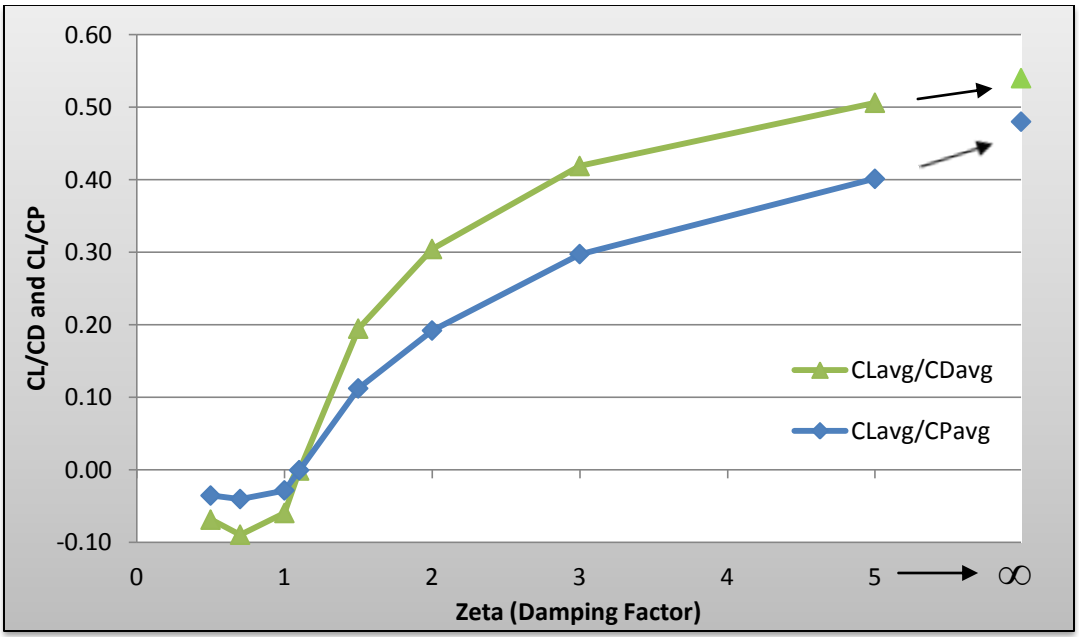


**Figure 4.5: Average steady state lift-to-drag and lift-to-power ratios.**

## 4.2. System with Damping and Forcing Below Resonance

Representative cases with damping below resonance were simulated for frequency ratios of 1/3 and 1/4. The lift coefficient, presented in Figure 4.6, was found to decline with increasing damping factor for both frequency cases and all damping factor cases considered. The highest lift performance occurs for zero structural damping for these cases below resonance, and the lift produced falls off sharply for small deviations from zero and begins to level off for high damping factors. The power and drag coefficients for both cases below resonance are shown to reduce with increasing damping factor, presented in Figure 4.7. A possible explanation for this benefit is the damping of large amplitude deformation caused by structural inertial forces and, to a lesser extent, fluid forces. This resulting smaller free-link amplitude may require less energy for the

wing to be driven through the fluid. The frequency ratio of 1 is included in the figure for more complete treatment and to show the context of frequency ratio 1/3 and 1/4 results.

The reduction in the power coefficient suggests that structural damping may be beneficial for average-power-constrained systems, particularly those that flap at a frequency ratio of 1/3. Introducing a damping factor of just 0.1 reduces the power

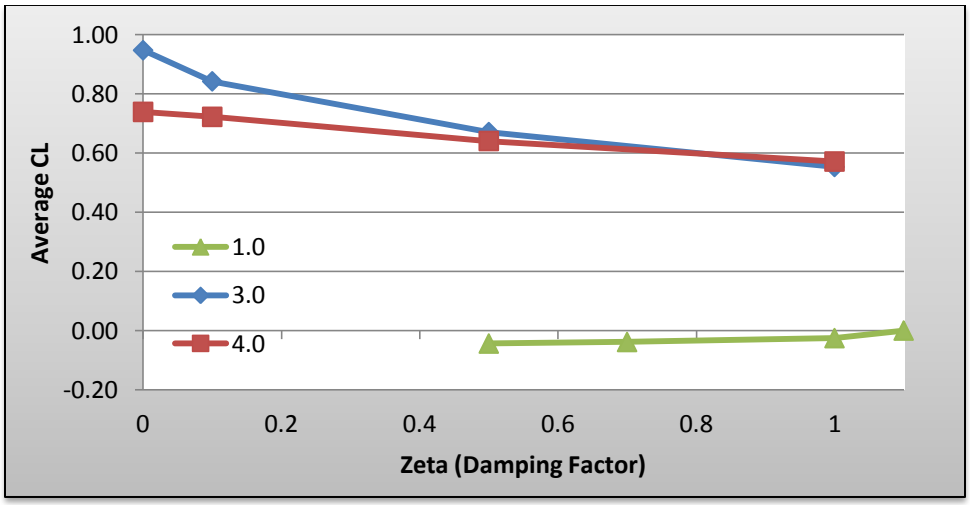


**Figure 4.6: Average steady state lift for different damping factors and inverse frequency ratios W1, W3, and W4.**

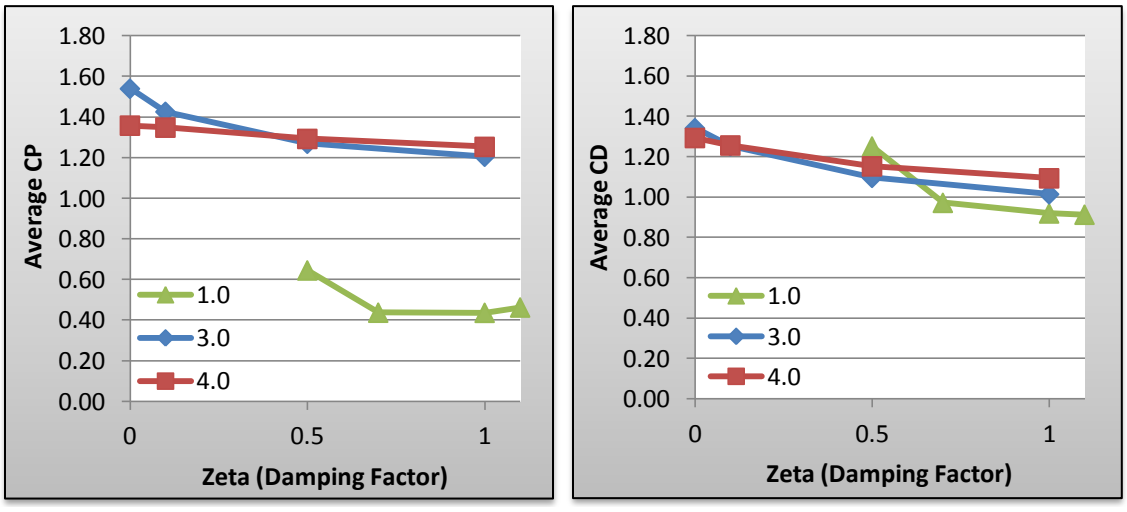


**Figure 4.7: Average steady state power coefficient (left) and drag coefficient (right) for different damping factors and inverse frequency ratios W1, W3, and W4.**

requirement by over 7%. Heavy structural damping that achieves a damping factor of 1.0 results in an input power requirement reduction of 22%. Unfortunately, the reduction in lift outweighs the reduction in power for increasing damping, illustrated in Figure 4.8.

The efficiency measures of lift-to-power and lift-to-drag depicted in Figure 4.8 decrease with increasing damping for the cases considered of flapping below resonance. There appears to be no net lift improvement for any non-zero damping factor for these cases and, while the power required decreases, the efficiency ratios convey a net disadvantage.

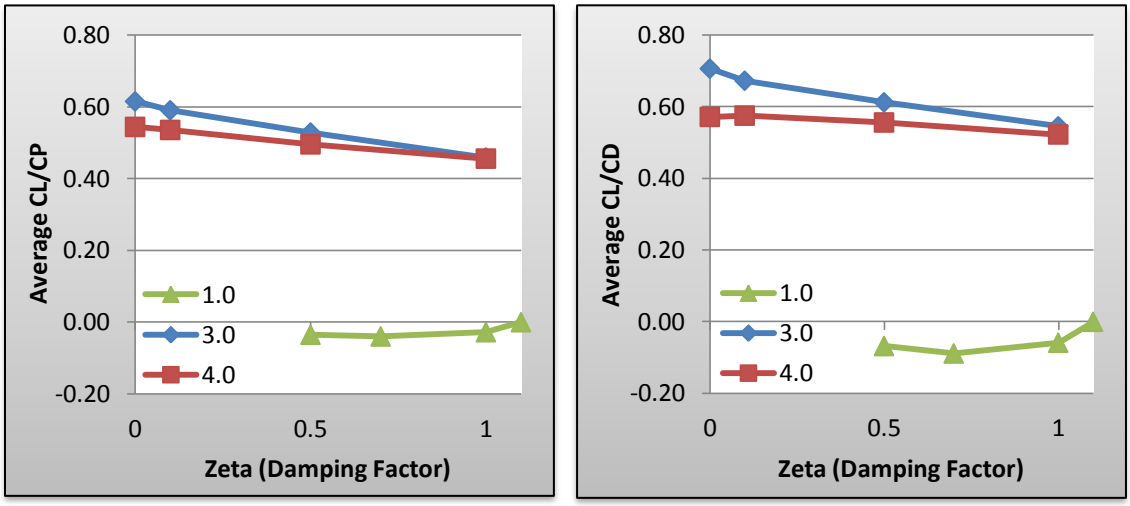


**Figure 4.8: Average steady state lift-to-power coefficient (left) and lift-to-drag coefficient (right) for different damping factors and inverse frequency ratios W1, W3, and W4.**

## 4.3. Asymmetrical Flexible Wings

Numerical simulations for flapping wings were conducted with varied leading link lengths and frequency ratios to determine the effect of asymmetrical flexibility for a single degree-of-freedom system. All prior research group efforts to this point have considered symmetrical links (Vanella *et al*., 2009a; Vanella, *et al*., 2009b; Fitzgerald *et al*., 2011; Fitzgerald *et al*., 2012). These studies identified a natural-to-forced frequency ratio of 1/3 as a preferred point for peak lift production and peak efficiency in lift-to- drag and power ratios across Reynolds numbers of 75, 250, and 1000 by using DNS, and inviscid flow by using the Unsteady Vortex Lattice Method (UVLM). A goal of the reformulation and parameters in the present work is to investigate the validity or universality of this apparent preferred efficiency point under further varied conditions.

Numerical experiments were performed for leading link lengths of 0.10, 0.25, 0.50, and 0.75 with zero structural damping. The simulated wing decays from rest to steady flapping in 5 periods, 3 periods are allowed for the fluid to dissipate transient behavior and reach a steady state at Reynolds number of 75; the resulting "steady state" data is presented for periods 8-12. Cases are identified with parameter combinations of W#A## where "#" corresponds to the inverse of the forced-to-natural frequency ratio and "##" corresponds to 100 × the leading link length. For example, W2A75 identifies the frequency ratio of one half and a leading link length of 0.75.

Initially, the model kinematics was provided for driving at the hinge point for symmetrical links. For asymmetrical links, the kinematics was translated to the peak of the leading edge so that all cases would have identical leading link and leading edge kinematics. It is noted that A = 0.5 corresponds to conditions of previously performed

numerical experiments, which are repeated here and compared to previous results to verify the correct implementation of the kinematics translation from the hinge point to the leading edge. Current performance metrics results were found to match previous results to two significant figures or better. Representative flow field snapshot time lapse plots are given for vorticity contours for case W3A25 in Figure 4.9. Similar flow field time-lapse plots can be seen for pressure, vorticity and magnitude velocity in Appendix A.

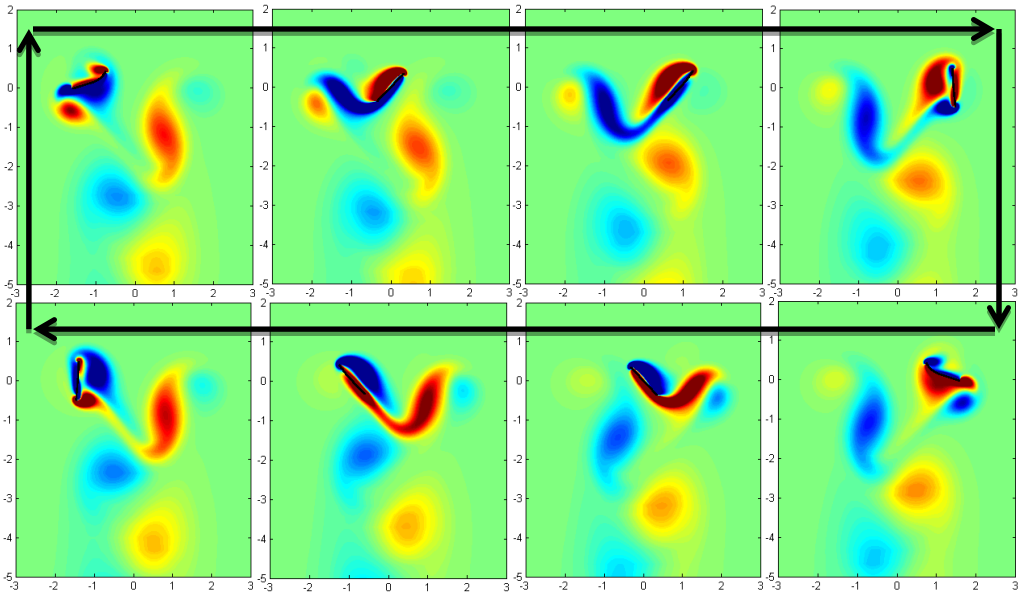

**Figure 4.9: Case W3A25 vorticity contour (-3, 3) time lapse for frame interval T/8 on truncated domain (-3,3)×(-5,2) for one period. *Arrow indicates direction of time evolution*.**

### 4.3.1. Performance Metrics

It is important to distinguish here between the variables and fixed quantities for comparative design purposes of particular systems. A fixed Reynolds number implies that, for a particular fluid and fixed structural system, a faster flapping frequency which produces a higher characteristic velocity is counteracted by a smaller chord. An insect in

flight that begins flapping faster, for example, has increased its Reynolds number as well as its frequency ratio. Therefore, for fixed wing and fluid properties, varying the flapping frequency or frequency ratio will vary the Reynolds number. Alternately, active stiffness control of a wing can be employed, which would help maintain the same flapping frequency; the stiffness properties would be varied to vary the fundamental natural frequency, thereby altering the frequency ratio while maintaining the same characteristic speed and Reynolds number for fixed wing geometry. A system that employs constant frequency with active stiffness control is a practical suggestion that one can come away with from the results presented in the case studies of this section.

A more involved implementation to make full use of the results obtained is to create a wing with a variable leading length and free section length. For fixed spatial kinematics, the leading link can be reduced and the free link extended by using active chord length control in order to transition between cases with desired performance as summarized below. Although technically valid, the latter possibility for implementation of these results is far more laborious; hence, the former interpretation is preferred for design considerations. Active stiffness control can be achieved by varying muscular or hydraulic resistance as well as variable stiffness springs through pre-loading or using electro-stiffening/electro-compliant materials.

The lift coefficient is plotted as a function of the normalized leading link length in Figure 4.10 for the four frequency ratio cases considered. First, it is noted that this set confirms the preferred frequency ratio of 1/3 for peak lift with symmetrical links, confirming previous findings. Asymmetrical links, however, show that a very slightly

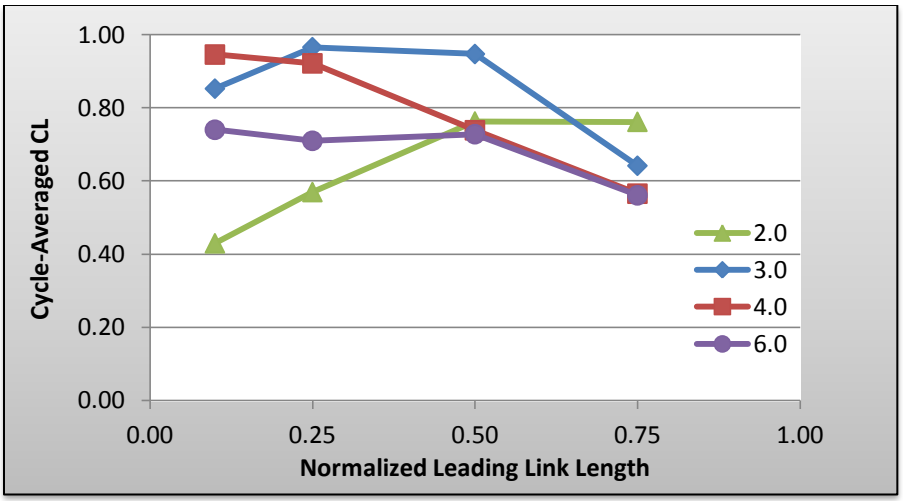


**Figure 4.10: Cycle-averaged steady state lift coefficient for different leading link lengths and inverse frequency ratios W2, W3, W4, and W6.**

higher lift can be achieved with a shorter leading link length of 0.25 at a frequency ratio of 1/3. Additionally, the frequency ratio of 1/4 achieves a very similar peak lift for a very short leading link length of 0.10. Therefore, very similar peak lift coefficients are shared and can be achieved by parameter combinations of W3A25, W3A50, W4A10, or W4A25.

Two frequency ratios are included in Figure 4.10 and several more link lengths that perform worse than these optimal cases. The cases with a frequency ratio of 6.0 were seen to provide relatively poor performance compared to the rest; yet these cases are fairly consistent for link lengths up to 0.5. Flapping a wing of the type presented whose leading link is shorter than its free link is expected to provide consistent results that are relatively insensitive to moderate link length variations. Contrary to the other three frequency cases, the ratio of 2.0 is associated with an increased lift as the leading link increases from 0.10 to 0.50, and increasing further to 0.75 yielded a negligible difference in performance. This is likely due to the large amplitude free link displacements for the

case close to linear system resonance forcing. As the free link length is reduced, the negative effect of its large angular displacement becomes less significant. In fact, in general, it can be seen that the shorter the free link, the less significant the performance difference is between the frequency cases. Intuitively, one would expect the performance of all frequency cases to converge further to the case of a single rigid wing as the free link length approaches zero.

For a frequency ratio of 2.0, a longer leading link produces more drag as seen in Figure 4.11. The effect of leading link length on drag production is mixed, but yet fairly consistent for other frequency ratios. However, the power consumption plot (Figure 4.12), exhibit a general trend across all cases of an increasing leading link length requiring more power input. This trend suggests that less strictly prescribed motion of a wing surface with more compliance in the chord direction is advantageous to minimize power consumption. This observation also provides a guideline for design of MAVs and understanding of flight methods in biological systems in the context of power consumption: an insect may produce more lift with a W3A25 configuration and an output power coefficient of 1.42; however, physiology may limit the average output power magnitude or the flapping frequency, in which case, a lower frequency ratio of 1/4 with an asymmetric wing can produce a similar lift coefficient with a small drop in the required output power coefficient.

Making use of the lift- and drag-coefficients provided in Figures 4.10 and 4.11, the ratio plot presented in Figure 4.13 is constructed. The frequency ratio of 3.0 is noted as the ratio associated with the highest overall performance and across most link lengths for this definition of performance efficiency. The lift-to-drag ratio is highest for a

frequency ratio of 1/3 across the majority of the considered wing geometries. Interestingly, the peak efficiency occurs for a leading link length of 0.25. For a frequency ratio of 1/4, the peak efficiency also occurs for a leading link length of 0.25. The compliant cases of 1/2 and the stiff cases of 1/6 both have peak performance for approximately symmetrical wings, within the resolution of the link lengths considered with assumed validity of interpolation. However, these peak values are still significantly lower than those obtained for the high lift cases of 1/3 and 1/4.

For conventional, steady, fixed-wing flight, the lift coefficient and lift-to-drag ratio are the golden standards used to characterize performance and efficiency. The lift coefficient is directly related to the lift capability of an airfoil of a steady-cruising, fixed-wing aircraft, the drag has a direct relationship to the power consumption, and the lift-to-drag ratio can be directly related to the distance traveled per unit of power consumed; or equivalently, the maximum steady cruising range for a fixed energy source. However, in

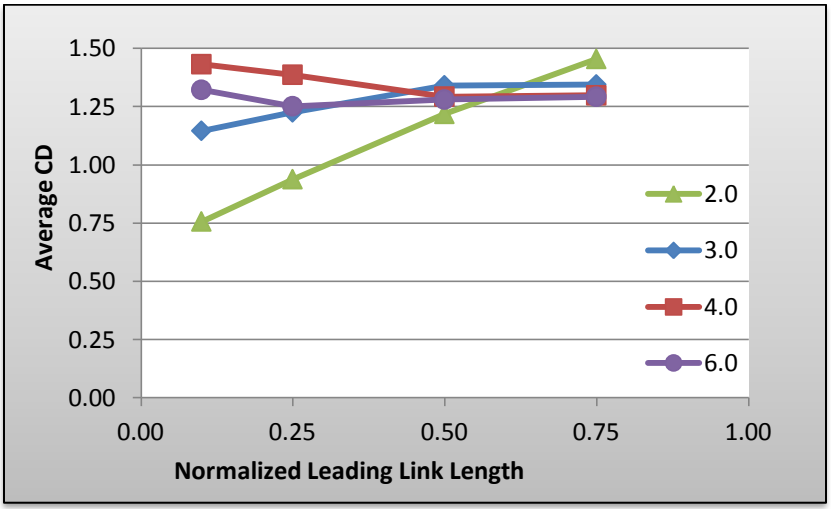


**Figure 4.11: Cycle-averaged steady state drag coefficient for different leading link lengths and inverse frequency ratios W2, W3, W4, and W6.**

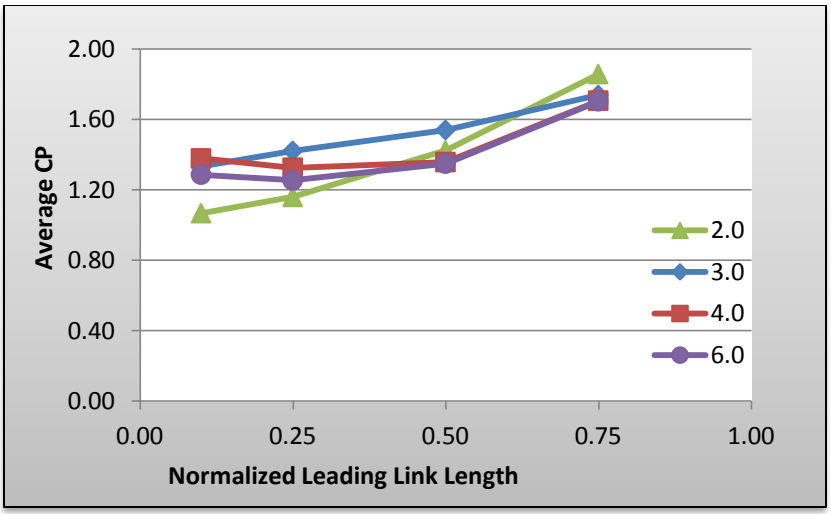


**Figure 4.12: Cycle-averaged steady state power coefficient for different leading link lengths and inverse frequency ratios W2, W3, W4, and W6.**

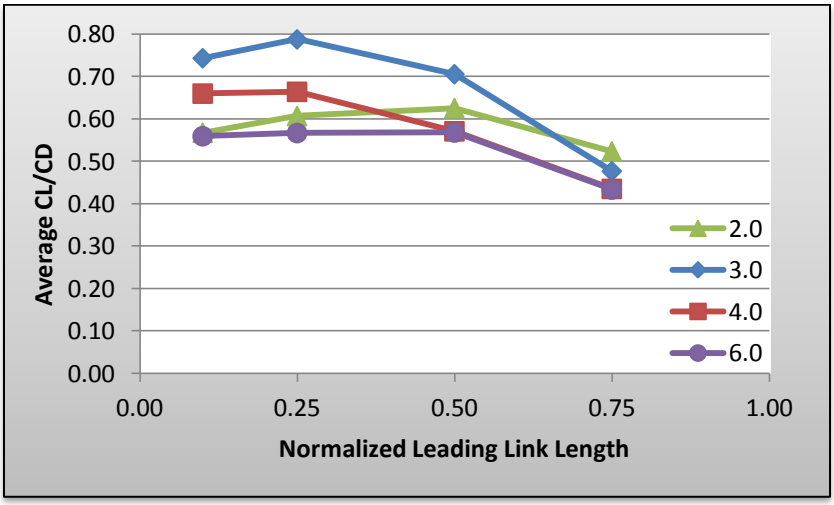


**Figure 4.13: Cycle-averaged steady state lift-to-drag ratio for different leading link lengths and inverse frequency ratios W2, W3, W4, and W6.**

flapping flight, lift forces and drag forces are not steady and the stroke reversal can require the wing to expend additional energy during rotation while also "capturing" some of the translational energy in the wake under the wing to enhance lift generation. Due to these additional features in the dynamics of flapping flight, drag forces cannot be directly

related to energy expenditure. Therefore, the lift-to-power ratio is considered rather than the lift-to-drag ratio as the primary indicator of performance efficiency.

When attempting to understand flight in biology, one must consider the evolutionary pressures that guide specific anatomy, control, or behavior. The lift capability can be considered as available general thrust, and the ability to quickly escape predators or pursue prey. The power coefficient can be considered as the metabolic rate relative to locomotion, and a higher rate of energy expenditure requires additional mobility for energy source consumption, which in turn requires more energy expenditure. When designing a MAV with a specific body mass and payload capability, the flight performance and duration must be optimized for a fixed energy supply, likely a chemical battery. In Figure 4.10, the parameter combinations of W3A25, W3A50, W4A10, andW4A25 were identified as high lift cases, and in Figure 4.14, the performance is placed in the context of lift-to-power efficiency.

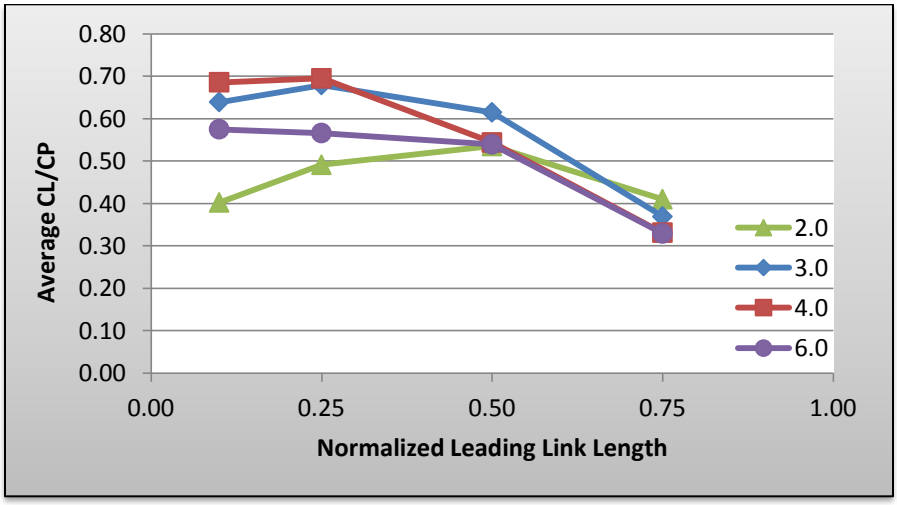


**Figure 4.14: Cycle-averaged steady state lift-to-power ratio for different leading link lengths and inverse frequency ratios W2, W3, W4, and W6.**

For the parameter combinations considered, the most advantageous frequency ratio is seen from Figure 4.14 to be 1/4, which is also the most sensitive to wing geometry. For the frequency ratio of 1/3, the system also performs well with a similar peak efficiency and the benefit of less sensitivity to link length. It is notable that for the leading link length of 0.25, one achieves the highest lift-to-power efficiency and the system performance is insensitive to moderate variations in link length and consistent for frequency ratios between 1/4 and 1/3. Given that wing geometry is likely fixed for practical MAV designs and biological systems, variations in kinematics and frequency ratio are the practical options for increasing thrust output and achieving high lift-to-power efficiency. Therefore, insensitivity to frequency ratio is strongly preferable.

For a system that maintains consistent spatial kinematics and only alters flapping frequency ratio, it is observed in Figure 4.10 that a flexible wing of the type considered in the present work with a $0.25L_C$ leading section and a $0.75L_C$ free section is capable of the highest lift production at a frequency ratio of 1/3, whereas the same wing geometry achieves the best lift-to-power efficiency for frequency ratios between 1/3 and 1/4. A flapping insect or MAV near Reynolds number 75 can produce maximum lift with minimal power output for a frequency ratio of 1/3 and reduce its frequency ratio to 1/4 to produce less lift while maintaining the same lift-to-power efficiency. For systems that vary widely in flapping frequency to control thrust produced, symmetric flexible wings display minimal sensitivity to flapping frequency with respect to efficiency, while providing significant control of lift production between frequency ratios of 1/4 and 1/3.

### 4.3.2. Frequency Analysis and Phase Plots

The significance of understanding frequency content in flapping systems is multi-faceted. First, the presence of certain frequencies manifested in the structural response may be correlated to performance in terms of thrust, power, or efficiency measures. Second, high-frequency content may indicate corresponding excessive power exertion or high amplitudes that can be modified through structural damping. Third, when controlling a dynamic system, angular positions and velocities are practical to measure and analyze in real time with on-board sensors and processing. A system may be able to predict control responses or modify control commands based on feedback received from free-link displacement measurements if known correlations to performance metrics exist. Additionally, the reduction of a high-dimensional, complicated system such as flapping flight into further perspectives through analysis provides a much greater chance of understanding and decoding the complicated physics into meaningful and useful high level interpretations.

The paths produced for the free links provide intricate phase plots that are clearly affected by high dimensional features in the fluid domain. The prescribed angle of attack for the leading link, theta, is compared graphically with the free link angular offset, alpha, and its angular velocity in the following phase plots of Figure 4.15 across four different frequency ratios for a leading link length of $0.25L_C$.

The amplitude of theta, the driven link angle of attack, is prescribed according to the kinematics. The amplitude of the relative free link displacement is observed to decrease as the stiffness of the torsion spring increases; or equivalently, as the frequency ratio is increased. This result is intuitively expected. The angular velocity plot displays

smooth, yet higher frequency content with amplitudes that are less affected by frequency ratio toward the compliant range. In the phase plot associated with the free link provided in the last row of Figure 4.15, one notices that the higher lift production and higher lift-to-power efficiency cases have smoother and soft transitions whereas the low-performance cases of high stiffness and high compliance cases have sharp transitions in angular velocity near zero angular displacement. The comparisons imply that sharper transitions result in lower lift production and higher energy expenditure to achieve such a rapid directional change in a moderately viscous fluid. From a comparison of the phase plots in Figure 4.15 with the lift coefficient in 4.6 and the lift-to-drag coefficient in 4.9 for the case of $0.25L_C$, one sees that in order of decreasing lift, the flapping frequencies can be ranked as W = 3-4-6-2 and in order of decreasing lift-to-power ratios, the flapping frequencies can be ranked as W = 4-3-6-2. For both performance metrics, soft transitions in the $\alpha - \dot{\alpha}$ curves correspond to high lift and high lift-to-power efficiency.

Fast Fourier transforms (FFTs) of the angular offset position $\alpha$ time history and angular velocity $\dot{\alpha}$ time history of the free link can provide further insights into the system dynamics. The frequency analysis can be used to understand how higher order effects in the flow field become manifested in the structural response. The steady state variable data is processed for two periods and made dimensionless by multiplying frequency values by the period of flapping. The case corresponding to highest performance in terms of lift-to-power is chosen as the first full example for this analysis and the associated results are shown in Figure 4.16. In this figure, single-period amplitude plots for $\alpha$ and $\dot{\alpha}$ and their FFT plots are shown.

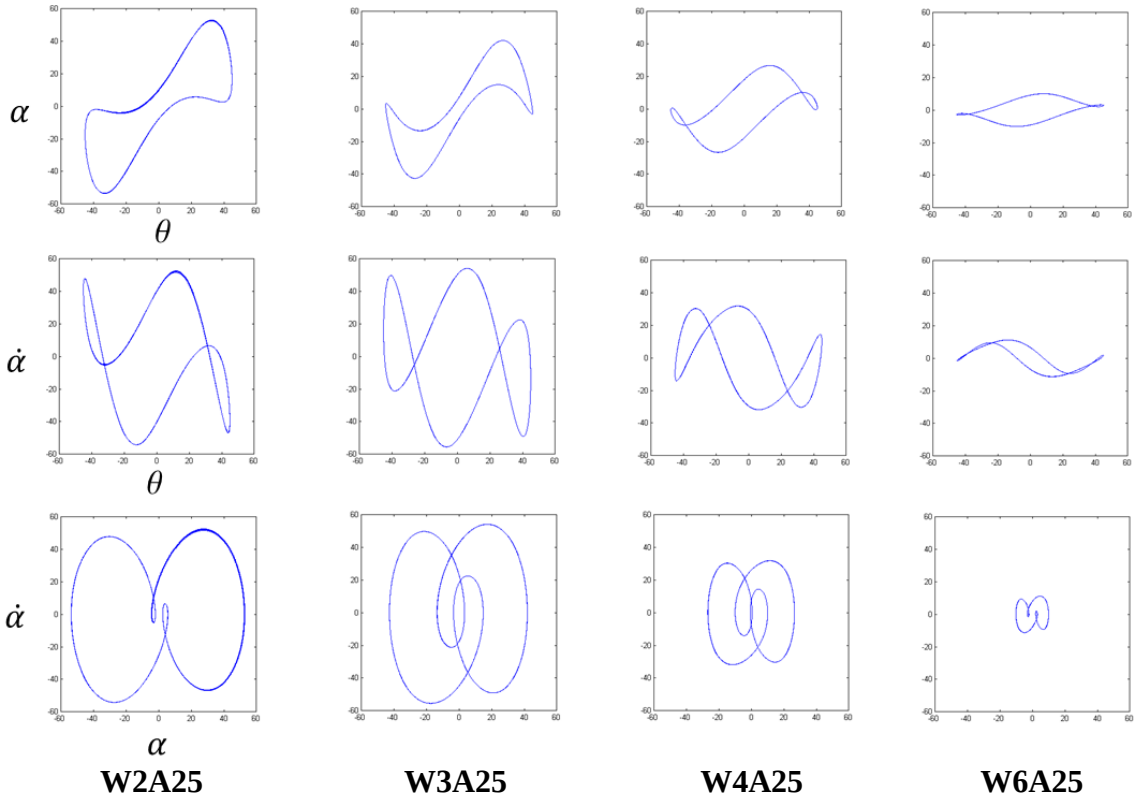


**Figure 4.15: Steady state phase plots for $\theta$, $\alpha$, and $\dot{\alpha}$ with different frequency ratios. For all plots, the domain is (-60°,60°)×(-60°,60°) and t/T = (10,12).**

The first interesting feature to notice is the prominence of the odd frequency content. In particular, the first and third harmonics are especially significant in the $\alpha$ FFT, and to a lesser extent, the fifth harmonic. The presence of first, third, and fifth harmonics and, to a lesser extent, the seventh harmonic are evident in the $\dot{\alpha}$ FFT. The peaks at the first, third, and fifth harmonics in the $\alpha$ and $\dot{\alpha}$ responses are observed for all parameter cases considered. Above the fifth harmonic, the spectral amplitudes die off rapidly to noise levels. Beyond the seventh harmonic, no prominent peaks were found above the background or average noise levels. Therefore, the FFT plots presented are truncated for up to the tenth harmonic. A subset of the parameter combination cases

simulated has been presented in the current section, and the complete set of FFT plots for frequency cases of 2, 3, 4 and varied link lengths can be found in Appendix A.

A cutoff value is selected for performance metrics in order to analyze the top few performance cases in terms of the spectral content and to look for similarities and draw correlations. Lift coefficients above 0.9 are achieved for cases W3A25, W3A50, W4A10, and W4A25, as shown in Figure 4.6. Lift-to-power ratios above 2/3 are obtained for W3A25, W4A10 and W4A25, as shown in Figure 4.14. The intersection of these two sets comprises the cases of primary interest; that is, W3A25, W4A10, and W4A25. The FFT plots of $\alpha$ and $\dot{\alpha}$ histories for these three cases are presented in Figures 4.17 – 4.19.

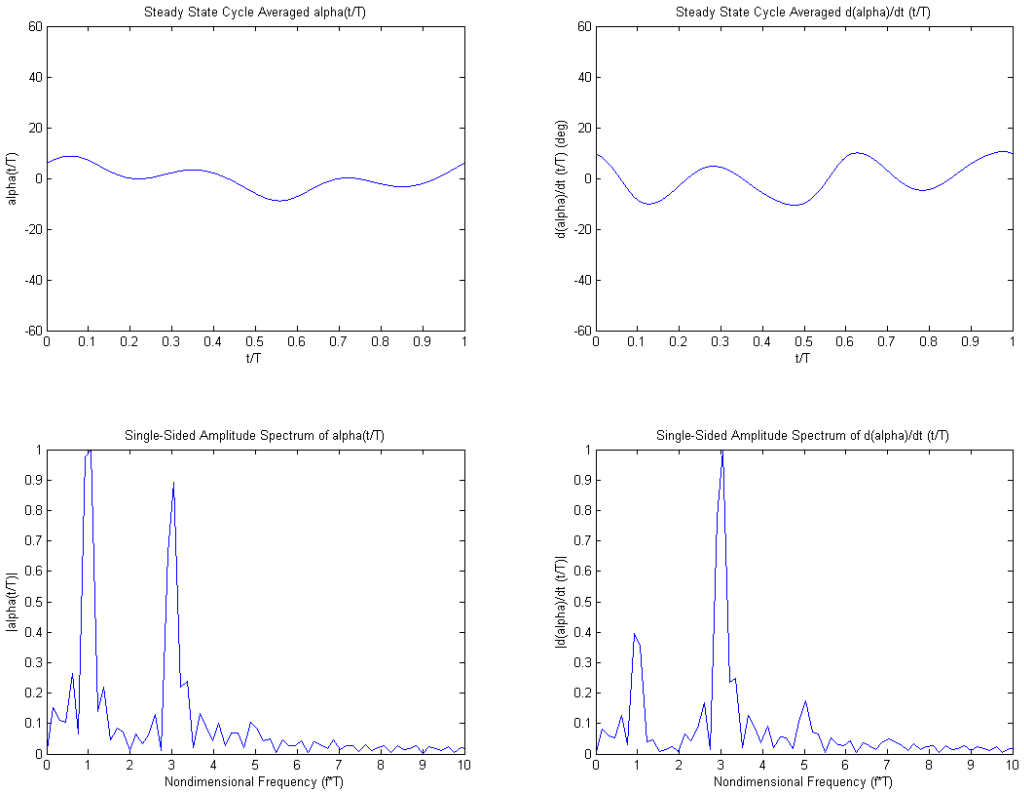


**Figure 4.16: Steady state responses and associated FFTs of $\alpha$ (left) and $\dot{\alpha}$ (right) for Case W4A25. Amplitudes have been normalized by maximum magnitude component value.**

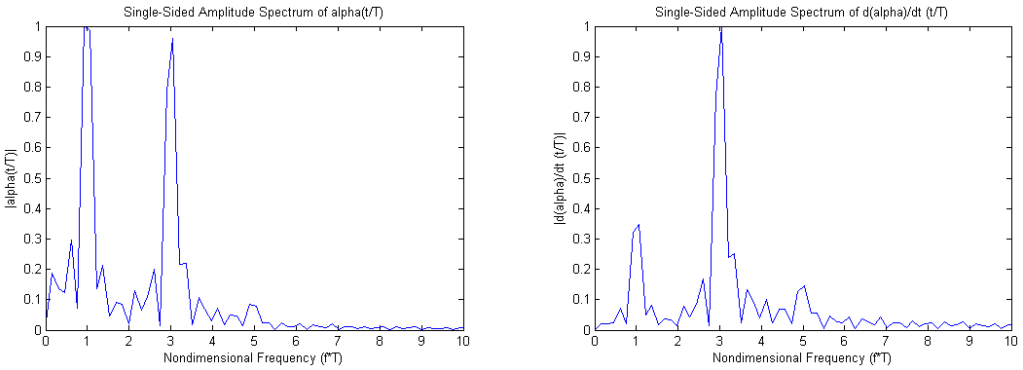


**Figure 4.17: FFTs of $\alpha$ (left) and $\dot{\alpha}$ (right) steady state histories for Case W3A25. Amplitudes have been normalized by maximum magnitude component value.**

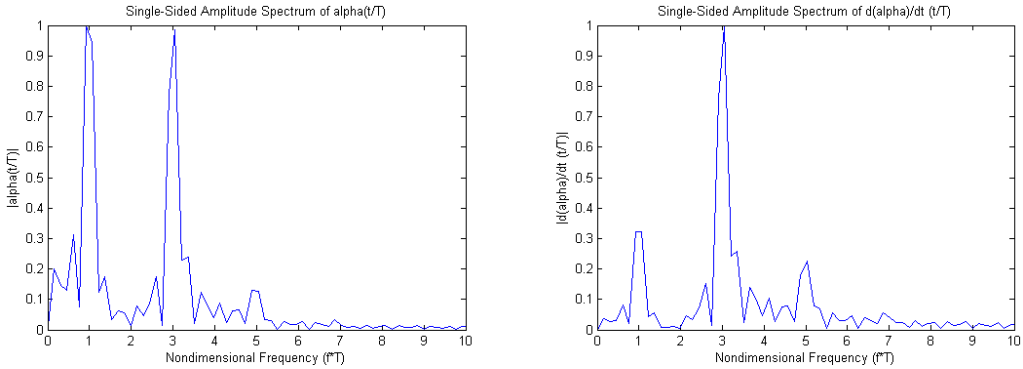


**Figure 4.18: FFTs of $\alpha$ (left) and $\dot{\alpha}$ (right) steady state histories for Case W4A10. Amplitudes have been normalized by maximum magnitude component value.**

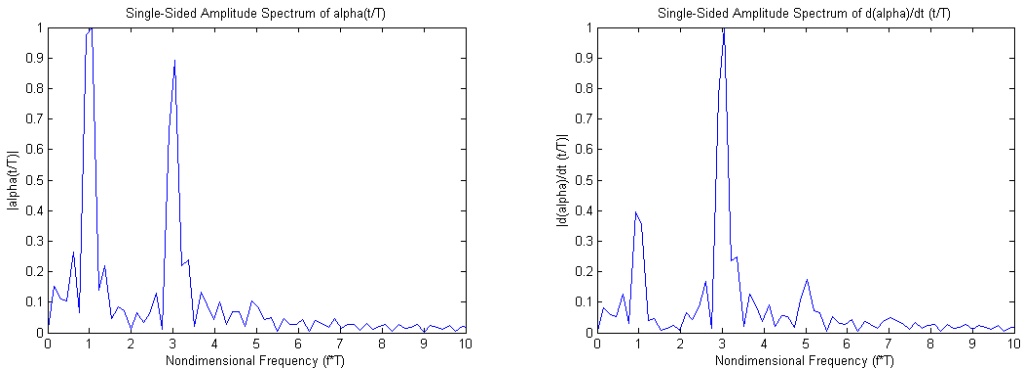


**Figure 4.19: FFTs of $\alpha$ (left) and $\dot{\alpha}$ (right) steady state histories for Case W4A25. Amplitudes have been normalized by maximum magnitude component value.**

All three cases corresponding to high performance show common spectral characteristics. Prominent peaks at the first and third harmonics are present in the $\alpha$ response. All higher order spectral components have normalized magnitudes less than 0.1, suggesting that this is a significant indicator of high performance for one or both of the metrics considered. Similar characteristics are also observed in the $\dot{\alpha}$ FFT plots. The spectral peak at the third harmonic is the strongest, with the first harmonic being the next strongest with a normalized amplitude around 0.3-0.4, followed by the fifth harmonic which has a normalized amplitude around 0.15-0.20. All higher order spectral components have normalized magnitudes below 0.1. In order to further validate these common magnitude proportions, two of the lowest performing cases W2A10 and W3A75 are contrasted. The FFTs of the $\alpha$ and $\dot{\alpha}$ responses for these two low performance cases are presented in Figures 4.20 and 21 below for comparison with the results displayed in Figures 4.17 to 4.19.

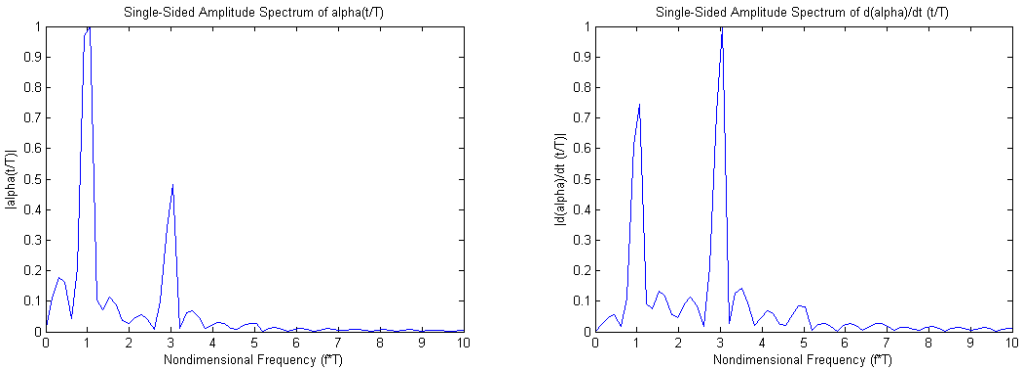


**Figure 4.20: FFTs of $\alpha$ (left) and $\dot{\alpha}$ (right) steady state histories for Case W2A10. Amplitudes have been normalized by maximum magnitude component value.**

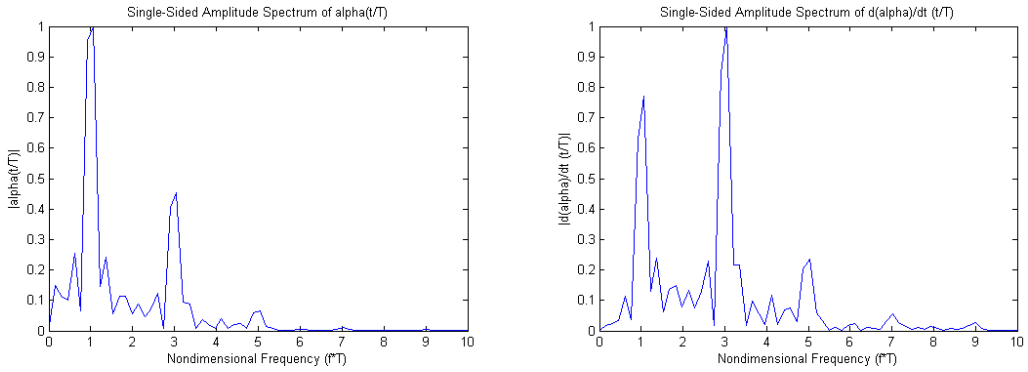


**Figure 4.21: FFTs of $\alpha$ (left) and $\dot{\alpha}$ (right) steady state histories for Case W3A75. Amplitudes have been normalized by maximum magnitude component value.**

Moderately different spectral profiles are observed for the two typical low performance cases presented in Figures 4.20 and 4.21 when compared to the high performance cases presented in Figures 4.17, 4.18, and 4.19. One first notices the presence of odd harmonics, which is observed in all cases considered. Upon closer inspection, the $\alpha$ plots show a significantly lower magnitude at the third harmonic, whereas for the high performance cases the magnitudes at the first and third harmonics are very similar. The $\dot{\alpha}$ FFT plots show relative spectral component ratios that are significantly different than those observed for the high performance cases, for which the first harmonic has a much high magnitude and the fifth harmonic magnitude is a lower fraction of the magnitude of the first harmonic.

While all of the FFT plots of the steady state structural response of $\alpha$ and $\dot{\alpha}$ have common spectral components present, the high performance cases have specific relative magnitudes of specific spectral content. It is important to note that the absolute magnitude of $\alpha$ and $\dot{\alpha}$ responses do not appear to have an effect on the performance; only the relative magnitudes of the spectral components. Therefore, the case-normalized

FFT plots are presented in this section. For example, the angular displacement response for a forcing frequency ratio of 1/3 is greater than that for a forcing frequency ratio of 1/4 since the system is being excited closer to a nonlinear resonance, but the cases with similar case-normalized FFT profiles have similar characteristics on the low- and the high-performing ends. These trends suggest that active control at the flexible joint that *imposes* the presence of beneficial spectral content may enhance system performance and is worthy of future investigation.

### 4.3.3. Near-Body Flow Field

The structural performance metrics and angular response data have the advantage of being real-time measurable quantities. In addition, the near-body flow field possesses a significant amount of information that may only be distilled in the structural response data which obscures higher-dimensional details. Lift produced in flapping flight is primarily attributed to the downward fluid jet. The lift force per unit span produced during flapping can be explained by a balance of the rate of momentum transfer into the downward fluid jet; this is given by

$$\frac{\vec{F}_L}{L} = \frac{d\vec{p}_{fluid}}{dt}\frac{1}{L} = \frac{d(m_{fluid}\vec{\bar{v}}_{jet})}{dt}\frac{1}{L} = \frac{d(\rho_{fluid}V_{fluid}\vec{\bar{v}}_{jet})}{dt}\frac{1}{L} = \rho_{fluid}\vec{\bar{v}}_{jet}\frac{d(\mathrm{A}_{fluid})}{dt}$$

$$\Rightarrow \boxed{\frac{|\vec{F}_L|}{L} = \rho_{fluid}\left(|\vec{\bar{v}}_{jet}\cdot\vec{\bar{v}}_{jet}|\right)w_{jet}} \doteq \frac{N}{m} \qquad (4.1)$$

Here, $\vec{F}_L / L$ is the lift force per unit span of the wing, $\vec{p}_{fluid}$ is the linear momentum of the fluid, $m_{fluid}$ is the mass of the fluid in volume $V_{fluid}$, $\rho_{fluid}$ is the density of the fluid and *t* is time. $\mathrm{A}_{fluid}$ represents the cross-sectional area of the region of the fluid jet

considered with width $w_{jet}$ and average velocity $\vec{\bar{v}}_{jet}$. The strength of the lift produced is therefore predicted to correlate directly to the width $w_{jet}$ and the square of the fluid jet velocity magnitude. Given that the above equation does not account for the effects of vorticity or the dissipation of viscosity, it is not clear whether the prediction from equation (4.1) will exactly match the measured strength and size of the fluid jet.

The near-body flow field is deconstructed into primary components via Singular Value Decomposition (SVD) for the vertical velocity, horizontal velocity, and the vorticity for period-averaged structures. It is notable that the average of the SVD of each snapshot is *not* equivalent to the SVD of the period-averaged snapshots; therefore, the SVD plots presented in this section are the average of the SVD of each of the 20 snapshots obtained individually per period. The primary mode in each case exposes the significant features in flow field relative to the variable deconstructed. An example of the primary velocity deconstruction is presented for the case W3A75 in Figure 4.22. The vertical velocity primary mode prominently exhibits significant structures identified as the central vertical fluid jet and the end of stroke vortices. The primary mode of the horizontal velocity exhibits features identified as the trailing edge vortices and the vortex street known to surround the vertical fluid jet.

It is worth mentioning the different signs of the regions of concentrated vertical velocity shown in Figure 4.22. While the central vertical fluid jet is clearly downward, the symmetrical end of stroke vortices at the top periphery of the central jet suggest a detrimental transfer of energy into the fluid; the upward velocity imparted into the end of stroke vortices would cause a downward force which reduces the lifting effect of the strong central fluid jet. The horizontal velocity contours display strongly opposing

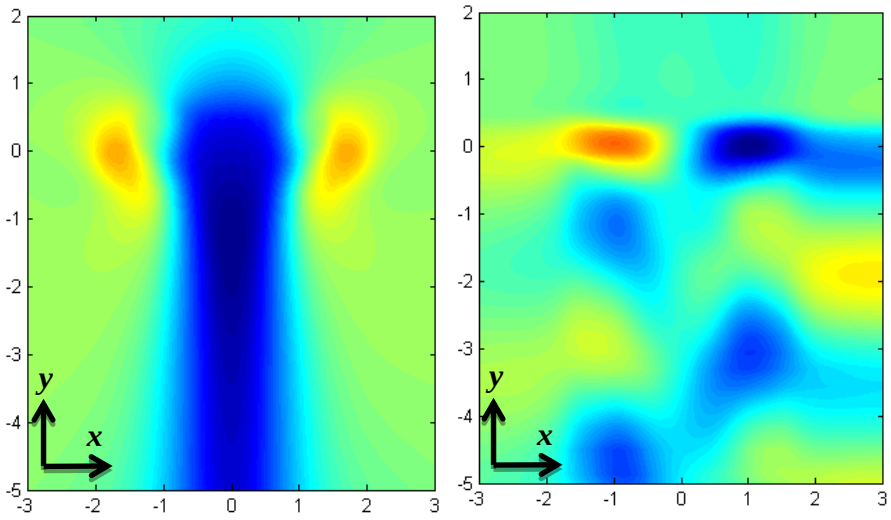


**Figure 4.22: Steady state SVD Mode 1 for Case W3A75:**
**Vertical velocity (left) and horizontal velocity (right) for (-3,3)×(-5,2) domain.**
**Amplitudes have been normalized by maximum magnitude component value.**

regions of horizontal velocity in the dissipating vortex streets. However, these strong regions appear diametrically and they are equal and opposite to each other, suggesting that the net effect is zero for symmetric flapping at Reynolds number 75, as the net period-averaged structural force computations confirm for each case within 0.5%.

The complete cycle-averaged vertical velocity contours for leading link length A10 and various frequency ratios are presented in the right column of Figure 4.23. It is noted that the first mode of the vertical velocity SVD across all cases was found to contain 80% ± 2% of the total information relative to the total vertical velocity field period average. Additionally, the first ten modes of the vertical velocity SVD across all cases were found to contain over 98% of the vertical velocity flow field information. The SVD primary mode for each case is presented in the left of the same figure; this allows for a clearer comparison of the relative magnitudes of the opposing vertical velocity structures. Considering the strength and size of the period-averaged central fluid jets, one

may visually estimate that the performance ranking in order of increasing lift produced would be frequency ratio inverse W = 3-4-6-2, where 2 clearly has a much narrower and weaker fluid jet than the other three cases. Investigating the deconstructed first SVD mode, however, one begins to see the relative effects of the end of stroke vortices and the true significance or insignificance of their upward velocities. It is evident from the SVD Mode 1 plots that the upward velocity is far less significant than the period-averaged plots for W3 and W4, yet, far more significant for W2 and W6. From the SVD Mode 1 plots, one would estimate the performance ranking in order of increasing lift as W = 4-3-6-2. A re-examination of the $C_L$ plot shown in Figure 4.10 in Section 4.2.1 confirms this ordering and confirms the significant difference in performance evident in a visual comparison of the cases' SVD Mode 1 and Modes 1-10 of the vertical velocity.

The steady state cycle-averaged vorticity magnitude contours are presented in Figure 4.20 for a fixed forcing frequency ratio and varied leading link lengths on a truncated fluid domain. For this analysis, the vorticity was taken as absolute values in order to quantify the circulation in the domain as a sum of the magnitudes of all vortices. This procedure is done because counter-rotating vortices yield a net zero circulation. Additionally, the plots are scaled such that the open, stationary domain is black (zero vorticity) and the peak vorticity value over all cases is used to normalize all values so that the contours may be represented in grayscale. The 428×499 pixel images with grayscale magnitudes then represent the magnitude vorticity in the truncated, equi-spaced Cartesian domain. The average magnitude vorticity is then computed as the average of each pixel element and the total circulation on the domain is simply the sum of all element magnitudes for comparison purposes.

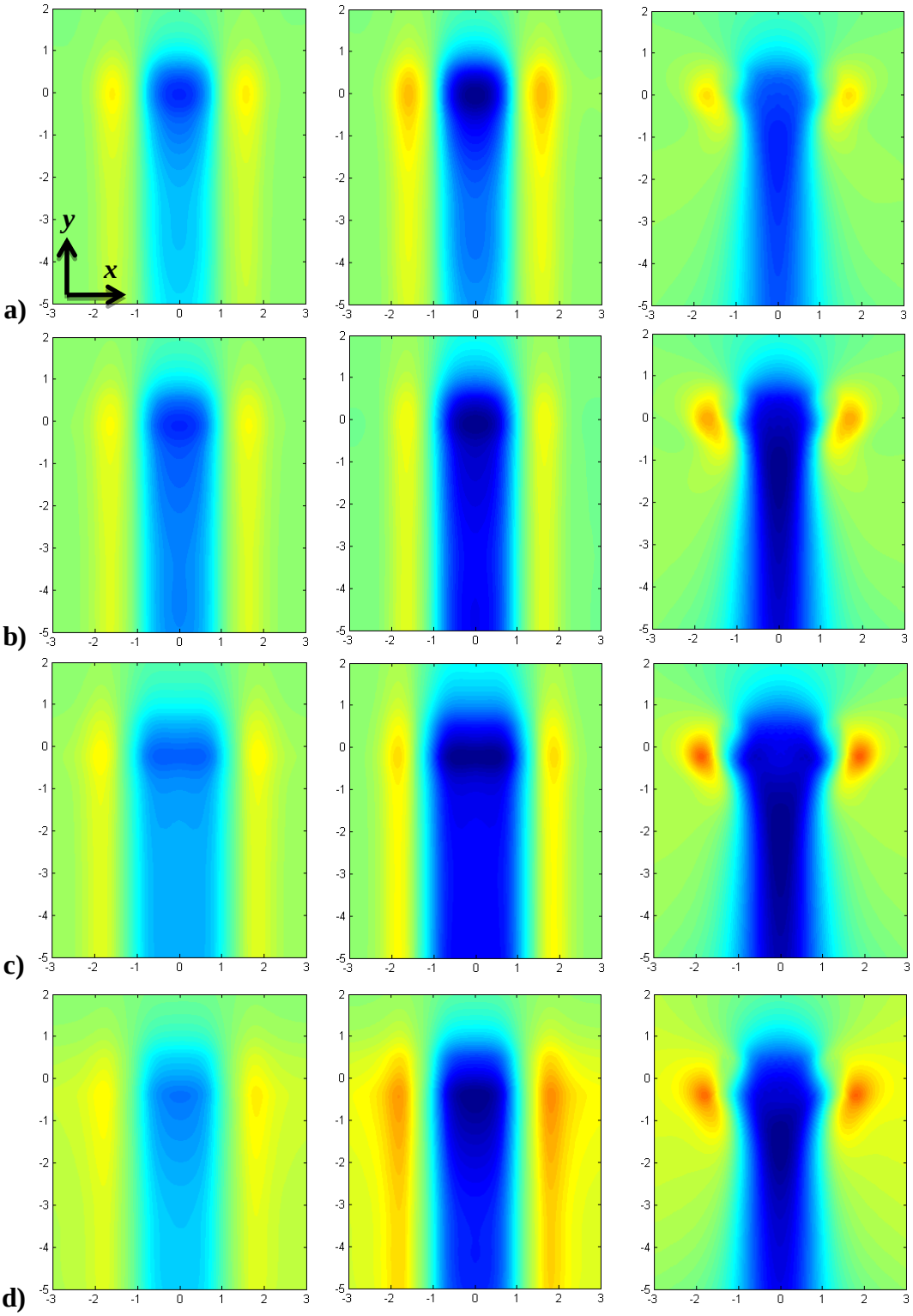


**Figure 4.23: Steady state cycle-averaged vertical velocity contour (-1,1) SVD mode 1 (left), modes 1-10 (center), and period average (right) on (-3,3)×(-5,2) domain for A10 and frequency ratios: a) 1/2, b) 1/3, c) 1/4, and d) 1/6.**

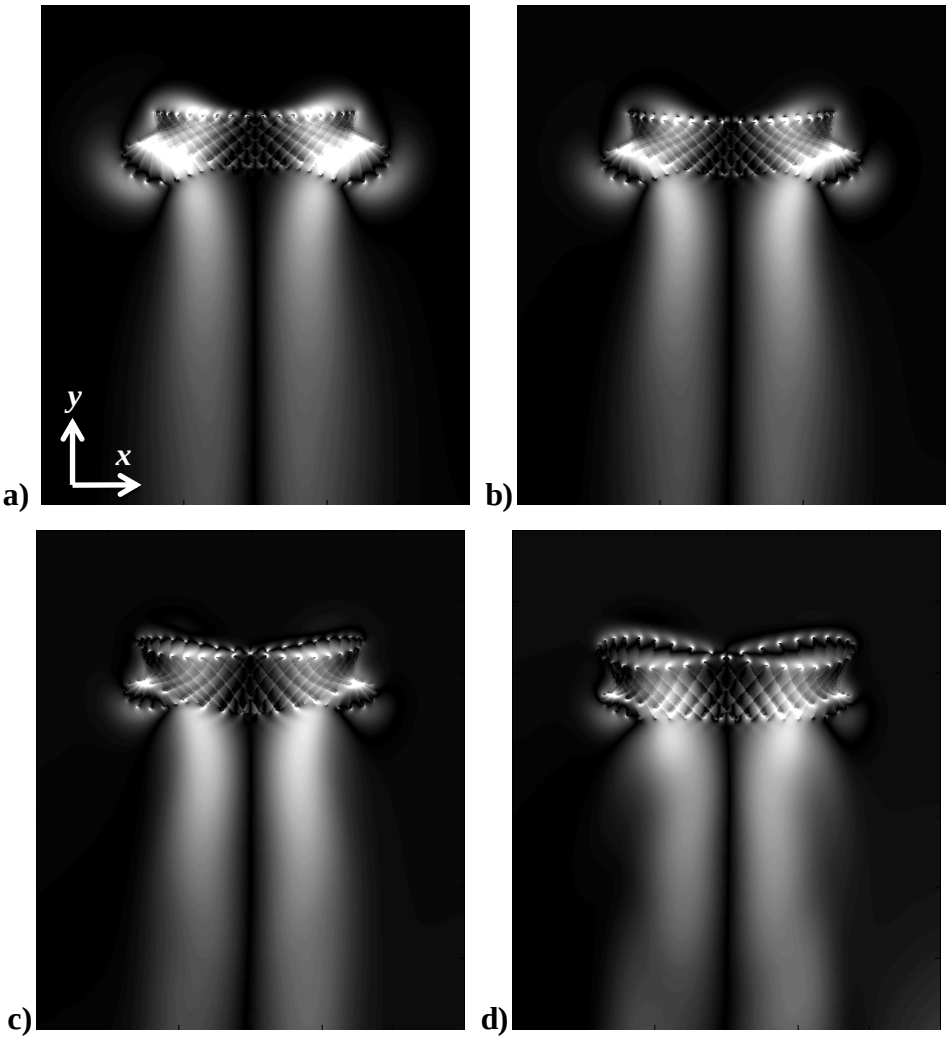


**Figure 4.24: Steady state cycle-averaged vorticity magnitude contour (0,1) on (-3,3)×(-5,2) domain for W4 and link lengths: a) A10, b) A25, c) A50, and d) A75. Amplitudes are normalized by maximum magnitude component value; 40 Snapshots per period.**

For the cases presented pictorially in Figure 4.24, the same analysis was applied to all cases with the forcing frequency ratios 1/2 and 1/3. Supplementary figures for these frequency ratios are included in Appendix A for comparison. With total magnitude circulation, denoted "|circulation|," as defined above, the values computed for each frequency and leading link length case are presented in Figures 4.25 and 4.26. The plots of total magnitude circulation exhibit curiously coherent trends for both frequency ratios

and normalized leading link lengths. One observes common trends in circulation as a function of the normalized leading link length: wings with symmetrical links or slightly smaller normalized leading links tend to produce less circulation whereas wings with very small or very large free segments tend to produce more circulation. Additionally, the amount of magnitude circulation produced correlates in all cases to the frequency ratio. Higher frequency ratios (below 1) result in more circulation produced during each flapping cycle for otherwise fixed structural and fluid conditions. Flapping closer to the natural frequency results in larger angular displacements of the free link which confirms the intuitive expectation that more circulation is produced for larger amplitude angular displacements.

A rough correlation is observed for the lift-to-power and lift-to-drag efficiency ratios and total magnitude circulation in the truncated domain for the high performance frequency ratios $\omega_f / \omega_n$ = 1/3 and 1/4 for various leading wing section lengths. A brief comparison of the performance is presented in Figure 4.27.

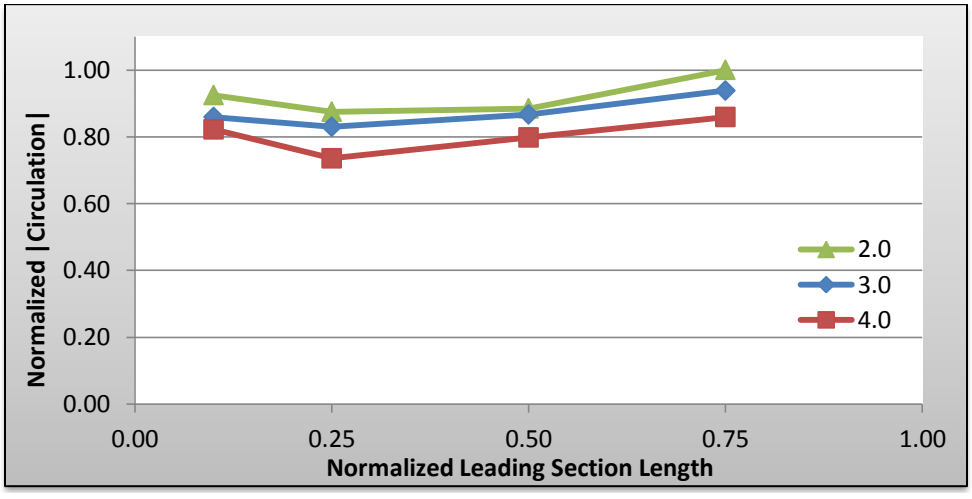


**Figure 4.25: Steady state cycle-averaged total magnitude circulation on (-3,3)×(-5,2) domain for different frequency ratios and leading link lengths.**

It is pointed out that the peak configurations for the frequency ratio $\omega_f / \omega_n$ = 1/3 correspond to a minimum in the circulation produced. Likewise, a similar trend is observed for the frequency ratio of $\omega_f / \omega_n$ = 1/4, that generally higher circulation production results in lower lift-to- power and drag efficiency measures. The trend begins to break down for the frequency ratio $\omega_f / \omega_n$ = 1/2, for which the system was found to exhibit relatively poor performance and likely has significant additional factors altering the performance metrics with regard to circulation. The trend is moderately strong for $\omega_f / \omega_n$ = 1/3 in the lift coefficient and the lift-to-power ratio such that a near-linear relationship is found, as shown in Figure 4.28.

It is emphasized that the moderately strong relationship depicted in Figure 4.28 is only found for the frequency ratio 1/3, which also happens to be the frequency ratio that generates the highest lift. Despite showing a general trend of better performance for lower circulation for a frequency ratio of 1/4 as well, a linear relationship could not be drawn. The $R^2$ correlation factor for a linear relationship for the frequency ratio 1/4 for lift and lift-to-power ratios were 0.54 and 0.43, respectively; far too low to suggest that circulation production can be used to predict performance and only allowing recognition of a "general" trend. Across all frequency ratios, it is clear that circulation alone is not enough to predict performance among similar cases and that additional flow field data such as fluid jet strength must be considered.

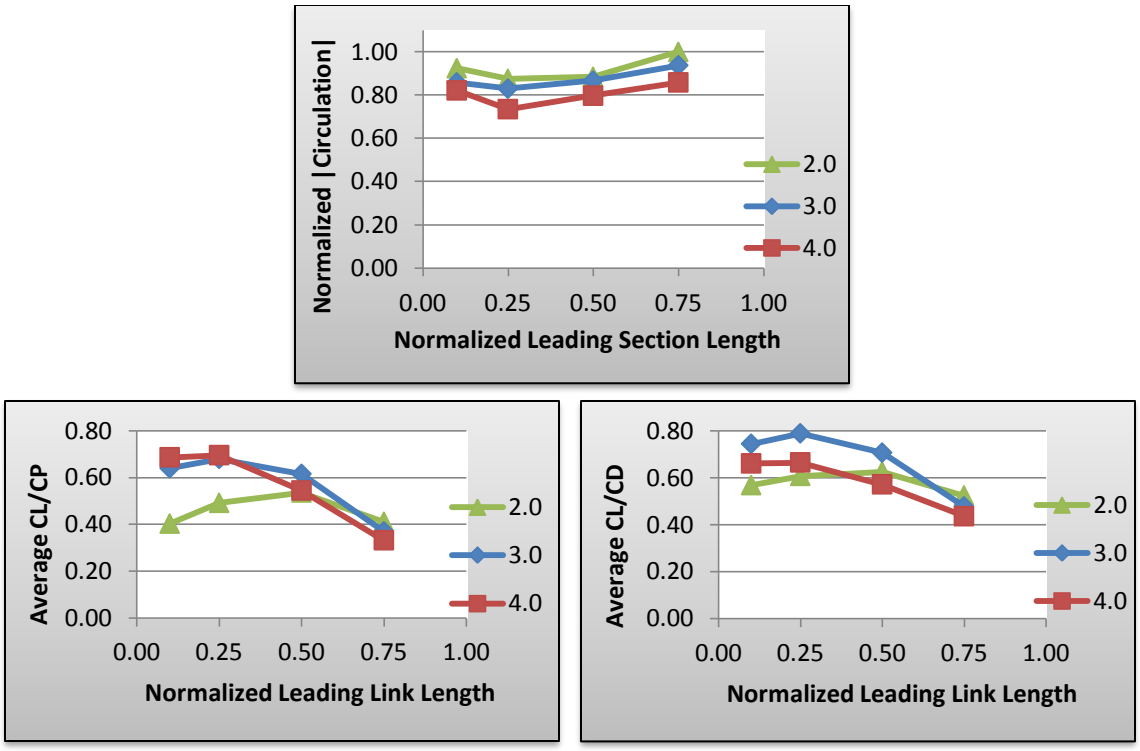


**Figure 4.27: Comparisons of steady state cycle-averaged magnitude circulation with lift-to- power and drag performance.**

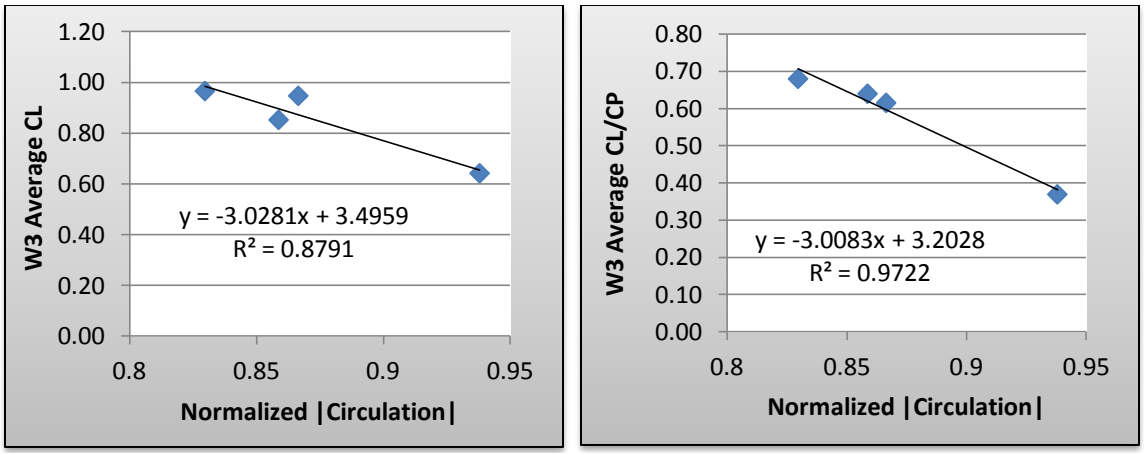


**Figure 4.28: Steady state cycle-averaged lift (left) and lift-to-power (right) for frequency ratio $\omega_f / \omega_n = 1/3$ as a function of normalized circulation on the truncated domain (-3,3)×(-5,2) with linear regression lines.**

## 4.4. Phase Shift in Angle of Attack

It would be naïve to assume that the peak lift, lift-to-drag or lift-to-power efficiency points for harmonic kinematics occur for a zero phase shift in the angle of attack, $\theta$. Furthermore, for harmonic kinematics, the peak lift, lift-to-drag and lift-to-power ratios may not occur at the same phase shift. Therefore, a case study series was chosen to evaluate the parameter combination of W3A25 for phase shifts in the angle of attack of -0.50, -0.25, 0, +0.25, +0.50, +0.75 and +1.00 radians. A pictorial description of the harmonic kinematics and phase shifts is displayed in Figure 4.29. A thought experiment suggests that advancing the phase for harmonic kinematics of a rigid flapping wing by a slight amount may reduce the drag and power expenditure by following the flow and deceleration of the trailing fluid during reversal and reducing the wing's resistance to the fluid. Considering the kinematics plots in Figure 4.29, the phase advancing cases appear that they would bias any additional rotation effort into shedding vortices and moving fluid downward. Conversely, a phase lag would intuitively increase

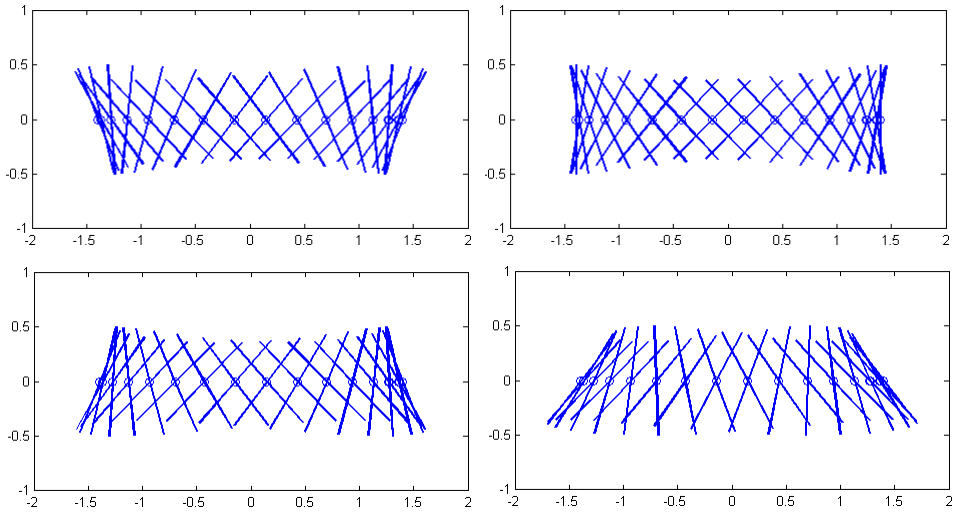

**Figure 4.29: Harmonic kinematics with phase shifts.**
**(top left to bottom right): -0.5, 0, +0.5, +1.0 radians.**
**30 snapshots per period with constant time intervals.**

the power expenditure to rotate and reverse the wing due to higher resistance to the wing's trailing fluid flow and appears that it may reduce the downward component of flow in the fluid jet. The composite $\alpha - \theta$ phase plots are displayed in Figure 4.30 for phase shifts of -0.5 through +0.5 radians.

The angular displacement amplitude is relatively unchanged for the phase shifts considered. The phase lag acts to sharpen the transition in these two-dimensional projections near the reversal points in $\theta$. Leading the phase acts to soften the transition substantially, which was also noted in Section 4.2 for reducing the power requirement to drive the kinematics. Relating performance metrics to measurable system responses such as angular displacement and trends in two-dimensional phase plot projections provides the significant advantage of distilling higher-dimensional effects of the fluid into simple real-time feedback. With this objective in mind, the lift coefficient obtained for each of the phase shifts considered is displayed in Figure 4.31 with notable performance implications introduced due to the phase shifts.

Confirming the general predictions developed with thought experiments and rigid wing kinematics plots, the lift coefficient data in Figure 4.31 demonstrates an enhancement in lift generation for leading the phase by up to approximately +0.5 radians. This phase shift results in approximately a 4% increase in lift production for steady flapping flight. A phase shift of +0.5 radians (28.6°) appears to be most advantageous for the flapping model and conditions presented. The lift improvement trend is curiously almost linear between -0.5 and +0.5 radians with a slope of 0.15 $rad^{-1}$ within the range.

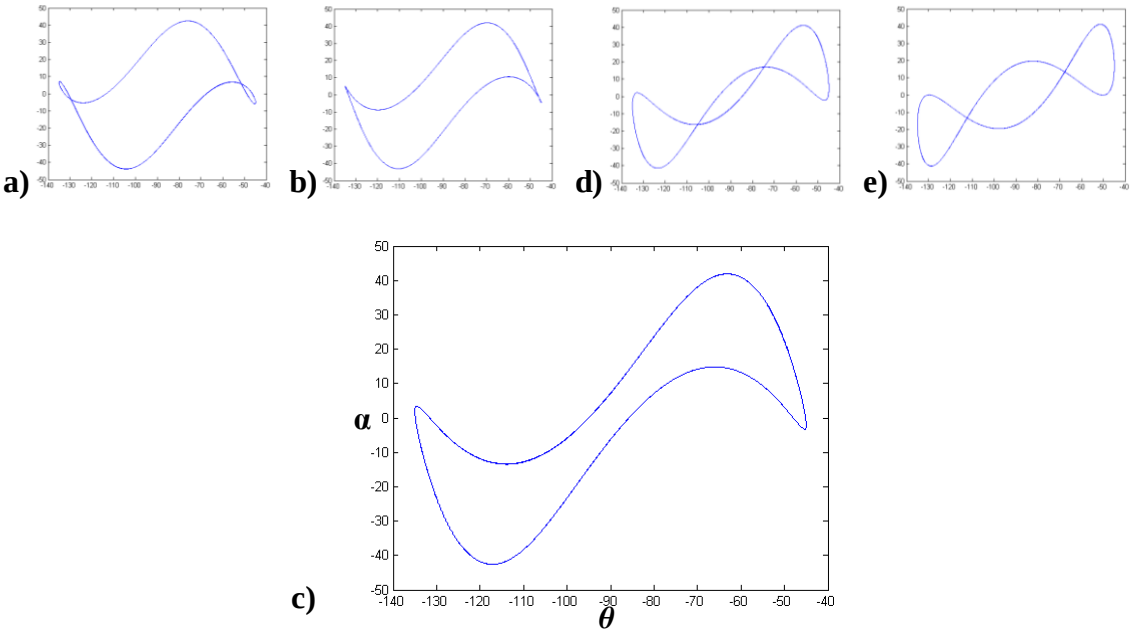


**Figure 4.30: Steady state response plots in the $\alpha - \theta$ plane for phase shifts a) -0.50, b) -0.25, c) 0, d) +0.25, and e) +0.5 radians.**

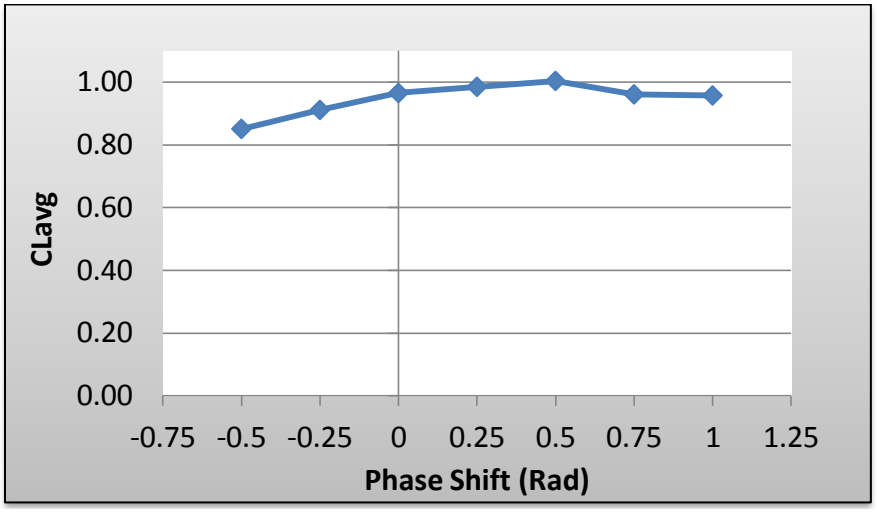


**Figure 4.31: Steady state lift coefficient plot for phase shifts (-0.50, +1.00) radians.**

For implementation purposes, this can be interpreted as a benefit in both the context of improving performance with simple kinematics modifications and the low sensitivity to

deviations from targeted values. If for a flapping insect or MAV under these conditions, one can only practically implement and control a kinematics phase shift to within ±0.25 rad (14.3°) of the intended value of +0.25rad, a lift coefficient between 0.97 and 1.0 can still be reliably achieved.

Plots of the efficiencies of lift with respect to drag and power are presented in Figure 4.32 for the various phase shifts considered. Note that the lift-to-drag curve displays an efficiency peak for a zero phase shift, though it also increases again for higher phase shifts. Since the practical metric for implementation and design is consideration of power, attention is shifted to the lift-to-power ratio. Following the trend in the lift coefficient, the lift-to-power efficiency displays an increasing trend for phase shifts between -0.5 to +0.5 radians. Phase lags appear to require more power while producing less lift than the zero offset case whereas phase leads up to +0.5 radians appear to increase lift while slightly reducing power requirements during stroke reversal.

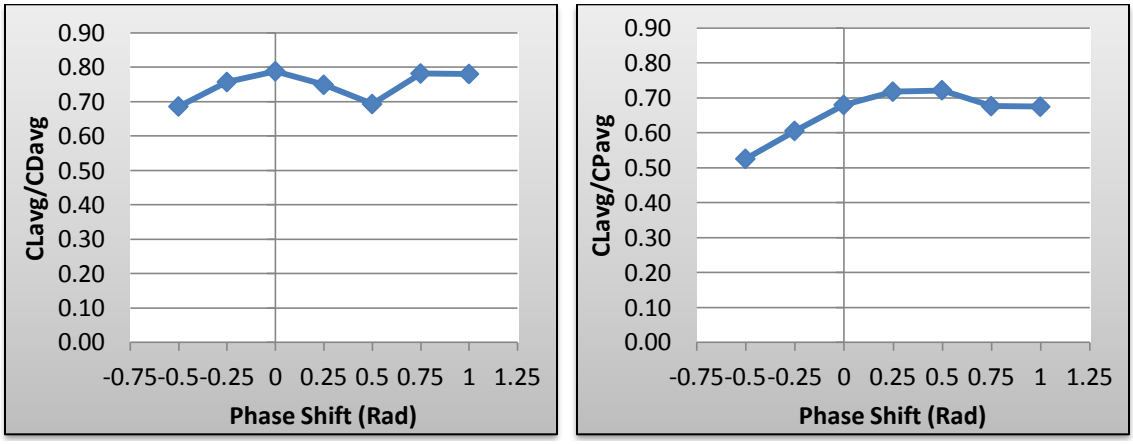


**Figure 4.32: Plots of steady state ratios for lift-to-drag (left) and lift-to-power (right). Phase Shifts (-0.50, +1.00) radians.**

Beyond a phase lead of +0.5 radians, the wing section begins to lead the fluid rather than moving with it with least resistance, and the steep angle of attack during peak translation speeds reduces the lift generated. The peak lift and peak lift-to-power efficiency point occur for a phase lift of approximately +0.5 radians, corresponding to a 4% increase in lift production and a 6% increase in lift-to-power efficiency. It is notable that the case of W3A25 with a phase shift of +0.5 radians is the only case in all of the parameter combinations considered in the present work to achieve or exceed a lift coefficient of 1.0, and the phase shifts of +0.25 and +0.5 radians are the only cases to surpass a lift-to-power ratio of 0.7.

## 4.5. Transition to Forward Flight

The various harmonic kinematics used in the present work to this point have been strictly for symmetrical, steady hovering. It is proposed that a mechanism for transition between symmetric hovering and forward flight is the breaking of symmetry in harmonic kinematics to produce an unbalanced lateral force while maintaining the majority of the dominant vertical lift force. The breaking of symmetry is implemented by an offset in the angle of attack while maintaining the same amplitude. A pictorial representation of the kinematics for various angle of attack offsets is presented in Figure 4.33 and the modified theta kinematics are presented in equation 4.2 where a subscript *T* represents the transition.

$$\begin{cases} t < t_T & \theta(t) = \theta_0 + \left(1 - e^{-t/\tau}\right) A_\theta \sin\left(\omega_f t + \gamma\right) \\ t \geq t_T & \theta(t) = \theta_0 + \theta_T \left(1 - e^{-t/\tau_T}\right) + \left(1 - e^{-t/\tau}\right) A_\theta \sin\left(\omega_f t + \gamma\right) \end{cases} \tag{4.2}$$

The greater the offset, the greater the period-averaged net lateral force is expected to be and the lower the vertical lift is expected to be. For the case of +45° offset, the kinematics in Figure 4.33 shows that a purely horizontal force is expected with zero net lift for period-averaged forces. Angle of attack offsets of 0°, 5°, 10°, 20°, and 30° are selected to simulate and characterize the effects of asymmetrical flapping. As with previous hovering cases, the wing decays from rest to steady, symmetric hovering between the periods 0 and 5. For periods 8 and 10, the structural and fluid responses are compared with baseline control cases to validate steady hovering. Over periods 10 through 12, there is a decay from steady hovering to the offset kinematics displayed in Figure 4.33. Over the periods 13 and 14, the fluid is allowed to reach a steady state and the data are presented from periods 15 and 16. Simulations are conducted in this manner

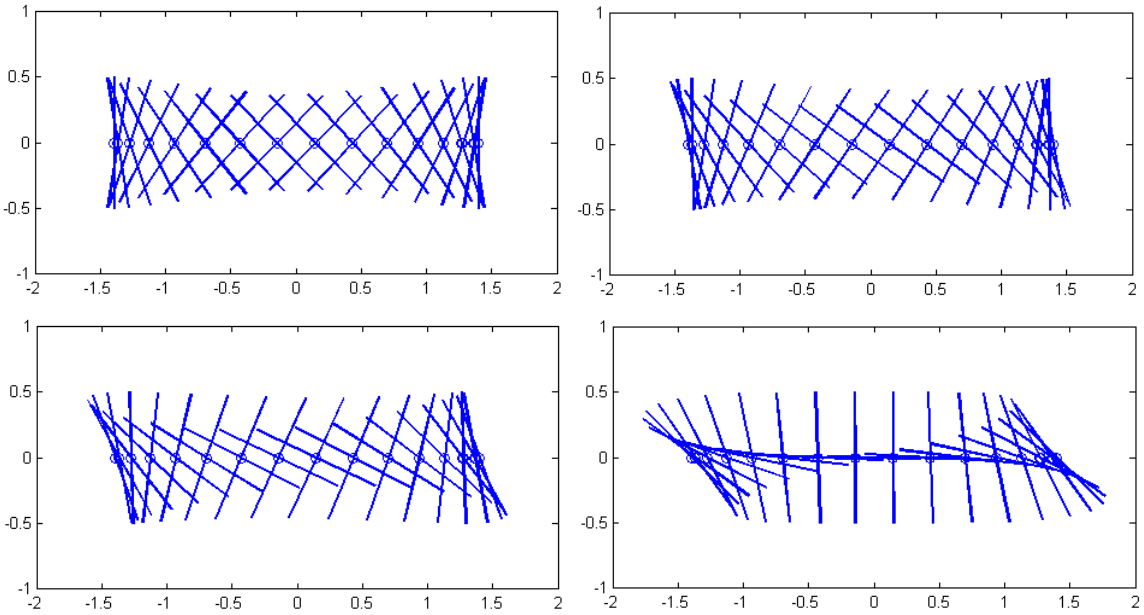

**Figure 4.33: Steady state rigid wing harmonic kinematics with angle of attack offset (top left to bottom right): 0°, +10°, +20°, and +45°. 30 snapshots per period with constant time intervals.**

for symmetric flexible wings with frequency ratios of 1/2, 1/3, and 1/4. It is critical to note that this "transitional flight" model is not intended to model full transition from steady hovering to steady forward flight. The zero location of the wing kinematics remains in the same position, equivalent to an entirely stationary body. In reality, once the flapping system begins moving through the fluid due to the lateral force, the accuracy of this model devolves. Therefore, the results presented in this section simply provide an approximation to the forces produced quickly after the kinematics transition.

The lift coefficient is given in Figure 4.34 for all of the cases simulated. The forcing frequency ratio case of 1/3 is again found to be the highest performance lift case for symmetrical wing geometry, and this case appears to be moderately sensitive to deviations from a zero offset. For the low-performance frequency ratios of 1/2 and 1/4, the system response displays minimal sensitivity to offsets between zero and up to nearly 10°, suggesting that any lateral benefit at either of these frequency ratios within this range can be achieved without impacting the available lift production. However, for all cases,

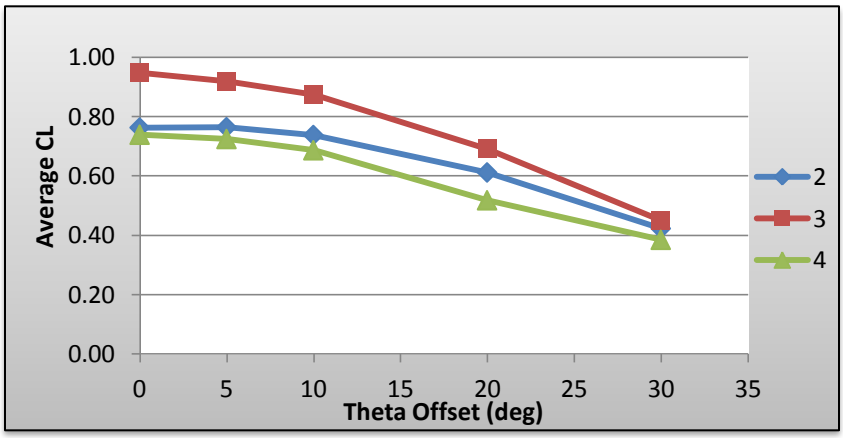


**Figure 4.34: Steady state lift coefficient for different angle of attack offsets and inverse frequency ratios W2, W3, and W4.**

large enough offsets in the angle of attack cause a consistent downward slope indicating the tradeoff between vertical and lateral thrust productions.

A more useful metric may be the total thrust produced, given that a simple reorientation of the flapping system's base can redirect the thrust in any desired direction. For comparison with the lift production, the lateral thrust produced as a function of angular offset is presented in Figure 4.35 on the left along with the total thrust produced, presented on the right. The total thrust is simply defined as the square root of the sum of the squares of the vertical ($C_L$) and horizontal ($C_{Tx}$) non-dimensional component forces.

The horizontal thrust produced by introducing an offset into the angle of attack kinematics varies approximately linearly for the first twenty degrees with a slope determined by the frequency ratio. While a frequency ratio of 1/3 produces the highest lift, it also produces the strongest lateral force per degree offset. The curves in the right plot of Figure 4.35 put the tradeoff between vertical and horizontal thrust into perspective by considering the total thrust produced per degree offset. It is observed that the highest performance case is also the most sensitive to the introduction of an offset, losing 4.4% of the total thrust capability at 10° in order to produce a 0.24 lateral force coefficient ($C_{Tx}$) while maintaining a 0.87 lift coefficient ($C_L$), nearly, an 8% reduction in lift production. The insensitivity of lift and total thrust to angle of attack offset for frequency ratios 1/2 and 1/4 can be attributed to their poor performance at zero offset compared to the potential demonstrated by the system at the forcing frequency ratio 1/3.

The lift and horizontal thrust power efficiency metrics are plotted in Figure 4.36. The lift-to-power ratio falls from its peak value steeply, especially, for the forcing frequency ratio 1/3. For 1/2 and 1/4 ratios, the moderately flat, shallow slope is

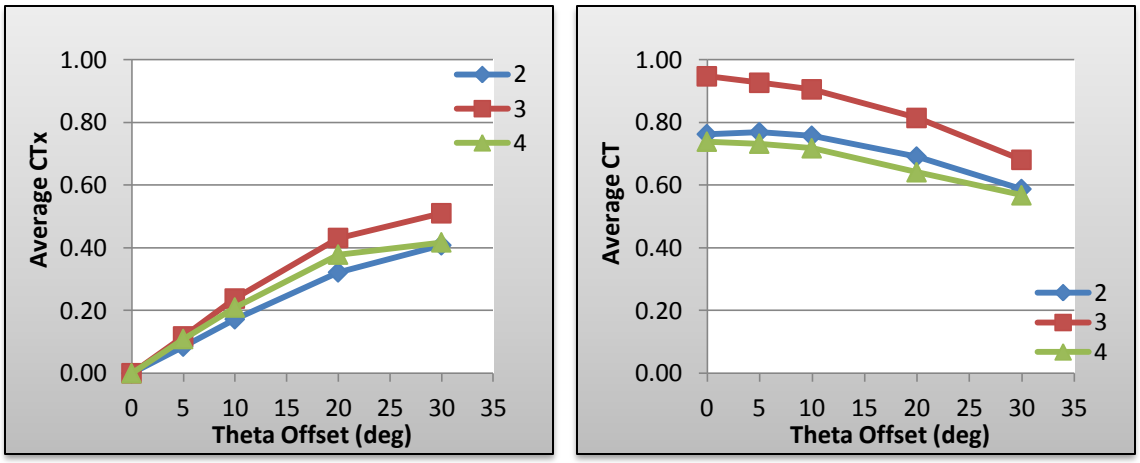


**Figure 4.35: Steady state horizontal thrust coefficient (left) and total thrust coefficient (right) for different angle of attack offsets and inverse frequency ratios W2, W3, and W4.**

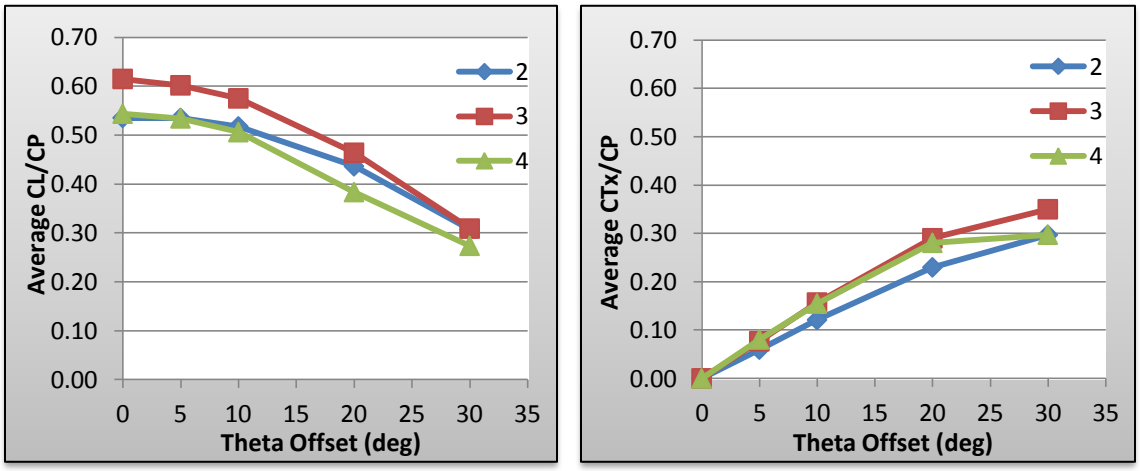


**Figure 4.36: Steady state lift-to-power coefficient (left) and horizontal-thrust-to-power coefficient (right) for different angle of attack offsets and inverse frequency ratios W2, W3, and W4.**

maintained for the first ten degrees as observed in the $C_L$ plot, falling steeply for higher offsets. The $C_{Tx}$-power-ratio plot displays similar efficiencies and slopes for frequency ratios 1/3 and 1/4, meaning that the higher horizontal thrust production for a frequency ratio of 1/3 requires a correspondingly higher power requirement such that the power

efficiency ratios are nearly identical up to a 20° offset. The vertical lift-to-power efficiency, however, reaffirms the preference of the frequency ratio of 1/3 for peak performance.

The total thrust-to-power ratio as a function of angle of attack offset is presented in Figure 4.37. The optimal efficiency is achieved for a zero offset for frequency ratios 1/3 and 1/4 whereas the optimal efficiency for frequency ratio 1/2 occurs for an offset of 5°. For the frequency ratio 1/3, the system significantly outperforms the other cases considered, and the total efficiency drop is only 3% over the first 10° offset from zero. The lift-to-power coefficient drops off fairly quickly, but the horizontal-thrust-to-power coefficient also increases quickly enough to maintain the total thrust-to-power coefficient near its maximum for offsets up to 10°. It is noted that the thrust-to-power efficiency is a description of power required to produce a particular thrust under particular conditions and parameter combinations.

A period-averaged nonzero pitching moment is also produced by the asymmetrical kinematics, presented in Figure 4.38. The free section displacement complicates the relationship between the moment produced and the angle of attack offset, however a general trend of increasing magnitude pitching moment is observed for increasing offsets in the angle of attack. Higher effective stiffness results in stronger magnitude moments produced, indicating that more control and counter-balance consideration is necessary for lower frequency ratios. In biological and MAV systems, this counter-balance may be achieved by shifting the body's center of gravity through movement of body structures such as a controllable tail or hind section. Proper displacement of the center of gravity may be used to create an equal and opposite

moment in order to maintain the desired orientation of the entire system. It is finally noted that the asymmetric kinematics for this parametric study induces a moment in all cases that acts to pitch "upward" in the direction that the body will be compelled due to the lateral forces produced.

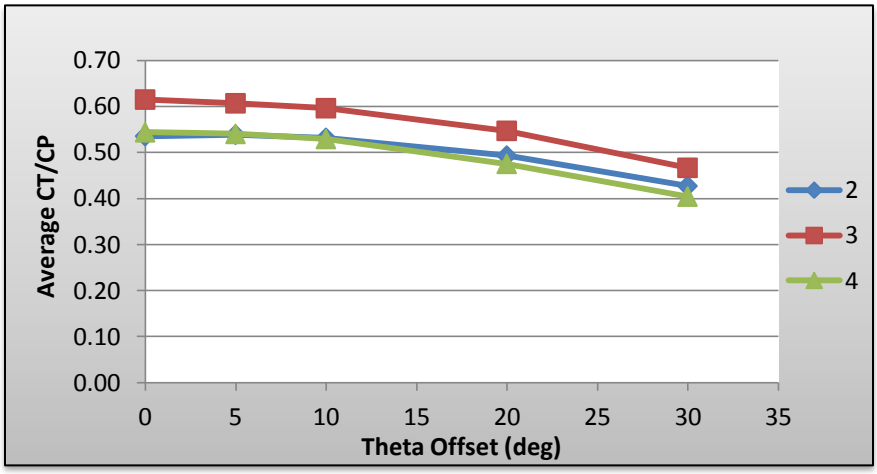


**Figure 4.37: Steady state thrust-to-power coefficient for different angle of attack offsets and inverse frequency ratios W2, W3, and W4.**

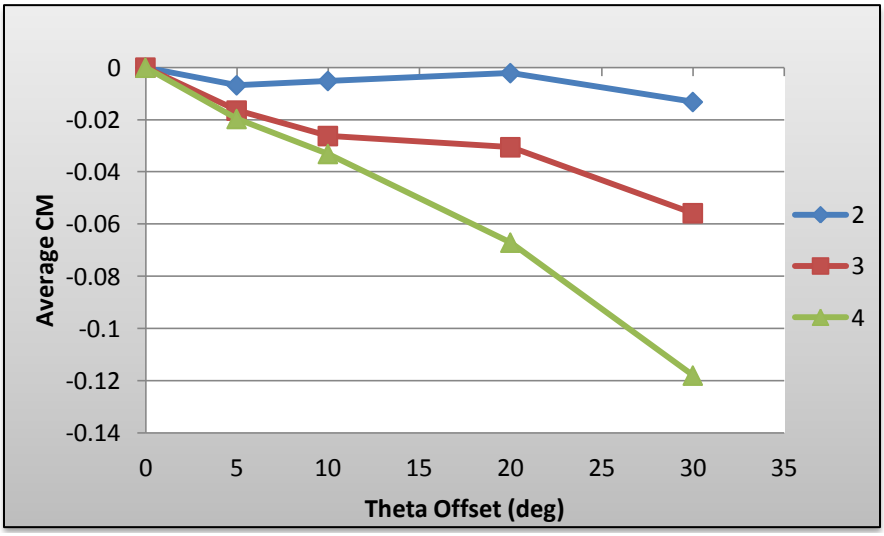


**Figure 4.38: Steady state moment coefficient for different angle of attack offsets and inverse frequency ratios W2, W3, and W4.**

It is worth noting that the offset as a mechanism to produce lateral thrust is simply a curious option for implementation with minimal system complication. For the cases considered, introducing an offset into the angle of attack generally reduces both the lift and the total thrust produced, as seen in Figure 4.34 and 4.35, especially for the high-performance 1/3 frequency ratio case and with the exception of a peak in total thrust at 5° for the forcing frequency ratio of 1/2. Another option for implementation would be to simply rotate the body during hovering such that the *x*-axis is rotated by an angular offset, turning the former "lift" force into corresponding vertical and horizontal components. The same deconstruction for that scenario can be performed as for the mechanism proposed in this section, with the same limited duration of validity due to the assumption of a stationary body; the forces computed with this simulation would only be approximately valid for a short time, during the beginning of transition between steady hovering and forward flight. The total thrust produced and the thrust-to-power ratios for evaluating this alternate mechanism can be interpreted simply as the lift coefficient plots and lift-to-power coefficient plots discussed in Section 4.2.

Practically, in terms of performance, the mechanism proposed in this section is less desirable than simply rotating the body, and therefore, the *x*-axis of the flapping kinematics because it results in production of lower forces and lower power efficiency. However, the actual implementation and control may be easier for MAVs given that the angle of attack is already controllable in the given kinematics whereas axis rotation requires additional actuation and control of the body. For MAVs, the omission of this extra actuation and control requirement allows for lighter systems, lower lift production requirements, and longer flight durations for a fixed power source. For insects and birds,

however, the many degrees of freedom already present in the body allow for control of the flapping axis by rotation of the abdomen or tail outward-from or under the body's center of mass. This mechanism of hovering stabilization or transition to forward or backward directional control is commonly seen in dragonflies, bees, and hummingbirds.

## 5. Summary and Concluding Remarks

A simulation-based parametric investigation of flapping flight has been presented to explore and characterize the effects of various physical parameters and kinematics for flexible wing sections during steady hovering and the beginning of transition to forward flight. The parametric studies have been organized around the following categories: i) structural dissipation at linear system resonance during steady hovering, ii) geometrical asymmetry in flexible wings during steady hovering, iii) phase shift in the angle of attack for harmonic kinematics during steady hovering, and iv) the initial transition from steady hovering to forward flight by the smooth introduction of a constant offset in the angle of attack for symmetrical, flexible wings.

Performance metrics used to compare the results obtained from the different case studies and evaluate the effects of parameters of interest consist of dimensionless steady-state cycle-averaged lift, drag, power, and their ratios. With structural dissipation for flapping at linear system resonance, the system performance was found to at best only approach the lift and lift-to-power performance of a rigid wing. Furthermore, with damping during resonance forcing, positive lift forces were only produced for cases of relatively high damping factors, above approximately 1.1; that is, overdamped cases. Therefore, for flapping flight under conditions similar to those simulated in the present work, accurately modeled in two dimensions, it is highly unlikely for biological systems to employ flapping at linear system resonance due to the relatively poor lift and lift-to-power efficiency performance and the relatively large structural damping factors required. It is found to be more advantageous in terms of stated performance metrics to flap a purely rigid wing or to flap well below resonance. The few representative cases of

flapping with damping below resonance resulted in a reduction in lift, power, and the lift-to-power ratio with increasing damping; the best performance for the cases below resonance considered proved to be zero damping. The present work reaffirmed the findings of earlier work (Fitzgerald *et al*., 2011; Fitzgerald *et al*., 2012) that the peak lift and the peak lift-to-power ratio is achieved for a forcing frequency ratio of 1/3 for symmetrical wings and simple harmonic kinematics. However, it was discovered that the highest lift coefficient is achieved for a frequency ratio of 1/3 and an asymmetrical wing with a normalized leading link length of $0.25L_C$ (case W3A25). Furthermore, the highest lift-to-power ratio is achieved for a frequency ratio of 1/4 and a normalized leading link length of $0.25L_C$ (case W4A25). For highly compliant ($\omega_f / \omega_n =$ 1/2) and highly stiff ($\omega_f / \omega_n =$ 1/6) wing sections of the considered geometries, the system performed poorly compared to the mid-stiffness frequency ratios for which the system performance exhibited peak lift and peak lift-to-power ratios. For mid-stiffness frequency ratios ($\omega_f / \omega_n =$ 1/3 and 1/4), moderately shorter leading sections and longer relative free sections of the flexible wing section generally produced more favorable lift values and power efficiency, especially in the overall high performance cases.

Phase plot projections of the responses for the asymmetrical, flexible cases show a general correlation between the softness of transitions in the two-dimensional projections of the plotted variables and general improvement of performance. The frequency characterization is explored further with the use of Fast Fourier Transforms of the $\alpha$ and $\dot{\alpha}$ steady state responses. Significant spectral content is found for odd harmonics while even harmonics are not noticeable above the background noise levels.

The significant spectral content dies off above background levels above a dimensionless frequency of approximately 5. Furthermore, a specific profile of relative magnitude content in the FFT plots curiously appears for the high-performance parameter cases (W3A25, W4A10 and W4A25), which is significantly different than the FFT content of other low-performance cases. It is proposed that a control system employing excitation and damping of the free link in a flexible wing may be used to enhance performance of the low-performance cases by matching the common FFT content of the high-performance cases. Flow structures in the near-body flow field are identified as the leading and trailing edge vortices, the end of stroke vortex, the vertical vortex street, and the central vertical fluid jet. The central vertical fluid jet is identified as the most significant flow structure to determine lift production; however, it was found to require consideration of the energy expenditure into fluid circulation in order to predict relative performance. Circulation and vortices, while significant and beneficial in fixed-wing airfoil flow, prove detrimental to performance in some cases of hovering flapping flight due to the inefficient transfer of energy into the fluid as less-useful rotational energy rather than the translational energy that creates lift through linear momentum transfer. Therefore, minimizing excess vorticity production and maximizing vertical fluid jet strength appears to produce the maximum lift and the highest lift-to-power ratio.

A phase shift in the angle of attack for simple harmonic kinematics was found to be relatively insensitive for the case study presented, but yet also found to have a significant effect on performance for large phase shifts. Lift is reduced and power required is increased for phase lagging shifts, while lift production is increased and power required is decreased for phase leading shifts. The optimal phase lead within the coarse

resolution presented was found to be around 0.5 radians, corresponding to approximately a 4% increase in lift production and a 6% increase in the lift-to-power ratio when compared to the baseline zero phase shift case (W3A25). The improvements in performance are indicative of the effects of "wake capture," whereby upon stroke reversal the wing utilizes previously expended energy in the trailing fluid to enhance lift and reduce the power required to perform the kinematics reversal. Wake capture is evidently increased between the phase shifts of -0.5 radians and +0.5 radians, yielding a nearly linear improvement in performance metrics throughout this range, after which the performance decreases due to premature advancement of the angle of attack during lateral translation.

A mechanism for transition between hovering and forward flight for symmetrical flexible wings is presented as the change from symmetric harmonic kinematics for steady hovering to asymmetric harmonic kinematics by introducing a steady offset in the angle of attack. The asymmetric kinematics produces an unbalanced lateral force while maintaining the majority of the dominant vertical lift force. The lateral force is evaluated in terms of the tradeoff between the vertical lift and the total magnitude of thrust produced by the wing as well as the forces relative to power expenditure for various asymmetrical offsets. For the best performance frequency ratio case, $\omega_f / \omega_n = 1/3$, the system is found to produce the highest total thrust coefficient and highest total-thrust-to-power coefficient ratio for zero angle of attack offset, while being moderately sensitive to offsets from zero. In all cases, the lift production is successfully traded for lateral thrust production by increasing the offset in the angle of attack at the expense of a loss in total thrust production and thrust-to-power efficiency except for small offsets between 0 and

5° for $\omega_f / \omega_n = 1/2$ and 1/4, for which there is a slight efficiency gain for those particular cases. The best performance frequency ratio case, $\omega_f / \omega_n = 1/3$, is found to be the most sensitive to the introduction of an offset, losing 4.4% of the total thrust capability at a 10° angle of attack offset in order to produce a 0.24 lateral force coefficient ($C_{Tx}$) while maintaining a 0.87 lift coefficient ($C_L$); nearly, an 8% reduction in lift to produce a horizontal thrust just over one quarter the magnitude of the lift. A pitching moment is also produced for the asymmetrical kinematics that generally increases with the angle of attack offset and acts to pitch "upward" in the direction that the system is compelled by the horizontal thrust produced.

The general results of this study allow for prediction of approximate wing properties and parameters as well as kinematics for flapping insects that operate near Reynolds number 75 with approximately two-dimensional flows. For example, the parametric investigations in the present work suggest that it is highly unlikely for an insect operating near these simulated conditions to flap at linear system resonance due to the low performance. Considering the preference of evolutionary development towards low energy expenditure and high thrust capability for swift movement, it is predicted that insects under conditions similar to those simulated prefer to flap at 1/4 to 1/3 of their wing's natural frequency with wing geometry configured with a shorter, driven leading edge (~$0.25L_C$) with a longer trailing section free to deform flexibly with inertial and fluid forces. For MAVs on such a small Reynolds scale, the design recommendations are similar: design wings with larger free sections and shorter driven sections (~$0.1\text{-}0.25L_C$) at the leading edge; size the wingspan, body mass, and payload mass, select the structural stiffness, and implement control to flap between 1/4 and 1/3 of the wing's natural

frequency with a 0.5 radian phase lead in the angle of attack. These conditions suggest high relative lift production and an efficient lift-to-power ratio for harmonic kinematics, translating to maximum acceleration and payload capability as well as flight duration for a fixed on-board energy supply.

## 5.1. Ongoing Work and Suggestions for Future Work

Ongoing work includes generation of intensity maps of vertical velocity similar to those presented for vorticity in Section 4.2.3. The goal is to quantify the strength of the fluid jet in the truncated domain and relate the mean magnitude vorticity and mean vertical velocity flow with the lift generated. It is proposed that lower circulation corresponds to higher power efficiency for similar fluid jet strengths. The findings in Section 4.2.3 suggest that circulation has a negative effect on the efficiency of converting energy transferred into the fluid into useful lift production. However, the lack of applicability of the finding across all forcing frequency ratios, particularly the low-performance cases, and the lack of clear relationships between vorticity production and lift production suggests that more variables must be considered. Additional characterization of the effects of structural dissipation for forcing below linear system resonance is desired, motivating a series of case studies for various damping factors. Frequency content and flow structures are to be correlated in a similar way as the structurally un-damped cases in the present work, and the effects of structural dissipation on the performance of flexible wings will be emphasized.

A few suggestions for future work can be broken down into major categories. First, a simple continuation of the present work in the context of further investigation of

configurations and parameter combinations that extrapolation suggests may yield high-performing results. Additionally, a series of numerical experiments may be performed to cover parameter combinations not yet fully mapped. For example, the present work investigated phase shifts only for W3A25 combination, but not other high-performing cases at zero phase shift such as W3A50, W4A10 and W4A25. It is possible that one or more of those three additional cases may yield even higher peak performance with respect to lift generation or lift-to-power efficiency. Implementing active control of the wing stiffness is recommended such that the FFT dimensionless frequency content may be dampened or excited in order to obtain the specific FFT profile found to be common among the high-performing cases. Additionally, stiffness control may be used to investigate perturbations in the current "optimal" FFT profile in order to attempt to further improve performance. Given that the common high-performing dimensionless frequency content (FFT profile) was found in combinations spanning two frequency ratios and three link lengths (W3A25, W3A50, W4A10, W4A25), manipulation of the dimensionless frequency content may allow for equally high performance under many various conditions of flapping frequency ratio and wing geometry.

Second, parameters may be investigated that are currently able to be modified in the existing computational model but have been fixed for the present work. Examples of these are the Reynolds number, the fluid-to-solid density ratio, kinematics amplitudes and other variable phase shifts or offsets, link profile thickness, and further investigation of the effects of structural dissipation. For the cases considered in the present work, a fixed body flaps two-dimensional wings in an initially-stationary fluid domain. The fluid domain may be given a prescribed inflow to simulate steady forward flight with specific

assumptions regarding the body mass being moved through the fluid, approximated as perfectly steady inflow. Additionally, the model may be modified to accommodate further physical capabilities. For example, the root of the wing kinematics may be attached to an inertial base with a specified weight with either one degree of freedom (vertical motion), two linear degrees of freedom, or two linear directions and pitching angle movement for full two-dimensional inertial coupling. While the present model includes a single degree of freedom, the wing profile may be modified for multiple flexible joints or continuous flexibility. The wing geometry may also be modified to include more aerodynamic shapes than a monolithic, symmetric wing; such as an NACA symmetric or cambered airfoil, or one that is bio-inspired. For biological systems, amplitude and frequency are typically the primary controllable variables. While natural frequency has been given significant consideration here at Reynolds 75, a study of amplitude effects in two spatial directions and orientation may provide significant insight into the structure and evolution of flapping systems found in nature. It is further acknowledged that the camber produced during flexible flapping is frequently positive in biological systems whereas the single-degree-of-freedom flexible system developed for the present work resulted in negative camber. Multiple flexible joints, continuous flexibility, either homogeneous or structured, may result in positive-camber wing deformation and allow for alternate performance-trend conclusions.

Third, a survey of flapping frequency ratio and wing geometry for insects flying under similar conditions is recommended in order to test the predictions and conclusions made by the present work. Namely, the results here predict a preferred flapping frequency ratio of approximately 1/4 to 1/3 and a preferred shorter, driven leading edge

(~$0.25L_C$) with a longer trailing section free to deform flexibly with inertial and fluid forces. This general configuration was found to produce maximum lift and maintain maximum lift-to-power efficiency in the present work.

The first note of difficulty encountered in these numerical experiments involving snapshots and flow fields is the enormous amount of data generated and computational resources required. Simulations presented in the present work produce approximately 10Gb of raw data to simply capture the steady state flow fields, and can reach around 12Gb per case with all post-processing files. Minimally useful data sets are on the order of 5Gb per case. Each of the cases at Re 75 requires approximately 2,000-2,500 CPU-hrs/GHz to solve depending on the number of periods simulated, the complexity of the structural system or the fluid domain response. The second note of difficulty is the rapidly growing number of simulations required to fully map the parameter space considering each variable of interest as a new "dimension" to map all combinations. Table 6.1 shows how quickly the scope of an investigation can get out of hand: the third column, a study only considering three frequency cases, four damping factors and three leading link lengths at two Reynolds numbers requires a total of 72 cases to be simulated, would generate 360Gb of data (at a coarse snapshot rate producing 5Gb per simulation) and would take approximately 100,000 CPU-hrs to solve and post-process.

The practical implementation of a large-scale study utilizing DNS and the evaluation methods of the present work requires full automation of the setup, starting, post-processing and summary of the full simulation process and the use of a computing cluster with a large number of available nodes to run cases in parallel. The present work was conducted on a 6-core system in batches of 4-6 simulations simultaneously with 36

**Table 5.1: Variables of Interest and Scope Implications**

| **Variables** | **# Cases** | | **# Cases** | | **# Cases** | |
|---|---|---|---|---|---|---|
| Frequency Ratio | **5** | 5 | **5** | 5 | **3** | 3 |
| Damping Factor | **5** | 25 | **4** | 20 | **4** | 12 |
| Leading Link Length | **4** | 100 | **4** | 80 | **3** | 36 |
| *x* Amplitude | **5** | 500 | **1** | 80 | **1** | 36 |
| θ Phase Shift | **5** | 2500 | **1** | 80 | **1** | 36 |
| θ Amplitude | **5** | 12500 | **1** | 80 | **1** | 36 |
| Reynolds Number | **3** | 37500 | **3** | 240 | **2** | 72 |
| | **Total # Cases** | | **Total # Cases** | | **Total # Cases** | |
| | 37,500 | | 240 | | 72 | |
| | 187,500 Gb data | | 1,200 Gb data | | 360 Gb data | |

simulations completed properly and successfully in total, generating over 400Gb of raw and post-processed summary data.

Laboratory experiments are recommended as a validation of both the physical results obtained in the present work and the evaluation of the range of validity of the two-dimensional flow assumption or approximation. Considering that turbulence is inherently a three-dimensional phenomenon and many biological flapping systems employ angular kinematics described primarily by pitch, plunge and sweep (or pitch, roll and yaw); fully three-dimensional simulations are a highly desirable extension of the present work. However, given the computational requirements for two-dimensional simulations noted above, there exists a scaling challenge in that a third dimension with the same resolution of the original lateral dimension would require the expansion of the 1229x551-node grid (677,179 total) into a 1229x551x551-node grid (373,125,629 total). The most costly operation in DNS of an incompressible fluid obeying the Navier-Stokes equation is the un-parallelizable inversion of the pressure-correction matrix. Furthermore, the simulation

of higher Reynolds number flapping flight allows for larger time steps but requires finer spatial resolution, exacerbating the difficulty of the matrix inversion and suggesting that three-dimensional DNS of flapping flight is outside the realm of current computing capability for full DNS. Still, two-dimensional simulations may be used to generate knowledge of precise effects of parameter choices and combinations as well as a thorough representation of the near-body flow field and fluid physics within the domain. The conclusions made through two-dimensional simulation may well approximate some three-dimensional configurations that can be validated with laboratory experiment. Two-dimensional simulation and three-dimensional experiment may be used in collaboration to produce meaningful design criteria and guidelines as well as to provide means for understanding flapping flight in biology that exists in many forms and on many scales in the natural world.

# A. Appendix: Supplementary Figures

This appendix complements the results presented in Chapter 4.

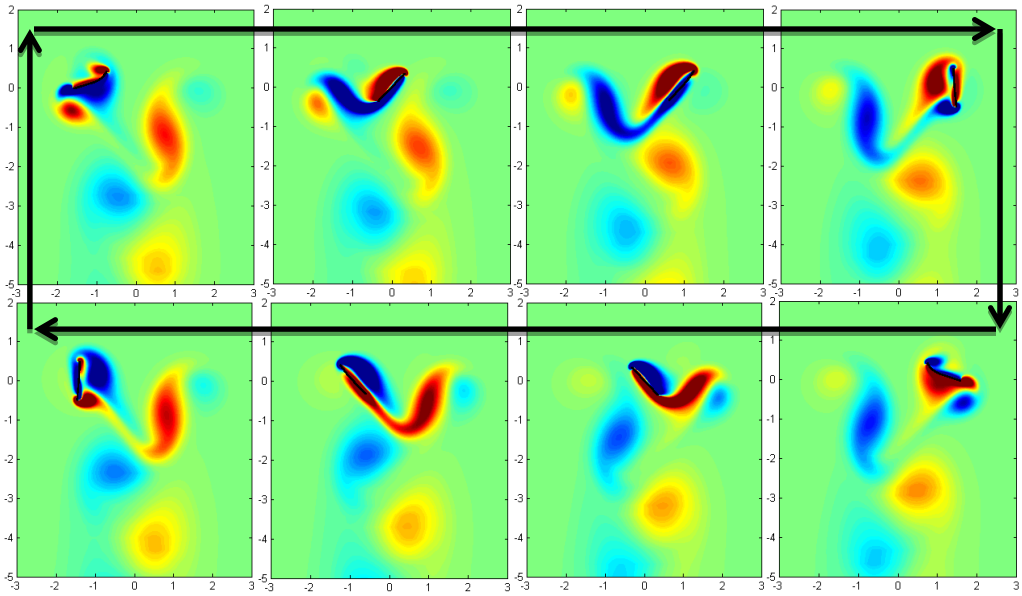

**Figure A.1: Case W3A25 vorticity contour (-3, 3) time lapse for frame interval T/8 on truncated domain (-3,3)×(-5,2) for one period.** ***Arrow indicates direction of time evolution***

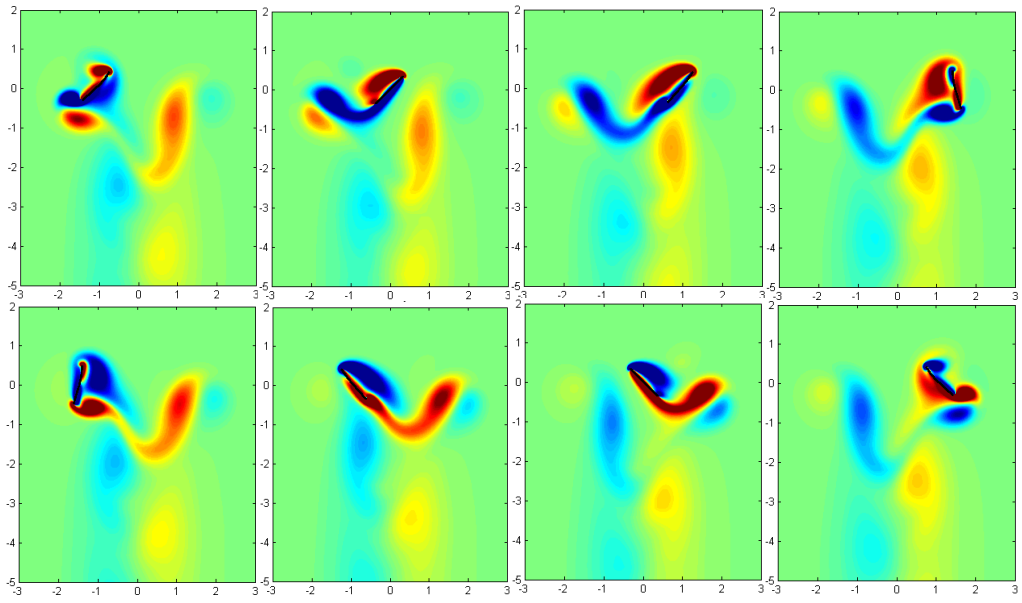

**Figure A.2: Case W4A25 vorticity contour (-3, 3) time lapse for frame interval T/8 on truncated domain (-3,3)×(-5,2) for one period.**

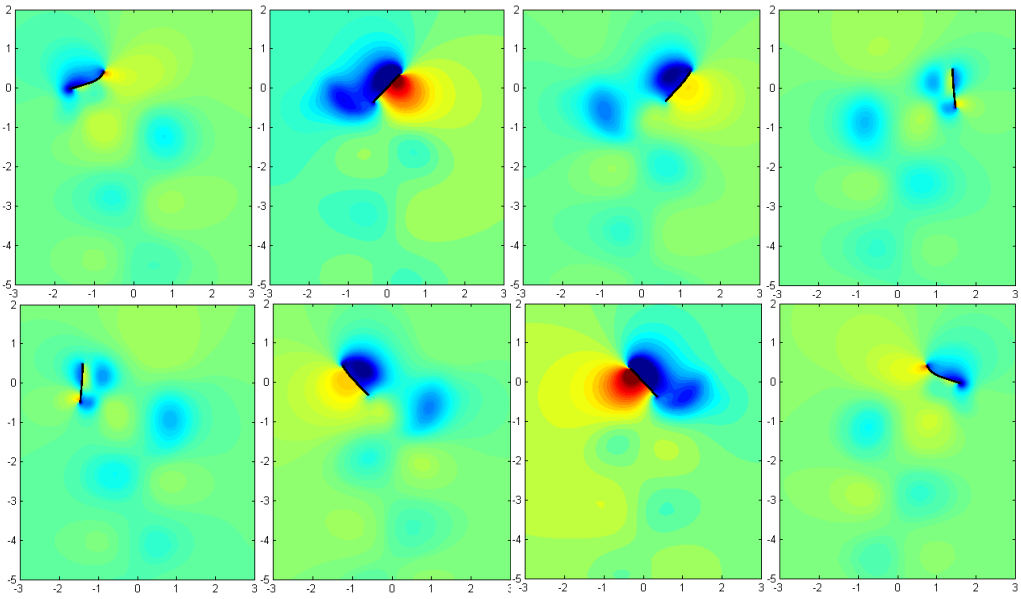

**Figure A.3: Case W3A25 pressure contour (-1, 1) time lapse for frame interval T/8 on truncated domain (-3,3)×(-5,2) for one period.**

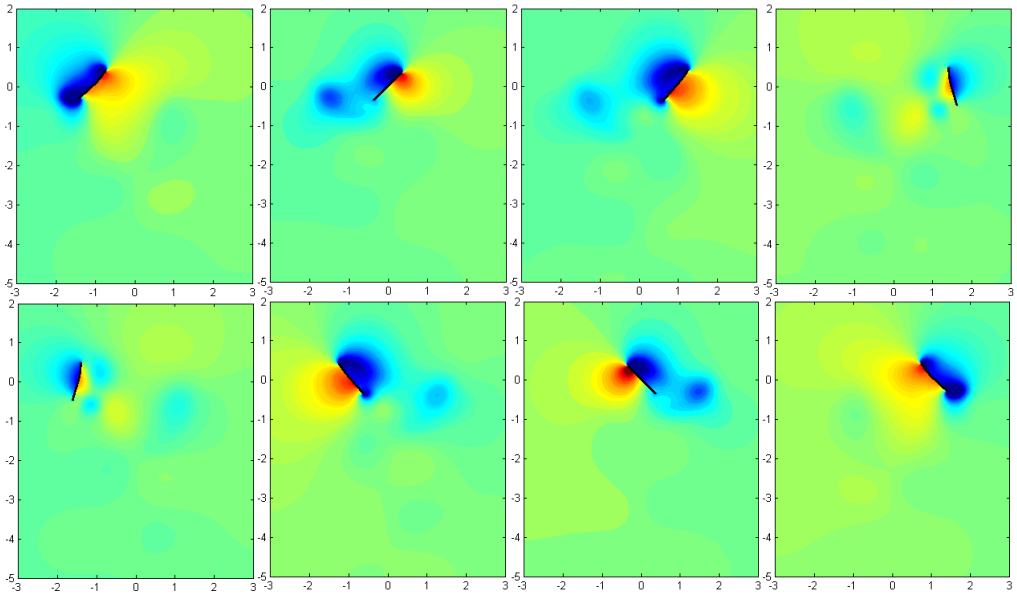

**Figure A.4: Case W4A25 pressure contour (-1, 1) time lapse for frame interval T/8 on truncated domain (-3,3)×(-5,2) for one period.**

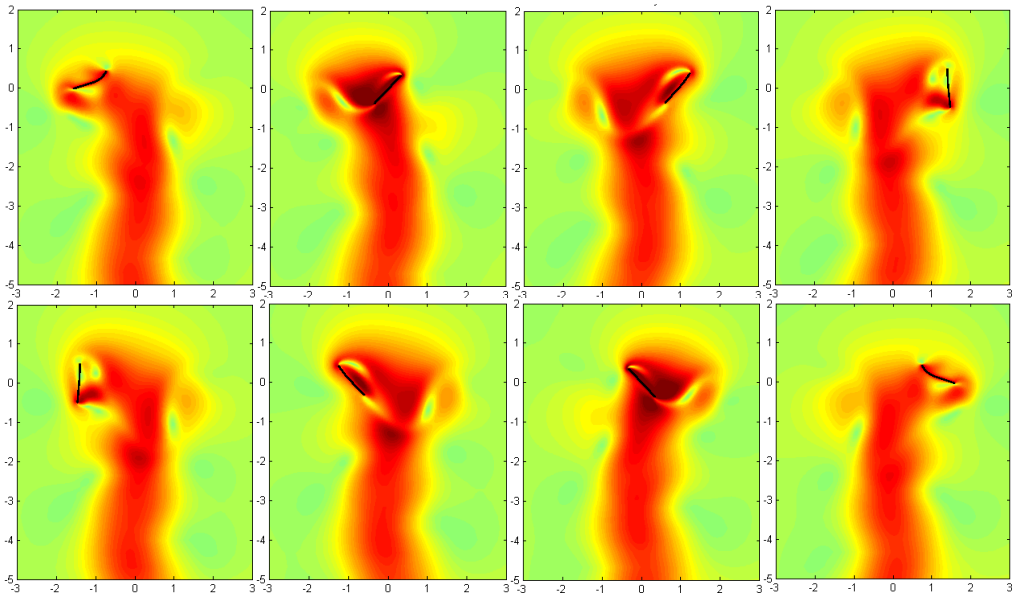

**Figure A.5: Case W3A25 magnitude velocity contour (0, 1) time lapse for frame interval T/8 on truncated domain (-3,3)×(-5,2) for one period.**

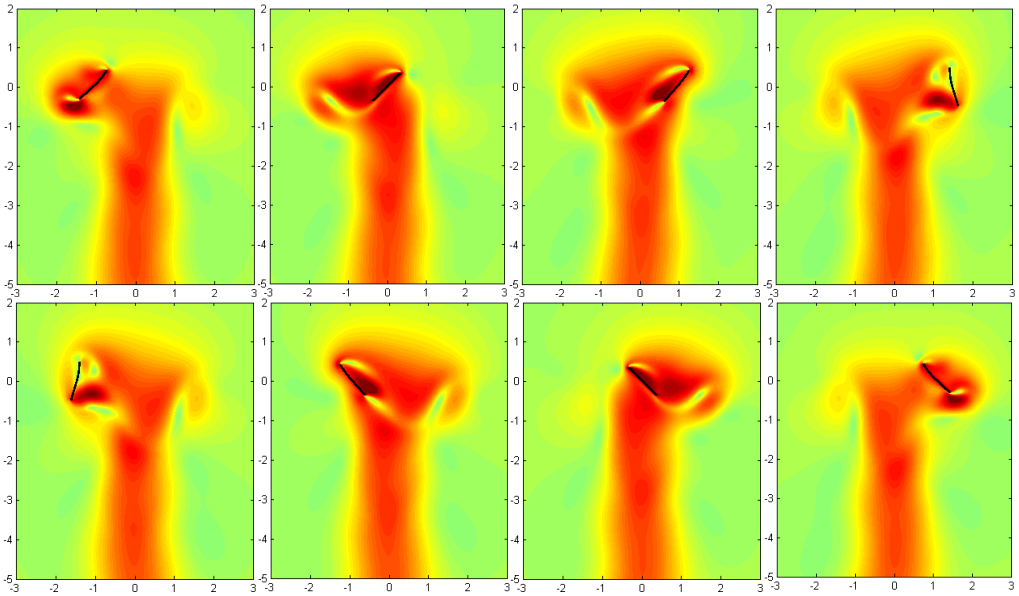

**Figure A.6: Case W4A25 magnitude velocity contour (0, 1) time lapse for frame interval T/8 on truncated domain (-3,3)×(-5,2) for one period.**

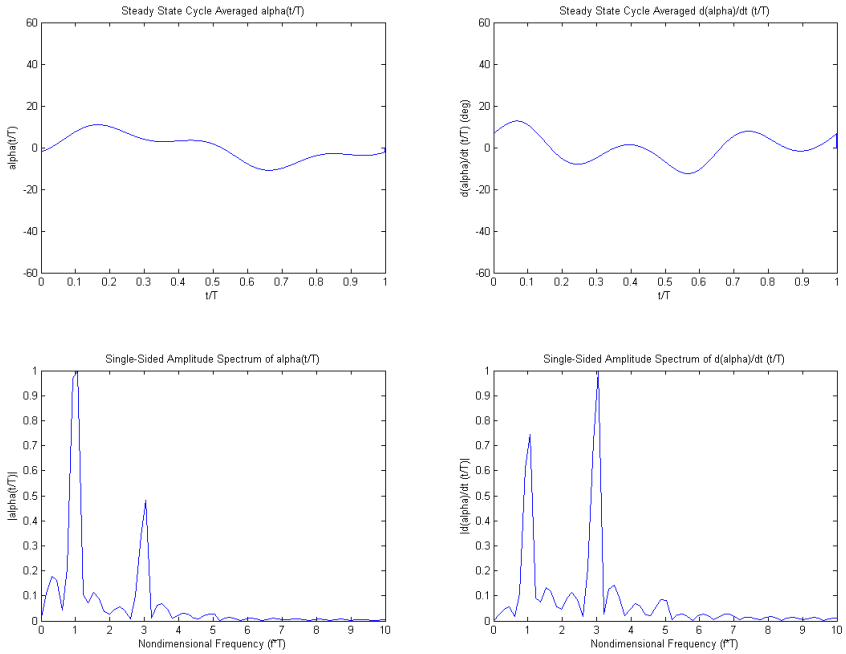


**Figure A.7: Steady state histories and FFTs for $\alpha$ (left) and $\dot{\alpha}$ (right) for Case W2A10. Amplitudes normalized by maximum magnitude component.**

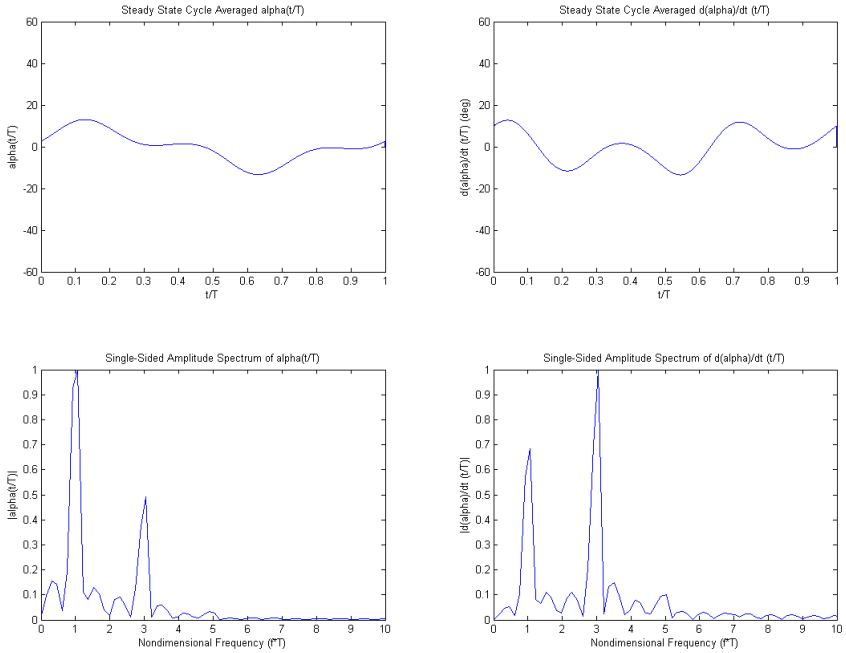


**Figure A.8: Steady state histories and FFTs for $\alpha$ (left) and $\dot{\alpha}$ (right) for Case W2A25. Amplitudes normalized by maximum magnitude component.**

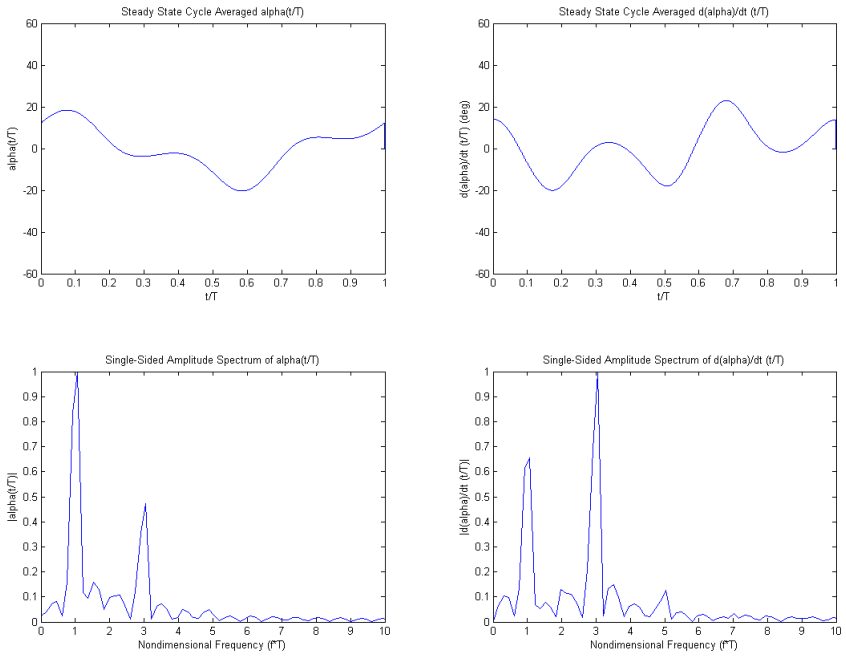


**Figure A.9: Steady state histories and FFTs for $\alpha$ (left) and $\dot{\alpha}$ (right) for Case W2A50. Amplitudes normalized by maximum magnitude component.**

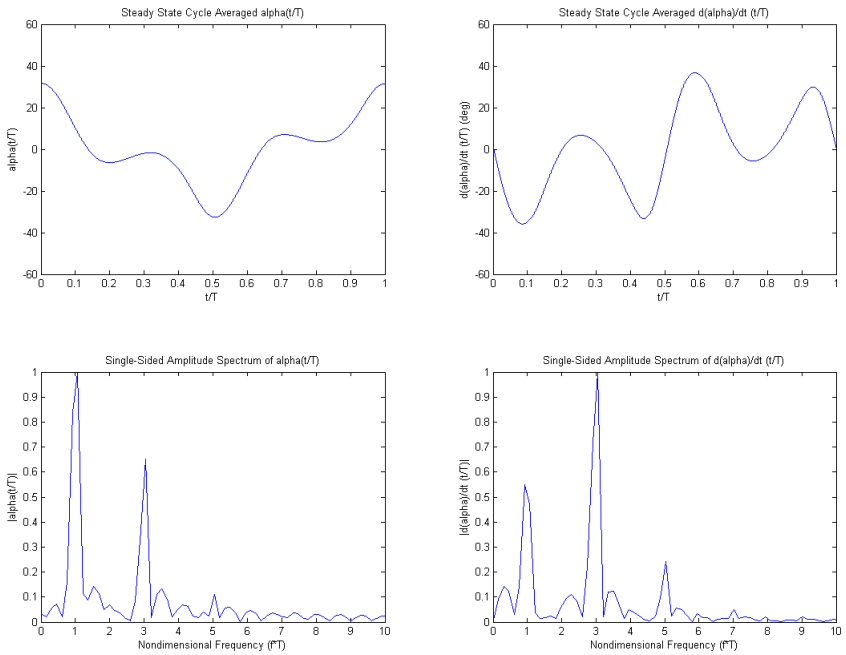


**Figure A.10: Steady state histories and FFTs for $\alpha$ (left) and $\dot{\alpha}$ (right) for Case W2A75. Amplitudes normalized by maximum magnitude component.**

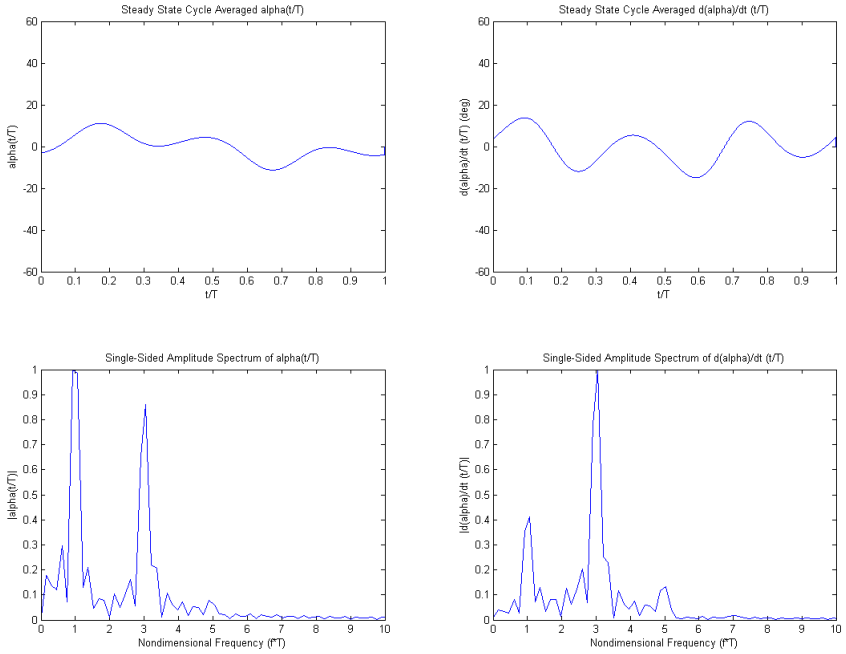


**Figure A.11: Steady state histories and FFTs for $\alpha$ (left) and $\dot{\alpha}$ (right) for Case W3A10. Amplitudes normalized by maximum magnitude component.**

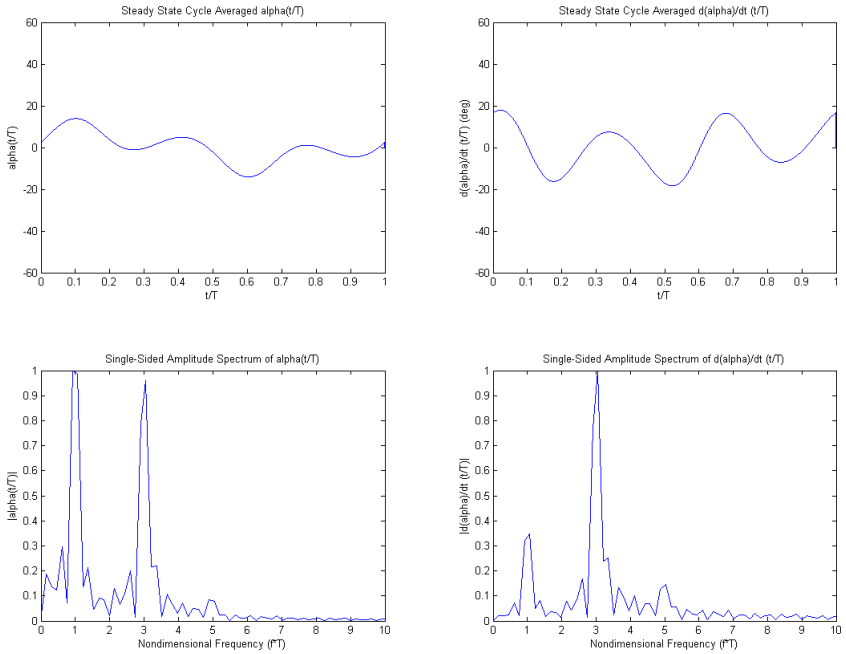


**Figure A.12: Steady state histories and FFTs for $\alpha$ (left) and $\dot{\alpha}$ (right) for Case W3A25. Amplitudes normalized by maximum magnitude component.**

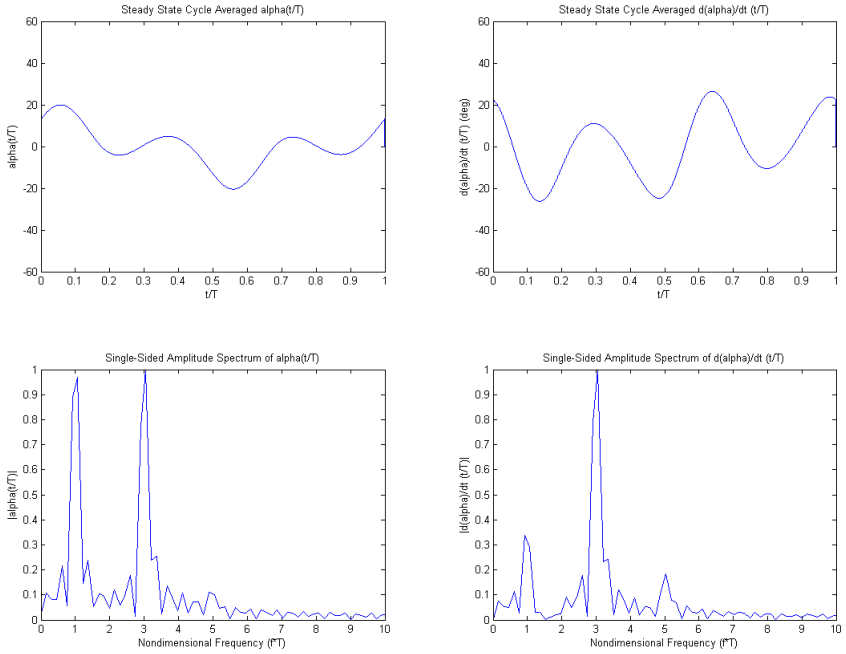


**Figure A.13: Steady state histories and FFTs for $\alpha$ (left) and $\dot{\alpha}$ (right) for Case W3A50. Amplitudes normalized by maximum magnitude component.**

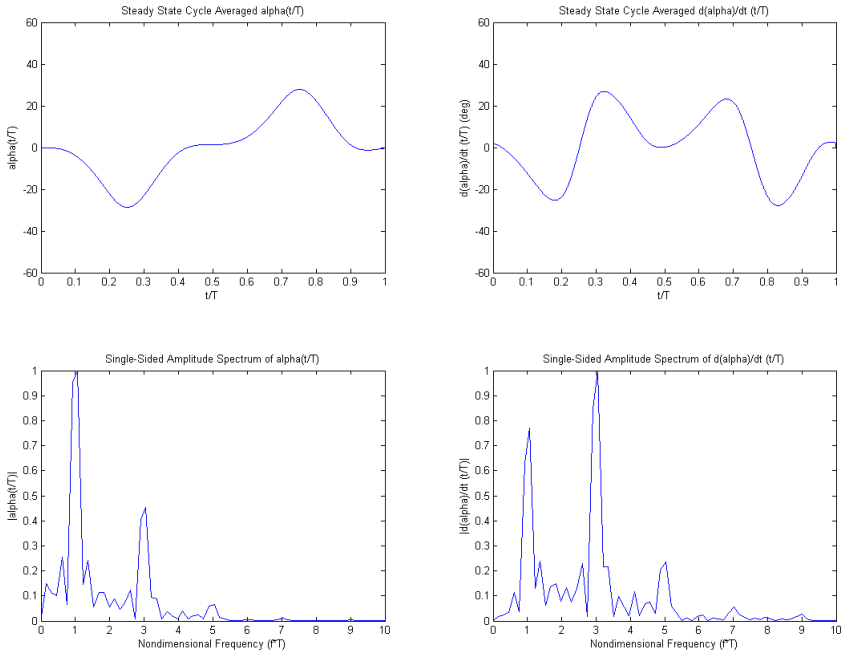


**Figure A.14: Steady state histories and FFTs for $\alpha$ (left) and $\dot{\alpha}$ (right) for Case W3A75. Amplitudes normalized by maximum magnitude component.**

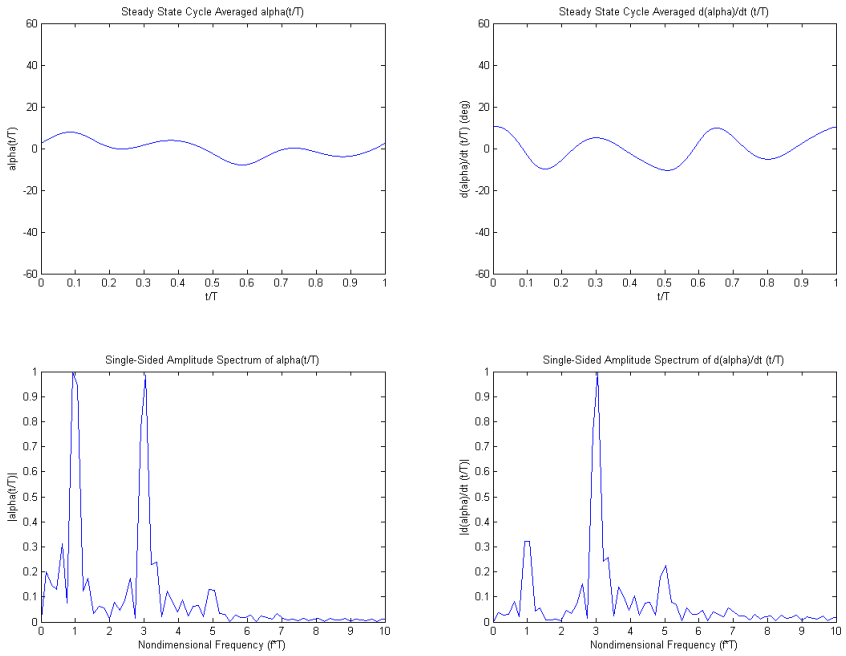


**Figure A.15: Steady state histories and FFTs for $\alpha$ (left) and $\dot{\alpha}$ (right) for Case W4A10. Amplitudes normalized by maximum magnitude component.**

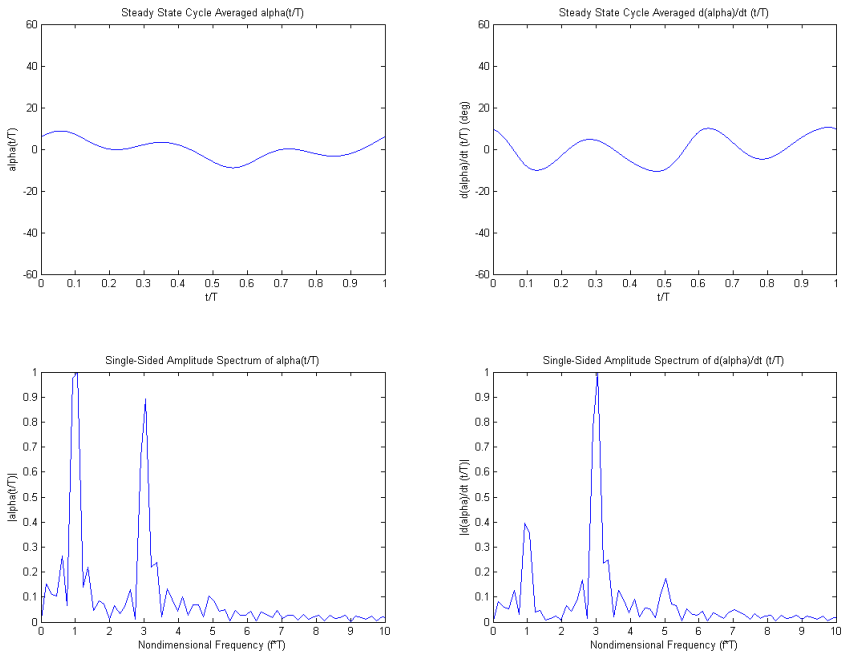


**Figure A.16: Steady state histories and FFTs for $\alpha$ (left) and $\dot{\alpha}$ (right) for Case W4A25. Amplitudes normalized by maximum magnitude component.**

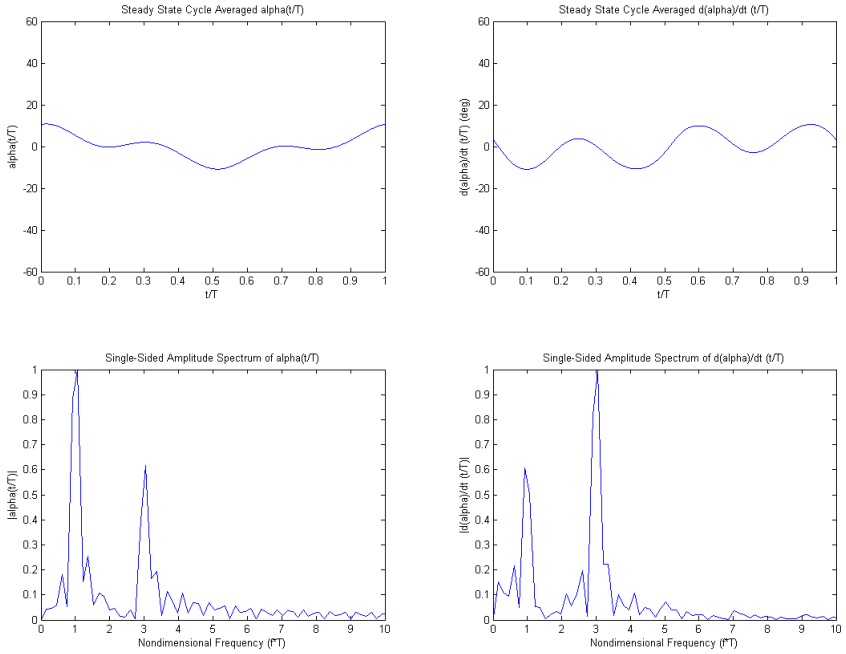


**Figure A.17: Steady state histories and FFTs for $\alpha$ (left) and $\dot{\alpha}$ (right) for Case W4A50. Amplitudes normalized by maximum magnitude component.**

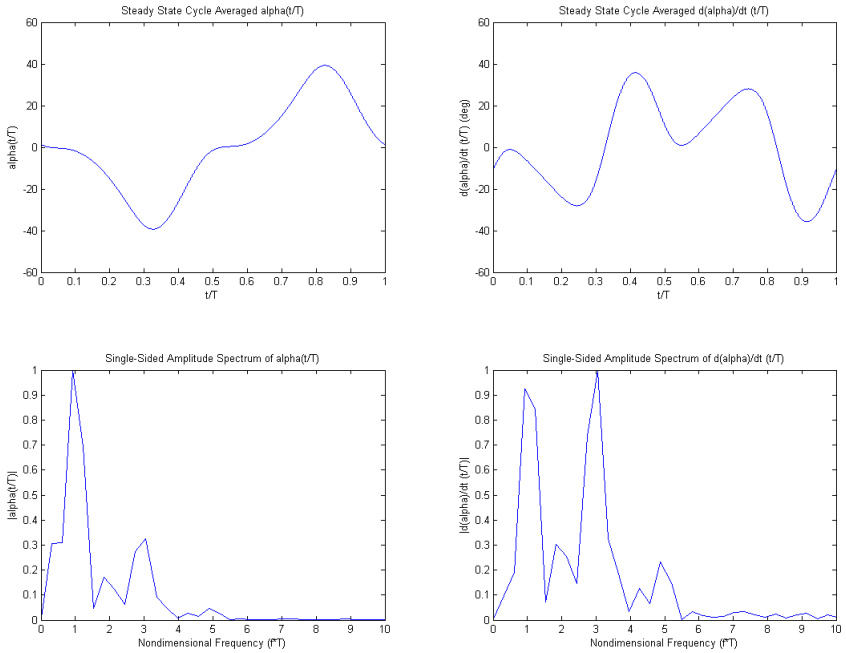


**Figure A.18: Steady state histories and FFTs for $\alpha$ (left) and $\dot{\alpha}$ (right) for Case W4A75. Amplitudes normalized by maximum magnitude component.**

**Figure A.19: Steady state cycle-averaged vorticity magnitude contour (0,1) on (-3,3)×(-5,2) grid for W2 and Link Length (top right to bottom left) A10, A25, A50, and A75. Amplitudes normalized by maximum magnitude component; 20 snapshots per period.**

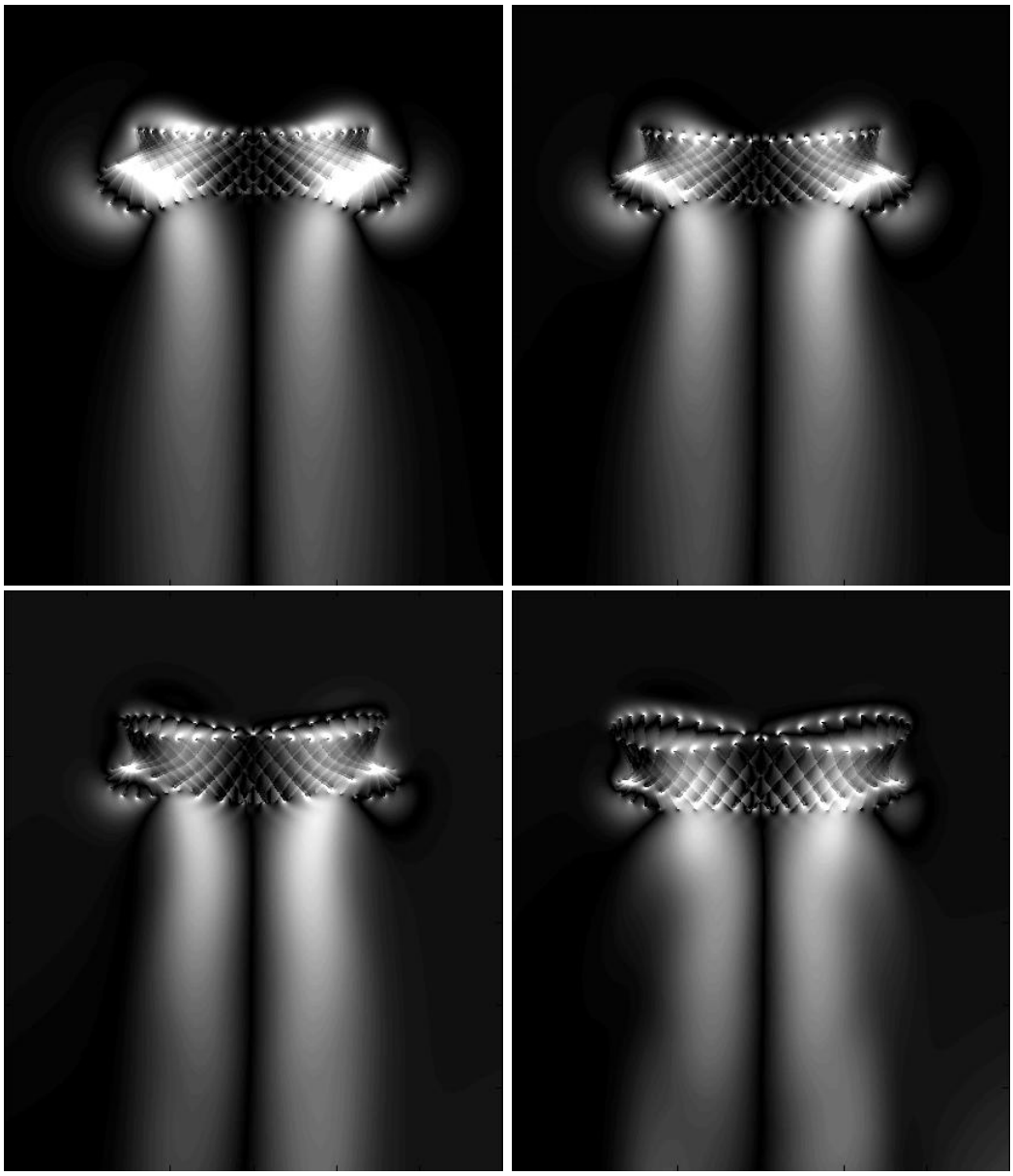

**Figure A.20: Steady state cycle-averaged vorticity magnitude contour (0,1) on (-3,3)×(-5,2) for W3 and Link Length (top right to bottom left) A10, A25, A50, and A75. Amplitudes normalized by maximum magnitude component; 40 snapshots per period.**

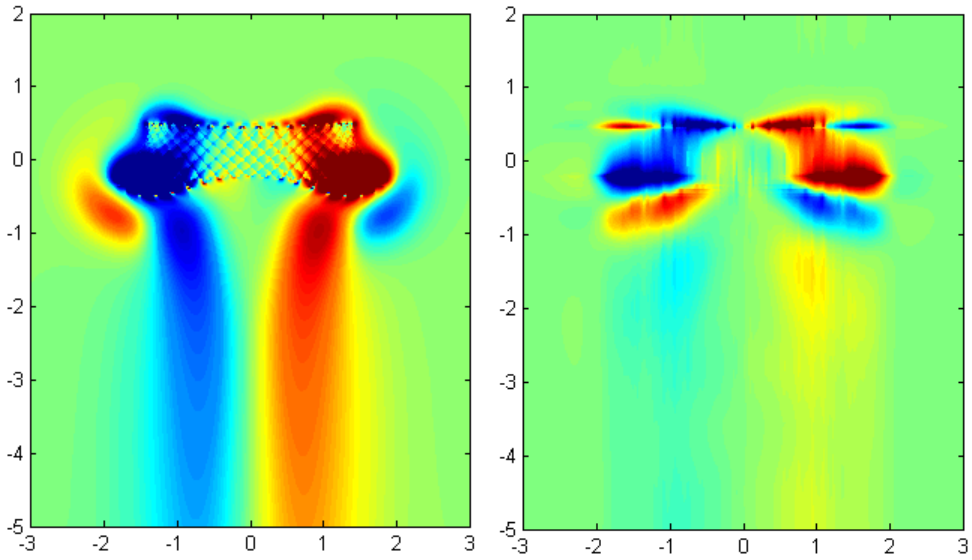


**Figure A.21: W4A10 Case: Steady state cycle-averaged vorticity (left) and SVD Modes 1-10 (right) Contours (-1,1) on (-3,3)×(-5,2) grid. Amplitudes normalized by maximum magnitude component; 40 snapshots per period.**

The SVD Modes 1-10 of the near-body vorticity field presented in Figure A.21 illustrate why the vorticity field is considered only in period-average. Modes of the horizontal and vertical velocity are found to be insightful and useful, whereas the SVD Modes of vorticity, the curl of the velocity field, produce few coherent structures.

## B. Appendix: Developed and Modified Codes

This appendix contains codes developed and codes modified during the course of this thesis work. These codes are as follows:

i) Spcoordroutines.f90 (*only subroutines added*)

The first subroutine was developed in order to drive the kinematics for a flexible wing with structural damping with unequal moments of inertia. The second subroutine was developed to translate the symmetrical wing harmonic kinematics, which used the pivot point as the prescribed position, to drive an asymmetrical wing from the same leading edge. This resulted in all cases considered with different wing section geometries following the same leading edge position and slope, originally defined for the prescribed kinematics of the symmetrical wing section.

ii) master_results.m (355 lines)

All parameters and variables of interest are computed in master_results.m from the raw data. Truncated variables that only contain steady-state information are built here and period averages, non-dimensonalized performance metrics, and plots are developed in this program.

iii) plot_data.m (278 lines)

All flow fields presented in figures in this work were produced using contour plots on the truncated domain developed in this program. Options exist for modifying the

truncated domain and plotting pressure, vorticity, velocity vector fields, and vertical, horizontal, and magnitude velocity from the raw flow field snapshots.

iv) FFT_alpha.m (200 lines)

The Fast Fourier Transforms were computed in FFT_alpha.m, which reads raw displacement and velocity data for the free link during steady-state periods and plots the variables and the first ten modes of their FFT for a specified case.

v) h5hyperslab.m (120 lines)

The full domain flow field snapshot data is saved in HDF5 format. h5hyperslab.m extracts the truncated domain of the "near-body" flow field and computes SVD modes, produces flow field and mode plots for single snapshots.

vi) svd_period.m (156 lines)

The full domain flow field snapshot data for one period is extracted on the truncated domain. The program then computes SVD modes for period averages, produces total and single-mode plots for period-averaged flow field data.

vii) vortcalc2.m (45 lines)

A grayscale image representing a vorticity contour on an equi-spaced grid on the truncated domain is read in and the mean magnitude vorticity and total circulation is computed and reported for a single case.

**Subroutines Added to** `spcoordroutines.f90`

```
! ******************************************************************
! ------------------------------------------------------------------
! Subroutine hovprofrestthetadampedfwd:
! Specified Hover for the generalized coordinate theta with
!  Transition to Forward Flight
! RESTRAINTS(i).restdof(j) = 13
! Time constant tau = 0.8*T (for hovering)
! Gives Oscillatory Steady State values for t/T > 5.5
! Time constant taufwd = 0.4*T (for transition to forward flight)
! Gives Oscillatory Steady State values for (t-tfwd)/T > 3.0
! Time of transition to Forward Flight is at t/T = 10
! ------------------------------------------------------------------
      subroutine hovprofrestthetadampedfwd(nmaxparamres,nparam,param, &
                                           time,spcoord)

      implicit none
      integer nmaxparamres,nparam
      real*8 param(nmaxparamres),time,spcoord(3)


      ! Local variables:
      real*8, parameter :: pi = 3.141592653589793
      real*8, parameter :: chord = 1.
      real*8 hovflag,Sta,Stc,Aoc,beta,tita0,amptita,phip
      real*8 frecp,ampo,tau,expttau
        real*8 taufwd,expttaufwd,timefwd,Tfwd,thetaoffset
      real*8 titad,titadd,tita

      hovflag = param(1);
      Sta     = param(2);
      Stc     = param(3);
      Aoc     = param(4);
      beta    = param(5);
      tita0   = param(6);
      amptita = param(7);
      phip    = param(8);
        thetaoffset = param(9); ! Added parameter
        Tfwd = param(10); ! Added parameter


      if (hovflag .EQ. 1) then
!c     In all cases umax is taken as 1
!c     In all cases the chord is taken as 1
         ampo  = Aoc*chord

         if (ampo .NE. 0) then
            frecp = 1.0/(ampo*pi)
         else
            frecp = 0
         endif

      elseif (hovflag .EQ. 2) then
!c        In all cases uo is taken as 1
```

```
!c        In all cases the chord is taken as 1
         frecp = Stc*1.0/chord

         if (frecp .NE. 0) then
            ampo  = Sta*1.0/frecp
         else
            ampo  = 0.
         endif
      endif

      tau = 0.8 * 1.0/frecp;
      expttau = exp(-time/tau)
        timefwd = Tfwd*1.0/frecp;
      taufwd = 0.4 * 1.0/frecp;
        !expttaufwd is 1 until time = timefwd, then decays to zero
        if (time .GE. timefwd) then
          expttaufwd = exp(-(time-timefwd)/taufwd);
        else
            expttaufwd = 1.;
      endif

        !Original Damped Hovering Kinematics are commented out
        !New kinematics implement transition to hovering after time =
tfwd
      !tita  = tita0 + (1.-expttau)*amptita*sin(2.*pi*frecp*time +
phip)
      tita = tita0 + (1.-expttau)*(thetaoffset*(1-expttaufwd) + &
          amptita*sin(2.*pi*frecp*time + phip))

      !titad = (1./tau)*expttau*amptita*sin(2.*pi*frecp*time + phip) +
&
      !     2.*(1.-expttau)*amptita*cos(2.*pi*frecp*time +
phip)*pi*frecp
      titad = (1.-expttau)*(thetaoffset*expttaufwd/taufwd + &
        2.*amptita*pi*frecp*cos(2.*pi*frecp*time+phip)) - &
          expttau*(thetaoffset*(expttaufwd-1.) - &
          amptita*sin(2.*pi*frecp*time+phip))/tau

      !titadd= -tau**(-2)*expttau*amptita*sin(2.*pi*frecp*time + phip)
+ &
      ! 4./tau*expttau*amptita*cos(2.*pi*frecp*time + phip)*pi*frecp -
&
      ! 4.*(1.-expttau)*amptita*sin(2.*pi*frecp*time + phip) * &
      ! pi**2 * frecp**2
      titadd = (expttau - 1.)*(thetaoffset*expttaufwd*taufwd**(-2) + &
          4.*amptita*pi**2*frecp**2*sin(2.*pi*frecp*time + phip)) + &
            (expttau*(thetaoffset*(expttaufwd - 1.) - &
            amptita*sin(2.*pi*frecp*time + phip)))*tau**(-2) + &
            2.*expttau*(thetaoffset*expttaufwd/taufwd + &
            2.*amptita*pi*frecp*cos(2.*pi*frecp*time + phip))/tau

      ! Theta generalized coordinate, velocity and accel:
      spcoord(1) = beta + tita;
      spcoord(2) = titad;
      spcoord(3) = titadd;
```

```
      return

      End subroutine
! ****************************************************************


! ----------------------------------------------------------------
! Subroutine TransformKinematics_DriveFromTip:
! To change kinematics to be driven from the tip, rather than the pin
! RESTRAINTS(i).restdof(j) = 23
! ----------------------------------------------------------------
      subroutine TransformKinematics_DrivingPt(spcoord_x, &
                                               spcoord_y, &
                                               spcoord_tita,length)

      implicit none
      real*8, INTENT(INOUT) :: spcoord_x(3)
      real*8, INTENT(INOUT) :: spcoord_y(3)
      real*8, INTENT(IN)    :: spcoord_tita(3)
      real*8, INTENT(IN)    :: length

      real*8 x(3),y(3),tita(3)
      real*8 sinT,cosT,thetad;

      ! where 'length' is the distance along from the pin joint along
      ! the link to where the kinematics are being applied
      ! therefore 'length = length_plate' means that the kinematics are
      ! driving the tip

      x      = spcoord_x;
      y      = spcoord_y;
      tita   = spcoord_tita;
      thetad = tita(2);

      cosT = cos(tita(1));
      sinT = sin(tita(1));

      ! Transpose x:
      spcoord_x(1) = x(1) - length*cosT;
      spcoord_x(2) = x(2) - length*(-thetad*sinT);
      spcoord_x(3) = x(3) - length*(-tita(3)*sinT -
thetad*thetad*cosT);

      ! Transpose y:
      spcoord_y(1) = y(1) - length*(sinT) - length + (0.5-length);
! an offset is added to y to place the leading edge at +0.5
      spcoord_y(2) = y(2) - length*(thetad*cosT);
      spcoord_y(3) = y(3) - length*(tita(3)*cosT - thetad*thetad*sinT);


      end subroutine
**********************************************************************
```

**master_results.m** (355 lines)

```
**************************************************************************
% master_results.m

% Based on plot_str.m in the "results" folders of each run
% This program plots structural results with the option of
% omitting transient data from the first few periods
clear all; close all; clc;

%% Choose the run
(directory information omitted)
%load FlatPlate_Re0075_wwf4.0_circ03_zeta0.00.mat

% --------------------------- Run Parameters --------------------------
---
rhoratio = 82.073;            % 25 for 10% thickness, 82.073 3% cases
omegaratio = 4.0;             % Ratio of forcing to natural frequency
kinematics_flag = 'harmonic'; % 'harmonic' for all current cases
dampingratio = 1.00;           %
thickness_percent = 3;        % 3 for all current cases
A = 0.50;                     % Leading link relative length (0-1)
Tstart = 0.5180001;              % Throw out the first few periods;
consider only steady state

%Plot limits
xlim = 2;
ylim = 2;
%-------------------------------------------------------------------------

Ox = A-0.5;     % Don't touch: Pivot Point location on normalized wing,
Ox = 0 for all A=0.5 cases.
                % (forced link on left, free link on right)
                % i.e., A=0.1 corresponds to Ox = -0.40;

% ALL runs are at Re = 75, FlatPlate with 3% thickness
% Steady State for final 5 Periods begin at:
(omitted)
% -------------------------------------------------------------------------

%Variables loaded from matrix file are:
%{
newtime
theta_rs_flt
x_rs_flt            %Contains 3 columns: x, dx/dt, d^2x/dt^2
y_rs_flt
CD_rs_flt
CDw_rs_flt
CL_rs_flt
CLw_rs_flt
Cma_rs_flt          %nondim moment about alpha
Cmt_rs_flt          %nondim moment about theta
alpha_rs_flt
fx_rs_flt
```

```
fy_rs_flt
ma_rs_flt
mt_rs_flt
%}

%% Plotting Parameters

T = 2.8*pi; %define the period

%build truncated variables
data_size = floor(length(newtime)-2.8*pi*Tstart/(newtime(2)-
newtime(1)));
time_short = zeros(data_size,1);
CD_short = zeros(data_size,1);
CL_short = zeros(data_size,1);
alpha_short = zeros(data_size,1);
alphadot_short = zeros(data_size,1);
x_short = zeros(data_size,1);
xdot_short = zeros(data_size,1);
y_short = zeros(data_size,1);
ydot_short = zeros(data_size,1);
theta_short = zeros(data_size,1);
thetadot_short = zeros(data_size,1);
%When Calculating Power:
%
fx_short = zeros(data_size,1);
fy_short = zeros(data_size,1);
ma_short = zeros(data_size,1);
mt_short = zeros(data_size,1);
%}

j = 1;
for i = drange(length(newtime)-data_size:length(newtime)),
   time_short(j) = newtime(i);
   CD_short(j) = CD_rs_flt(i);
   CL_short(j) = CL_rs_flt(i);
   alpha_short(j) = alpha_rs_flt(i,1);
   alphadot_short(j) = alpha_rs_flt(i,2);
   x_short(j) = x_rs_flt(i,1);
   xdot_short(j) = x_rs_flt(i,2);
   y_short(j) = y_rs_flt(i,1);
   ydot_short(j) = y_rs_flt(i,2);
   theta_short(j) = theta_rs_flt(i,1);
   thetadot_short(j) = theta_rs_flt(i,2);

   %For calculating power:
   %
   fx_short(j) = fx_rs_flt(i,1);
   fy_short(j) = fy_rs_flt(i,1);
   ma_short(j) = ma_rs_flt(i,1);
   mt_short(j) = mt_rs_flt(i,1);
   %}

   j=j+1;
```

```
end

%% Build Cycle-Averaged Variables for one Period
% Save number of periods
num_per = (max(time_short) - min(time_short))/T;
dt = time_short(2)-time_short(1);
numsteps = floor(T/dt); %Number of time steps per period
fy_ave = zeros(round(data_size/num_per),1);
for i = drange(1:round(num_per))
    for j = drange(1:numsteps)
       fy_ave(j) = fy_ave(j)+fy_short(j);
    end
    fy_ave = fy_ave/(round(num_per));
end
t_ave = [dt:dt:T]; % build time variable for one period
%plot(t_ave/T,fy_ave) % Example plot for period-averaged variable

%%
% navigate back to base directory
cd Z:\jrmax_runs\DampingSweep\newkinematics\Re0075

%% Power Calculations
%Added by Jesse Maxwell 9/13/12
%
%For identical link cases
%[na, ma, k, Ia] =
DimensionalCalcs(rhoratio,omegaratio,kinematics_flag,dampingratio,thick
ness_percent);
%[na, ma, k, Ia] =
DimensionalCalcs(25,wwf,kinematics_flag,0,thickness_percent);
%Body A, free link
[na, ma, ka, Ia, ca] =
DimensionalCalcs(rhoratio,omegaratio,kinematics_flag,dampingratio,thick
ness_percent,Ox, 1);
%Body B, forced link
[nb, mb, kb, Ib, cb] =
DimensionalCalcs(rhoratio,omegaratio,kinematics_flag,dampingratio,thick
ness_percent,-Ox, 1);
%For varied link length cases
%[na, ma, k, Ia, c]
=DimensionalCalcs(rhoratio,omegaratio,kinematics_flag,dampingratio,thic
kness_percent, hinge_point, screen_info);
%{
nb = na;
mb = ma;
Ib = Ia;
%}
grav = 0;

POW_tr_x = zeros(length(time_short),1);
POW_tr_y = zeros(size(POW_tr_x));
POW_rot = zeros(size(POW_tr_x));
Power_rot = zeros(size(POW_tr_x));
Power_tr = zeros(size(POW_tr_x));
Power_short = zeros(size(POW_tr_x));
```

```
%for loop done with 'variable' rather than 'signal.variable'
if( isnumeric(omegaratio) == 1 )
    for ii = 2:data_size;
        y1 = x_short(ii);           % x
        y2 = y_short(ii);           % y
        y3 = theta_short(ii);       % theta
        y4 = alpha_short(ii);       % alpha

        y5 = xdot_short(ii);           % xd
        y6 = ydot_short(ii);           % yd
        y7 = thetadot_short(ii);       % thetad
        y8 = alphadot_short(ii);       % alphad

        twodt = time_short(ii+1)-time_short(ii-1);
        y5d = (xdot_short(ii+1)-xdot_short(ii-1))/ twodt; % xdd
        y6d = (ydot_short(ii+1)-ydot_short(ii-1))/ twodt; % ydd
        y7d = (thetadot_short(ii+1)-thetadot_short(ii-1))/ twodt; %
thetadd
        y8d = (alphadot_short(ii+1)-alphadot_short(ii-1))/ twodt; %
alphadd

        % Resultant force in the x direction R = m*xdd - fx
        R_x = (ma+mb)*y5d +(-ma*na*sin(y3+y4) + mb*nb*sin(y3))*y7d +
...
              (-ma*na*sin(y3+y4))*y8d -( ma*na*cos(y3+y4)*(y7+y8)^2 -
...
             mb*nb*cos(y3)*y7^2) - fx_short(ii);


        % Resultant force in the y direction R_y = m*ydd - fy;
        R_y = (ma+mb)*y6d + (ma*na*cos(y3+y4) - mb*nb*cos(y3))*y7d +
ma*na*cos(y3+y4)*y8d  ...
         - ( ma*na*sin(y3+y4)*(y7+y8)^2 - mb*nb*sin(y3)*y7^2 )
...
         - (ma+mb)*grav ... ...
         - fy_short(ii);


        % Resultant torque in the theta direction TR = I*thetadd -
Mtheta
        MT = (-ma*na*sin(y3+y4) + mb*nb*sin(y3))*y5d + ...
             ( ma*na*cos(y3+y4) - mb*nb*cos(y3))*y6d + ...
             (Ia+Ib)*y7d + Ia*y8d - mt_short(ii) ;

        % Transtlational work:
        try
        POW_tr_x(ii,1) = R_x*y5;
        POW_tr_y(ii,1) = R_y*y6;
        catch
            fprintf(2,'Error.  ii = %d\n',ii)
            return
        end
```

```
        if POW_tr_x(ii,1) < 0
            POW_tr_x(ii,1) = 0;
        end

        if POW_tr_y(ii,1) < 0
            POW_tr_y(ii,1) = 0;
        end

        % Rotational work:
        POW_rot(ii,1)= MT*y7;

        if POW_rot(ii,1) < 0
            POW_rot(ii,1) = 0;
        end

        %            EN_elast(ii,1) = Kt * y4^2;
        %           POW_elast(ii,1)= -(Kt * y4) * y8;

    end
end

%POW_trmean  = mean( POW_tr_x(1:data_size,1)) + mean(
POW_tr_y(1:data_size,1));
%POW_rotmean = mean( POW_rot(1:data_size,1));
Power_tr = POW_tr_x + POW_tr_y;
Power_rot = POW_rot;
Power_short = Power_tr + Power_rot;
Power_avg = mean(Power_short);

% Define Power Coefficient, CP = (Ptr + Prot)/( 1/2 * rhof * Vc^3 * Lc)
% Definition from Fitzgerald, et al 2011
CP_short = Power_short/(0.5*1*1^3*1);


%% Plots
%
%PRINT USEFUL DATA
disp('  DATA SUMMARY')

max_per = (max(time_short))/T;
str = sprintf('Max Period:     %.3f',max_per);
disp(str);

num_per = (max(time_short) - min(time_short))/T;
str = sprintf('Num Periods:     %.3f',num_per);
disp(str);
%
%Average Lift Coefficient
CLavg = mean(CL_short);
str = sprintf('CLavg =          %.5f',CLavg);
disp(str);
%Average Drag Coefficient
CDavg = mean(CD_short);
```

```
str = sprintf('CDavg =          %.5f',CDavg);
disp(str);
%Average Power Coefficient
CPavg = mean(CP_short);
str = sprintf('CPavg =          %.5f',CPavg);
disp(str);
%Average Lift to Average Drag
CLCDavg = CLavg/CDavg;
str = sprintf('CLavg/CDavg =    %.5f',CLCDavg);
disp(str);
%Average Lift to Average Power
CLCPavg = CLavg/CPavg;
str = sprintf('CLavg/CPavg =    %.5f',CLCPavg);
disp(str);
%Average Fy
Fyavg = mean(fy_short);
str = sprintf('Fyavg =    %.5f',Fyavg);
disp(str);
%Average Fx
Fxavg = mean(fx_short);
str = sprintf('Fxavg =    %.5f',Fxavg);
disp(str);
%}
%{
CLCDavg2 = mean(CL_short./CD_short);
str = sprintf('(CL/CD)avg =     %.5f',CLCDavg2);
disp(str);
%}


%plot(time_short/T,CD_short,time_short/T,CL_short);

%{
%plot(time_short/T,CD_short)
fig = figure();
ax = axes('parent',fig);
%plot(newtime/T,alpha_rs_flt(:,1),'k',time_short/T,alpha_short)
%plot(alpha_short,CL_short,alpha_short,CD_short,alpha_short,alphadot_sh
ort)
plot(alphadot_short,CL_short,alphadot_short,CD_short,alphadot_short,alp
ha_short)
%plot(alpha_short,alphadot_short)
title('Steady State (t/T > 10)');
xlabel('Adot');
ylabel('CD(G), CL(B), A(R)');
set(ax,'DataAspectRatio',[1 1 1]);
set(ax,'XLim',[-xlim xlim],'YLim',[-ylim ylim]);
%}

%{
% Look at theta versus alpha in steady state
fig = figure();
ax = axes('parent',fig);
plot(theta_short*180/pi+90,alpha_short*180/pi)
set(ax,'XLim',[-60 60],'YLim',[-60 60]);
```

```
set(ax,'DataAspectRatio',[1 1 1]);
%}

% navigate back to base directory
cd Z:\jrmax_runs\DampingSweep\newkinematics\Re0075
**************************************************************************
```

**plot_data.m** (278 lines)

```
**************************************************************************
% plot_data.m
% Based on test_plot.m
% Creates separate plots for visualizing individual frames'
% flow fields. Seperately plot: Pressure,
% Vorticity, Velocity Magnitude (contour and arrow),
% Vertical Velocity and Horizontal Velocity
% User options WITHIN the code which variables to plot and plotting
parameters

%%
clear all ; close all ; clc

%% Parameters
%cd
'Z:\jrmax_runs\DampingSweep\newkinematics\Re0075\FlatPlate_wwf1.0_circ0
3_zeta1.0\frames_small'
%cd
'Z:\jrmax_runs\DampingSweep\newkinematics\Re0075\FixedMass\FlatPlate_ww
f3.0_circ03_LinkA0.25_zeta0.00\frames'
cd
'X:\Re0075\FixedMass\FlatPlate_wwf4.0_circ03_LinkA0.25_zeta0.00\frames'
baseprefix = '../FlatPlate_wwf4.0_circ03_zeta0.00/';
%cd
'Z:\jrmax_runs\DampingSweep\newkinematics\Re0075\FlatPlate_wwf3.0_circ0
3_LinkA0.50_zeta0.10\frames'
%baseprefix = '../FlatPlate_wwf3.0_circ03_zeta0.10/';
%cd
Z:\jrmax_runs\DampingSweep\newkinematics\Re0075\Transitional_Flight\Fla
tPlate_wwf2.0_circ03_LinkA0.50_zeta0.00_ThOff30\frames
%baseprefix = '../FlatPlate_wwf4.0_circ03_zeta0.00/';
%dirprefix = [baseprefix,'../frames_small/'];
dirprefix = [baseprefix,'../frames/'];
gridfile = 'grid.h5';

%Plots 1 = YES, 0 = NO
framenumber = 260;      % frame number to plot
%countours = 30;        % # of contours for each plot
xlim           =  3;%3    % horizontal plot limit centered around zero
ylim           =  2;%1    % vertical plot limit centered around zero
ylimlow        =  5;%5    % ylim;
plotgrid       =  0;    % Plot the grid over contour plots
numcontours    =  100;   % # of contours for each plot
plotpressure   =  0;    % Pressure
   pressurelimit    =  0.75;    % Contour Plot Limits
plotvorticity  =  0;    % Vorticity
   vortclip         =  3;    % Clip Max Vorticity Values
   vorticitylimit   =  3;    % Vorticity Plot Limits
plotvelocity   =  1;    % Velocity Magnitude
   velocitylimit    =  1;    % Velocity Plot Limits
plotquiver     =  0;    % arrow vectors on the velocity plot
   reductionfactor  = 20;  % must be integer, reduces # arrows ^2
```

```
   scalingfactor    = 0.75; % scaling factor for arrow length
plotu           =  0;    % Vertical Velocity
plotw           =  0;    % Horizontal Velocity
hfile = [dirprefix,sprintf('/uwp%04d.h5',framenumber)];

%%
x = hdf5read(gridfile,'/x');
xc = hdf5read(gridfile,'/xc');
z = hdf5read(gridfile,'/z');
zc = hdf5read(gridfile,'/zc');

%% load up Pressure
p = hdf5read(hfile,'/p');

if plotpressure == 1,
p = p-p(1,1);
% plot
fig = figure();
ax = axes('parent',fig);
contourf(ax,zc,xc,p,numcontours,'color','none')
set(ax,'DataAspectRatio',[1 1 1]);
set(ax,'XLim',[-xlim xlim],'YLim',[-ylimlow ylim]);
hold on

% plot the grid
if plotgrid == 1,
 nz = length(z);
 nx = length(x);

 for j = 1:nz;
    plot([z(j) z(j)],[x(1) x(end)],'k')
 end
 for i = 1:nx;
    plot([z(1) z(end)],[x(i) x(i)],'k')
 end
end

plot_body('./', framenumber, ax, 0, 0,'none','k')
title('Pressure');
set(ax,'Clim',[-pressurelimit pressurelimit])

end % end if plots

%% Vorticity
vort = hdf5read(hfile,'/vort');

if plotvorticity == 1,

% Reference Vorticity
vort = vort-vort(1,1);

%
% Clip Max & Min Values
```

```
%vortclip = vorticitylimit;
for i = 1:length(vort(:,1))
   for j = 1:length(vort(i,:))
      if vort(i,j) > vortclip,
          vort(i,j) = vortclip;
      end
      if vort(i,j) < -vortclip,
          vort(i,j) = -vortclip;
      end
   end
end
%}

% Normalize Vorticity
%vort = vort./max(max(abs(vort)));

% plot
fig = figure();
ax = axes('parent',fig);
contourf(ax,z,x,vort,numcontours,'color','none')
set(ax,'DataAspectRatio',[1 1 1]);
set(ax,'XLim',[-xlim xlim],'YLim',[-ylimlow ylim]);
hold on

% plot the grid
if plotgrid == 1,
 nz = length(z);
 nx = length(x);

 for j = 1:nz;
    plot([z(j) z(j)],[x(1) x(end)],'k')
 end
 for i = 1:nx;
    plot([z(1) z(end)],[x(i) x(i)],'k')
 end
end

plot_body('./', framenumber, ax, 0, 0,'none','k')
title('Vorticity');
%set(ax,'Clim',[-vorticitylimit vorticitylimit])
set(ax,'Clim',[-vortclip vortclip])

end % end if plots

%% Velocity Magnitude
uo = hdf5read(hfile,'/uo');
wo = hdf5read(hfile,'/wo');
vmag = sqrt(uo.^2+wo.^2);
vmax = max(max(vmag));

if plotvelocity == 1,
% plot
fig = figure();
ax = axes('parent',fig);
```

```
contourf(ax,z,x,vmag,numcontours,'color','none'); %,'edgecolor','none')
%contour(ax,z,x,vmag,contours)
set(ax,'DataAspectRatio',[1 1 1]);
set(ax,'XLim',[-xlim xlim],'YLim',[-ylimlow ylim]);
hold on
%{
if plotquiver == 1,
%build a sparser grid for plotting arrows
wosparse = zeros(size(wo));
[wrow wcol] = size(wo);
uosparse = zeros(size(uo));
[urow ucol] = size(uo);
for i = 1:reductionfactor:wrow,
   for j = 1:reductionfactor:wcol,
    wosparse(i,j) = wo(i,j);
   end
end
for i = 1:reductionfactor:urow,
   for j = 1:reductionfactor:ucol,
    uosparse(i,j) = uo(i,j);
   end
end
quiver(z,x,wosparse,uosparse,scalingfactor,'k-')
end % end if plotquiver
%}
% plot the grid
if plotgrid == 1,
 nz = length(z);
 nx = length(x);

 for j = 1:nz;
    plot([z(j) z(j)],[x(1) x(end)],'k')
 end
 for i = 1:nx;
    plot([z(1) z(end)],[x(i) x(i)],'k')
 end
end

% plot the body over the grid
plot_body('./', framenumber, ax, 0, 0,'none','k')
title('Velocity');
set(ax,'Clim',[-velocitylimit velocitylimit])

end % end if plots

if plotquiver == 1,
%build a sparser grid for plotting arrows
wosparse = zeros(size(wo));
[wrow wcol] = size(wo);
uosparse = zeros(size(uo));
[urow ucol] = size(uo);
for i = 1:reductionfactor:wrow,
   for j = 1:reductionfactor:wcol,
    wosparse(i,j) = wo(i,j);
   end
```

```
end
for i = 1:reductionfactor:urow,
   for j = 1:reductionfactor:ucol,
    uosparse(i,j) = uo(i,j);
   end
end
quiver(z,x,wosparse,uosparse,scalingfactor,'k-')
end % end if plotquiver


%% Vertical Velocity
uo = hdf5read(hfile,'/uo');

if plotu == 1,
% plot
fig = figure();
ax = axes('parent',fig);
contourf(ax,zc,x,uo,30,'color','none')
set(ax,'DataAspectRatio',[1 1 1]);
set(ax,'XLim',[-xlim xlim],'YLim',[-ylimlow ylim]);
hold on

% plot the grid
if plotgrid == 1,
 nz = length(z);
 nx = length(x);

 for j = 1:nz;
    plot([z(j) z(j)],[x(1) x(end)],'k')
 end
 for i = 1:nx;
    plot([z(1) z(end)],[x(i) x(i)],'k')
 end
end

% plot the body over the grid
plot_body('./', framenumber, ax, 0, 0,'none','k')
title('Vertical Velocity');
set(ax,'Clim',[-velocitylimit velocitylimit])
hold off

end % end if plots

%% Horizontal Velocity

wo = hdf5read(hfile,'/wo');

if plotw == 1,
% plot
fig = figure();
ax = axes('parent',fig);
contourf(ax,z,xc,wo,30,'color','none')
set(ax,'DataAspectRatio',[1 1 1]);
set(ax,'XLim',[-xlim xlim],'YLim',[-ylimlow ylim]);
```

```
hold on

% plot the grid
if plotgrid == 1,
 nz = length(z);
 nx = length(x);

 for j = 1:nz;
    plot([z(j) z(j)],[x(1) x(end)],'k')
 end
 for i = 1:nx;
    plot([z(1) z(end)],[x(i) x(i)],'k')
 end
end

% plot the body over the grid
plot_body('./', framenumber, ax, 0, 0,'none','k')
title('Horizontal Velocity');
set(ax,'Clim',[-velocitylimit velocitylimit])

end % end if plots

%% Navigate Back to Original Directory
cd 'Z:\jrmax_runs\DampingSweep\newkinematics\Re0075'
**************************************************************************
```

**FFT_alpha.m** (200 lines)

```
**************************************************************************
%FFT_alpha.m
% Based on master_results.m, but used strictly for FFT of data sets

clear all; close all; clc;

%% Choose the run
cd
Z:\jrmax_runs\DampingSweep\newkinematics\Re0075\FixedMass\FlatPlate_wwf
4.0_circ03_LinkA0.50_zeta0.00\results
load FlatPlate_Re0075_wwf4.0_circ03_A0.50.mat

% --------------------------- Run Parameters --------------------------
---
rhoratio = 82.073;            % 25 for 10% thickness, 82.073 3% cases
omegaratio = 4.0;             % Ratio of forcing to natural frequency
kinematics_flag = 'harmonic'; % 'harmonic' for all current cases
dampingratio = 0.0;           %
thickness_percent = 3;        % 3 for all current cases
A = 0.50;                     % Leading link relative length (0-1)
Tstart = 6.12500;               % Throw out the first few periods;
consider only steady state

%Plot limits
xlim = 2;
ylim = 2;
%-------------------------------------------------------------------------

Ox = A-0.5;     % Don't touch: Pivot Point location on normalized wing,
Ox = 0 for all A=0.5 cases.
                % (forced link on left, free link on right)
                % i.e., A=0.1 corresponds to Ox = -0.40;

% ALL runs are at Re = 75, FlatPlate with 3% thickness
% Steady State for final 5 Periods begin at:

% Varied Damping
%% Plotting Parameters

T = 2.8*pi; %define the period

%build truncated variables
data_size = floor(length(newtime)-2.8*pi*Tstart/(newtime(2)-
newtime(1)));
time_short = zeros(data_size,1);
alpha_short = zeros(data_size,1);
alphadot_short = zeros(data_size,1);
theta_short = zeros(data_size,1);
thetadot_short = zeros(data_size,1);

j = 1;
```

```
for i = drange(length(newtime)-data_size:length(newtime)),
   time_short(j) = newtime(i);
   alpha_short(j) = alpha_rs_flt(i,1);
   alphadot_short(j) = alpha_rs_flt(i,2);
   theta_short(j) = theta_rs_flt(i,1);
   thetadot_short(j) = theta_rs_flt(i,2);

   j=j+1;
end

%% Build Cycle-Averaged Variables for one Period
% Save number of periods
num_per = (max(time_short) - min(time_short))/T;
dt = time_short(2)-time_short(1);
numsteps = round(T/dt); %Number of time steps per period ***round was
floor
%fy_ave = zeros(round(data_size/num_per),1);
alpha_ave = zeros(round(data_size/num_per),1);
alphadot_ave = zeros(round(data_size/num_per),1);
for i = drange(1:round(num_per))
    for j = drange(1:numsteps)
       %fy_ave(j) = fy_ave(j)+fy_short(j);
       alpha_ave(j) = alpha_ave(j)+alpha_short(j);
       alphadot_ave(j) = alphadot_ave(j)+alphadot_short(j);
    end
    %fy_ave = fy_ave/(round(num_per));
    alpha_ave = alpha_ave/(round(num_per));
    alphadot_ave = alphadot_ave/(round(num_per));
end
t_ave = [0:dt:T]; % build time variable for one period
%plot(t_ave/T,alpha_ave) % Example plot for period-averaged variable

%%
% navigate back to base directory
cd Z:\jrmax_runs\DampingSweep\newkinematics\Re0075

%% FFT

L = length(time_short);
NFFT = 2^nextpow2(L); % Next power of 2 from length of y
Y = fft(alpha_short,NFFT)/L;
f = 1/dt/2*linspace(0,1,NFFT/2+1);
F = f*T; % Nondimensionalize
%{
fig = figure();
ax = axes('parent',fig);
plot(F,2*abs(Y(1:NFFT/2+1)))
title('Single-Sided Amplitude Spectrum of alpha(t/T)')
xlabel('Nondimensional Frequency (f*T)')
ylabel('|alpha(t/T)|')
set(ax,'XLim',[0 10],'YLim',[0 1]);
%}

% Do the same for Alphadot
```

```
Y2 = fft(alphadot_short,NFFT)/L;
f2 = 1/dt/2*linspace(0,1,NFFT/2+1);
F2 = f2*T; % Nondimensionalize

%% Plot all results together
%
fig = figure();

subplot(2,2,1);
%Plot steady state averaged values for alpha and alpha dot
%ax = axes('parent',fig);
plot(t_ave/T,alpha_ave*180/pi)
hold on;
title('Steady State Cycle Averaged alpha(t/T)')
xlabel('t/T')
ylabel('alpha(t/T)')
%set(ax,'XLim',[0 1],'YLim',[-30 30]);
axis([ 0 1 -60 60]);

subplot(2,2,2)
%ax = axes('parent',fig);
plot(t_ave/T,alphadot_ave*180/pi)
title('Steady State Cycle Averaged d(alpha)/dt (t/T)')
xlabel('t/T')
ylabel('d(alpha)/dt (t/T) (deg)')
%set(ax,'XLim',[0 1],'YLim',[-30 30]);
axis([ 0 1 -60 60]);
%}

subplot(2,2,3)
%ax = axes('parent',fig);
Y1max = max(max(2*abs(Y(1:NFFT/2+1))));
plot(F,2*abs(Y(1:NFFT/2+1))/Y1max)
title('Single-Sided Amplitude Spectrum of alpha(t/T)')
xlabel('Nondimensional Frequency (f*T)')
ylabel('|alpha(t/T)|')
%set(ax,'XLim',[0 10],'YLim',[0 1]);
axis([ 0 10 0 1]);

subplot(2,2,4)
%ax = axes('parent',fig);
Y2max = max(max(2*abs(Y2(1:NFFT/2+1))));
plot(F2,2*abs(Y2(1:NFFT/2+1))/Y2max)
title('Single-Sided Amplitude Spectrum of d(alpha)/dt (t/T)')
xlabel('Nondimensional Frequency (f*T)')
ylabel('|d(alpha)/dt (t/T)|')
%set(ax,'XLim',[0 10],'YLim',[0 1]);
axis([ 0 10 0 1]);
**************************************************************************
```

**h5hyperslab.m** (120 lines)

```
**************************************************************************
%Create a truncated domain from the HDF5 structured grid and plot
results

clear all; close all; clc;

cd
'Z:\jrmax_runs\DampingSweep\newkinematics\Re0075\FixedMass\FlatPlate_ww
f2.0_circ03_LinkA0.10_zeta0.00\frames';
baseprefix = '../FlatPlate_wwf2.0_circ03_zeta0.00/';
%dirprefix = [baseprefix,'../frames_small/'];
dirprefix = [baseprefix,'../frames/'];
gridfile = 'grid.h5';

%Plots 1 = YES, 0 = NO
framenumber = 100;      % frame number to plot
%   num_countours = 30;        % # of contours for each plot
xlim           =  3.5;    % horizontal plot limit centered around zero
ylim           =  2.5;    % vertical plot limit centered around zero
ylimlow        =  5.5;    % ylim;
plotgrid       =  0;    % Plot the grid over contour plots
numcontours    =  30;   % # of contours for each plot
plotpressure   =  0;    % Pressure
   pressurelimit    =  .75;    % Contour Plot Limits
plotvorticity  =  0;    % Vorticity
   vorticitylimit   =  1;    % Vorticity Plot Limits
plotvelocity   =  1;    % Velocity Magnitude
   velocitylimit    =  1;    % Velocity Plot Limits
plotquiver     =  0;    % arrow vectors on the velocity plot
   reductionfactor  = 20;  % must be integer, reduces # arrows ^2
   scalingfactor    = 0.75; % scaling factor for arrows
plotu          =  0;    % Vertical Velocity
plotw          =  0;    % Horizontal Velocity
hfile = [dirprefix,sprintf('/uwp%04d.h5',framenumber)];

% x=1229, z=551
% [xl yl xr yr] = [15 26 498 1180] creates box [(-3,-5)(3,1)]
% [xl yl xr yr] = [15 26 512 1180] creates box [(-3,-5)(3,2)]

xl = 15; %15;
yl = 26;
xr = 512; %498;
yr = 1180;
x = h5read(gridfile,'/x',xl,xr);
xc = h5read(gridfile,'/xc',xl,xr);
z = h5read(gridfile,'/z',yl,yr);
zc = h5read(gridfile,'/zc',yl,yr);

%% load up Pressure
%p = hdf5read(hfile,'/p');
%data = hdf5read(working_file,[1 1],[5 3]);
data = h5read(hfile,'/p',[xl yl],[xr yr]);
```

```
data = data-data(1,1);
%{
% plot
fig = figure();
ax = axes('parent',fig);
contourf(ax,zc,xc,data,numcontours,'color','none')
set(ax,'DataAspectRatio',[1 1 1]);
set(ax,'XLim',[-xlim xlim],'YLim',[-ylimlow ylim]);
set(ax,'Clim',[-pressurelimit pressurelimit]);
%}
%%
% Change back to parent directory
cd 'Z:\jrmax_runs\DampingSweep\newkinematics\Re0075';

%
%I = imread('Rainier_small.jpg');
%I = im2double(I);
%I = rgb2gray(I);
[U S V] = svd(data);
%imshow(data);

%Choose number of SVD modes to rebuild
j = 10;

data2 = U(:,1:j)*S(1:j,1:j)*V(:,1:j)';
%imshow(Iaj);

% plot
fig = figure();
ax = axes('parent',fig);
contourf(ax,zc,xc,data2,numcontours,'color','none')
set(ax,'DataAspectRatio',[1 1 1]);
set(ax,'XLim',[-xlim xlim],'YLim',[-ylimlow ylim]);
set(ax,'Clim',[-pressurelimit pressurelimit])
%}
%{
[U,S,V] = svd(X,0);
ranks = [1 2 5 10 20 rank(X)];
for k=ranks(:)'
Xhat = (U(:,1:k)*S(1:k,1:k)*V(:,1:k)');
image(Xhat);
end
%}
```

**********

**svd_period.m** (156 lines)

```
**************************************************************************
%svd_period.m
%Load HDF5 snapshot frames and compute SVD modes on period averages
% or just plot the period average without deconstruction
clear all; close all; clc;

cd
'Z:\jrmax_runs\DampingSweep\newkinematics\Re0075\FixedMass\FlatPlate_ww
f4.0_circ03_LinkA0.75_zeta0.00\frames';
baseprefix = '../FlatPlate_wwf4.0_circ03_zeta0.00/';
%dirprefix = [baseprefix,'../frames_small/'];
dirprefix = [baseprefix,'../frames/'];
gridfile = 'grid.h5';

%Plots 1 = YES, 0 = NO
framenumber = 240;      % frame number to plot
number_of_frames = 40;  % number of frames to include (20 per period)
% Fixed Mass
%   W2 outputs 20 frames/period, last frame is 140
%   W3 outputs 40 frames/period, last frame is 280
%   W4 outputs 40 frames/period, last frame is 280
%   W6 outputs 40 frames/period, go from 376-416


xlim           =  3;    % horizontal plot limit centered around zero
ylim           =  2;    % vertical plot limit centered around zero
ylimlow        =  5;    % ylim;
plotgrid       =  0;    % Plot the grid over contour plots
numcontours    =  30;   % # of contours for each plot
plotpressure   =  0;    % Pressure
   pressurelimit    =  1;    %1, Contour Plot Limits
   vortlimit        =  1.5;    %1.5, Contour Plot Limits

hfile = [dirprefix,sprintf('/uwp%04d.h5',framenumber)];

%%
% Hyperslab
% x=1229, z=551
% [xl yl xr yr] = [15 26 498 1180] creates box [(-3,-5)(3,1)]
% [xl yl xr yr] = [15 26 512 1180] creates box [(-3,-5)(3,2)]

xl = 15; %15;
yl = 26;
xr = 512; %498;
yr = 1180;
x = h5read(gridfile,'/x',xl,xr);
xc = h5read(gridfile,'/xc',xl,xr);
z = h5read(gridfile,'/z',yl,yr);
zc = h5read(gridfile,'/zc',yl,yr);

%% Load Frames
```

```
data = h5read(hfile,'/p',[xl yl],[xr yr]);
total_data = data*0;     % Initialize total_data, SVD Dataset
raw_data = data*0;       % Initialize raw_data, Period Avg Dataset

for i=1:number_of_frames,
% load up Pressure for Current Frame
%p = hdf5read(hfile,'/p');
%data = hdf5read(working_file,[1 1],[5 3]);

% Choose Variable to Load
% /p, /uo, /wo, /vort
data = h5read(hfile,'/wo',[xl yl],[xr yr]);

data = data-data(1,1); % Set zero reference (offset)

[U S V] = svd(data);
j = 10;
data2 = U(:,1:j)*S(1:j,1:j)*V(:,1:j)';
total_data = total_data+data2;  % SVD Dataset
raw_data = raw_data + data;     % Period Avg Dataset

framenumber = framenumber+1;
hfile = [dirprefix,sprintf('/uwp%04d.h5',framenumber)];
end %End Frame Loop
%%
% Remove Offset
raw_data = raw_data-raw_data(1,1);
%Reduce total_data to the period-average
total_data = total_data/number_of_frames;
raw_data = raw_data/number_of_frames;
%Average SVD Variable Quantity
str = sprintf('SVD Var Avg =    %.5f',mean(mean(total_data)));
disp(str);
%Average Raw Variable Quantity
str = sprintf('Raw Var Avg =    %.5f',mean(mean(raw_data)));
disp(str);
%
%Normalize such that max magnitude of any value is 1
total_data_N = total_data/max(max(abs(total_data)));
raw_data_N = raw_data/max(max(abs(raw_data)));
%Average NORMALIZED SVD Variable Quantity
str = sprintf('N SVD Var Avg =    %.5f',mean(mean(total_data_N)));
disp(str);
%Average NORMALIZED Raw Variable Quantity
str = sprintf('N Raw Var Avg =    %.5f',mean(mean(raw_data_N)));
disp(str);
%}

%% Plot data
%
% Plot non-normalized data
% Contour Plot with Color Shades (no lines)
fig = figure();
ax = axes('parent',fig);
```

```
%contourf(ax,zc,xc,total_data,numcontours,'color','none')
contourf(ax,zc,xc,raw_data,numcontours,'color','none')
set(ax,'DataAspectRatio',[1 1 1]);
set(ax,'XLim',[-xlim xlim],'YLim',[-ylimlow ylim]);
set(ax,'Clim',[-pressurelimit pressurelimit])
%}
%{
% Plot Data -Greyscale
fig = figure();
ax = axes('parent',fig);
%contourf(ax,zc,xc,abs(total_data),256,'color','none')
contourf(ax,zc,xc,abs(raw_data),256,'color','none')
set(ax,'DataAspectRatio',[1 1 1]);
set(ax,'XLim',[-xlim xlim],'YLim',[-ylimlow ylim]);
set(ax,'Clim',[0 vortlimit])
set(gcf, 'colormap', gray)
%}
%{
% Plot Normalized Data -Greyscale
fig = figure();
ax = axes('parent',fig);
%contourf(ax,zc,xc,total_data_N,numcontours,'color','none')
contourf(ax,zc,xc,raw_data_N,numcontours,'color','none')
set(ax,'DataAspectRatio',[1 1 1]);
set(ax,'XLim',[-xlim xlim],'YLim',[-ylimlow ylim]);
set(ax,'Clim',[-pressurelimit pressurelimit])
set(gcf, 'colormap', gray)
%}
%{
% Plot Normalized Data
fig = figure();
ax = axes('parent',fig);
%contourf(ax,zc,xc,total_data_N,numcontours,'color','none')
contourf(ax,zc,xc,raw_data_N,numcontours,'color','none')
set(ax,'DataAspectRatio',[1 1 1]);
set(ax,'XLim',[-xlim xlim],'YLim',[-ylimlow ylim]);
set(ax,'Clim',[-pressurelimit pressurelimit])
%}
%{
% Contour Plot with 20 Lines
fig = figure();
ax = axes('parent',fig);
contourf(ax,zc,xc,total_data,20)
%contourf(ax,zc,xc,raw_data,20)
%contourf(ax,zc,xc,raw_data_N,20)
%contourf(ax,zc,xc,total_data_N,20)
set(ax,'DataAspectRatio',[1 1 1]);
set(ax,'XLim',[-xlim xlim],'YLim',[-ylimlow ylim]);
set(ax,'Clim',[-pressurelimit pressurelimit])
%}

% Change back to parent directory
cd 'Z:\jrmax_runs\DampingSweep\newkinematics\Re0075';
**************************************************************************
```

**vortcalc2.m** (45 lines)

```
**************************************************************************
%% vortcalc2.m
% Read in an image in greyscale and compute total magnitude vorticity
% and total circulation on truncated domain of image
clear all;

%% Navigate to Working Directory
cd 'C:\Documents and Settings\Jesse\Desktop\'

%I = imread('W3_A50_J1_W_2T_n.png');
I = imread('TestImage2.jpg');
Idouble = im2double(I);
Igrey = rgb2gray(Idouble);

%Renormalize
%IgreyN = Igrey-Igrey(5,5);
%min(min(I))
%max(max(I))
%mean(I)
%Average Raw Variable Quantity
str = sprintf('Mean Vort  =    %.5f',mean(mean(Igrey)));
disp(str);
str = sprintf('Total Circ =    %.5f',sum(sum(Igrey)));
disp(str);

%
[U S V] = svd(Igrey);
imshow(Igrey);

j = 100;
Iaj = U(:,1:j)*S(1:j,1:j)*V(:,1:j)';
imshow(Iaj);
%}

%{
[U,S,V] = svd(X,0);
ranks = [1 2 5 10 20 rank(X)];
for k=ranks(:)'
Xhat = (U(:,1:k)*S(1:k,1:k)*V(:,1:k)');
image(Xhat);
end
%}

%% Navigate Back to Original Directory
cd 'Z:\jrmax_runs\DampingSweep\newkinematics\Re0075'
**************************************************************************
```

**Bibliography**

Anderson, J.D. (2007), *Fundamentals of Aerodynamics*, 4th Ed., McGraw-Hill.

Chabalko, C., Fitzgerald, T., Valdez, M. and Balachandran, B. (2012), Flapping Aerodynamics and Ground Effect. 50th AIAA Aerospace Sciences Meeting including the New Horizons Forum and Aerospace Exposition, Nashville, Tennessee

Clancy, L.J. (1975), *Aerodynamics*, Section 3.3, Pitman Publishing Limited, London.

Dickinson, M. H., Lehmann, F. O. and Sane, S. P. (1999). Wing rotation and the aerodynamic basis of insect flight. *Science* 284, 1954-1960.

Ellington, C. P., Van den Berg, C., Willmott, A. P. and Thomas, A. L. (1996), Leading edge vortices in insect flight. *Nature* 384, 626-630.

Ferziger, J.H. and Peric, M. (1997), *Computational Methods for Fluid Dynamics*, Springer

Fitzgerald, T., Valdez, M. and Balachandran, B. (2011b), A comparison of computational models for fluid-structure interaction studies of flexible flapping wing systems. 49th AIAA Aerospace Sciences Meeting including the New Horizons Forum and Aerospace Exposition, Orlando, Florida

Fitzgerald, T., Valdez, M. and Balachandran, B. (2010), Flexible Hovering Wing Motions: Proper Orthogonal Decomposition Analysis. 48th AIAA Aerospace Sciences Meeting Including the New Horizons Forum and Aerospace Exposition, Orlando, Florida

Fitzgerald, T., Valdez, M., Vanella, M., Balaras, E., and Balachandran, B. (2011) Flexible Flapping Systems: Computational Investigations into Fluid-Structure Interactions. *Royal Aeronautical Society*, Vol. 115, No. 1172

Gatesy, S. M. and Dial, K. P. (1996), Locomotor Modules and the Evolution of Avian Flight. *Evolution*: Vol. 50, No. 1, pp. 331-340

Gopalakrishnan, P. and Tafti, D.K.,(2010), Effect of Wing Flexibility on Lift and Thrust Production in Flapping Flight. *AIAA Journal*, Vol. 48, No. 5

Katz, J. (1991), *Low-speed aerodynamics: From wing theory to panel methods*. McGraw-Hill. New York: McGraw-Hill.

Liu, H. and Kawachi, K. (1998). A numerical study of insect flight. *Journal of Computational Physics*, 146, 124-156.

Liu, H., Ellington, C.P., Kawachi, K., Van Den Berg, C. and Willmott, A.P. (1998), A Computational Fluid Dynamic Study of Hawkmoth Hovering. *Journal of Experimental Biology*, 1998, 201, pp 461-477.

Persson, P. O., Willis, D. J. and Peraire, J. (2012), Numerical simulation of flapping wings using a panel method and a high-order Navier–Stokes solver. *International Journal for Numerical Methods in Engineering*. Vol. 89, Iss. 10, pp 1296–1316

Preidikman, S. (1998), Numerical simulations of interactions among aerodynamics, structural dynamics, and control systems. Ph.D. Dissertation, Department of Engineering Science and Mechanics, Virginia Tech, 1998.

Ramamurti, R. and Sandberg, W. (2002). A three-dimensional computational study of the aerodynamic mechanisms of insect flight. *Journal of Experimental Biology*, 205, 1507-1518.

Sane, S. P. (2003), The aerodynamics of insect flight, *Journal of Experimental Biology* 206: 4191–4208

Sane, S. P. and Dickinson, M. H. (2001), The control of flight force by a flapping wing: lift and drag production. *Journal of Experimental Biology* 204, 2607–2626

Simmons, N., Seymour, K., Habersetzer, J., and Gunnel, G. (2008), Primitive Early Eocene bat from Wyoming and the evolution of flight and echolocation. *Nature* 451, 818-821

Sun, M. and Tang, J. (2002). Unsteady aerodynamic force generation by a model fruit fly wing in flapping motion. *Journal of Experimental Biology*, 2002, 205, 55-70.

Valdez, M.F., Preidikman, S. and Massa, J. (2006), Aerodynamics of two-dimensional and unsteady flows dominated by vorticity, *Computational Mechanics*, 2006, 24, pp 2333-2357. (in Spanish).

Valdez, M.F., Preidikman, S., Massa, J. C. and Balachandran, B. and Mook, D. T. (2008), Aerodynamics of 2D Unsteady Vorticity Dominated Flows. 10th Pan American Congress of Applied Mechanics, 2008, 12, pp 280-283.

Vandenberghe, N., Zhang, J., Childress, S. (2004), Symmetry breaking leads to forward flapping flight. *Journal of Fluid Mechanics*. Vol. 506, pp. 147-155

Vandenberghe, N., Zhang, J., Childress, S. (2006), On unidirectional flight of a free flapping wing. *Physics of Fluids* 18, 014102; (8 pages)

Vanella, M. and Balaras, E. (2009), A moving-least-squares reconstruction for embedded-boundary formulations. *Journal of Computational Physics*, 228, pp 6617-6628.

Vanella, M., Fitzgerald, T., Preidikman, S., Balaras, E. and Balachandran, B. (2009) Influence of flexibility on the aerodynamic performance of a hovering wing. *Journal of Experimental Biology*, 2009, 212, 95-105

Walker, T. J. (1999). Largest Lepidopteran Wing Span, *University of Florida Book of Insect Records*, Department of Entomology & Nematology, University of Florida, Gainesville, FL

Wang, Z. J. (2000a). Two dimensional mechanism for insect hovering. *Physical Review Letters*, 85, 2216-2219.

Wang, Z. J. (2000b). Vortex shedding and frequency selection in flapping flight. *Journal of Fluid Mechanics*, 410, 323-341.

Wang, Z. J., Birch, J. M. and Dickinson, M. H. (2004). Unsteady forces and flows in low Reynolds number hovering flight: two-dimensional computations vs robotic wing experiments. *Journal of Experimental Biology*, 2004, 207, 449-460.

Weis–Fogh, T., (2001) Biology and physics of locust flight. II. Flight performance of the desert locust (Schistocerca gregaria). *Philosophical Transactions of the Royal Society B*, 1965, 239, pp 459–510.

White, F.M. (1974), *Viscous Fluid Flow*, McGraw-Hill.

Wood, G. (1983), *Guinness Book of Animal Facts and Feats*, 3rd Ed., Sterling Publishing Co., Inc.

Yang, J. and Balaras, E. (2006), An embedded-boundary formulation for large-eddy simulation of turbulent flows interacting with moving boundaries. *Journal of Computational Physics*, 215, 12-40.

Yang, J., Preidikman, S. and Balaras, E. (2008), A strongly-coupled, embedded boundary method for fluid-structure Interactions of elastically mounted rigid bodies. *Journal of Fluids and Structures*, 24, 167-182.